

Doppler Radar Monitoring of Lava Dome Processes at Merapi Volcano, Indonesia

Dissertation
zur Erlangung des Doktorgrades
der Naturwissenschaften im Department
Geowissenschaften
der Universität Hamburg

vorgelegt von
Malte Vöge

aus
Marne

Hamburg
2007

Als Dissertation angenommen vom Department Geowissenschaften der Universität
Hamburg

aufgrund der Gutachten von Prof. Dr. Matthias Hort
und Dr. Joachim Wassermann

Hamburg, den 20.12.2006

Prof. Dr. Kay-Christian Emeis
(Leiter des Departments Geowissenschaften)

Zusammenfassung

Der Vulkan Merapi in Zentral-Java in Indonesien ist einer der gefährlichsten Vulkane weltweit. Aufgrund der hohen Viskosität seiner Magmen kann die austretende Lava nicht ruhig über die Flanken abfließen, sondern türmt sich zu einem sogenannten Lavadom auf. Ein Indikator für die Stabilität des Lavadomes sind Steinschläge und Block- und Aschenströme, die von lokalen Instabilitäten am Dome verursacht werden. Der Dom kollabiert, wenn er eine kritische Größe erreicht. Das Resultat sind zerstörerischen Block- und Aschenströmen, die mehrere Kilometer in die Umgebung des Vulkans reichen können. In der Vergangenheit wurde die Aktivität von Steinschlägen und Block- und Aschenströmen visuell und durch seismische Netzwerke beobachtet. Visuelle Beobachtungen sind allerdings oft unmöglich, da am Merapi in der Regel schlechte Sichtbedingungen herrschen. Seismische Messungen können solche Ereignisse zwar kontinuierlich beobachten, sie lassen zur Zeit aber nur wenig Schlüsse über die in das Abbrechen von Dommaterial involvierten dynamischen Prozesse zu.

Um das Monitoring von Lavadomaktivitäten zu verbessern, wurde im Oktober 2001 ein erstes Prototyp Doppler Radarsystem auf der westlichen Flanke des Merapi installiert. Der Kern dieses Systems ist ein sogenanntes "frequency modulated continuous wave" (FMCW) Doppler Radar. Die von dem System registrierten Dopplerspektren geben Aufschluß über die Größe von Materialbewegungen und die darin involvierten Geschwindigkeiten. Da das Radarsystem von Wolken nicht beeinflusst wird, bietet das System erste "quasi-visuelle" kontinuierliche Beobachtungen von Dominstabilitäten. Im August 2003 wurde das Radarsystem zu einem kompletten Monitoringsystem erweitert. Um eine präzise Ausrichtung des Radarstrahls auf den aktiven Bereich am Dom zu erreichen, wurde das Radarsystem mit einem elektrischen Schwenk-Neige-Kopf ausgerüstet. Eine CCD-Kamera wurde am Radarspiegel angebracht, um eine bessere Dokumentation der Ausrichtung des Radarstrahls zu gewährleisten und um zusätzlich Veränderungen am Dom visuell zu dokumentieren. Über Datenfunk werden die gemessenen Daten, Bilder der Kamera und Statusinformationen an das Merapi Volcano Observatory übermittelt, wo diese prozessiert und interpretiert werden können. Unabhängig vom Datenfunk werden Statusinformationen ebenfalls über ein GSM Modem per SMS verschickt. Ein zweites Radarsystem wurde im Januar 2005 installiert.

Anhand der gemessenen Dopplerspektren konnten drei verschiedene Prozesse in

Verbindung mit Dominstabilitäten identifiziert werden: rutschendes Dommaterial, gravitative Abbrüche und explosive Ausbrüche. Zusätzlich erlaubt das Dopplerradar Regenmessungen, anhand derer mögliche Zusammenhänge zwischen Domaktivität und Regenfall untersucht werden können. Aufgrund der großen Anzahl von Dominstabilitäten, die in Zeiten starker Aktivität auftreten, ist eine manuelle Auswertung solcher Ereignisse unmöglich. Daher wurde ein Klassifikationssystem entwickelt, das in der Lage ist, die unterschiedlichen Arten von Dominstabilitäten, Regenereignisse sowie Störungen unbekanntes Ursprungs zu unterscheiden. Für die Klassifikation von einzelnen Dopplerspektren wurden zwei verschiedene Klassifikatoren verwendet: neuronale Netze und die K-nearest-neighbor Methode. Da Ereignisse in den Radardaten aus einer Serie von Dopplerspektren bestehen, kann sich der beobachtete Prozess während eines Ereignisses ändern. Daher wurde ein Regelsatz erstellt, mithilfe dessen der Typ des Ereignisses anhand der Sequenz von bereits klassifizierten Dopplerspektren bestimmt wird.

Zwischen November 2001 und Juli 2004 wurden ca. 80000 Radarereignisse registriert. Das Klassifikationssystem hat ungefähr 57000 dieser Ereignisse als Dominstabilitäten identifiziert. Ein Vergleich dieser vom Radarsystem registrierten Dominstabilitäten mit Steinschlag-Messungen des seismischen Netzwerks des Merapi Volcano Observatory demonstriert das große Potential von Dopplerradar Messungen zur Beobachtung von Dominstabilitäten. Wenn das Radarsystem auf den aktivsten Bereich am Dom ausgerichtet ist, werden mehr Ereignisse identifiziert, als vom seismischen Netzwerk, was überwiegend eine Folge der kürzeren Dauer der Ereignisse in den Radardaten ist. In Kombination mit seismischen Messungen erlaubt das Radarsystem, Verlagerungen der Aktivität am Dom zu beobachten. Die unterschiedlichen Typen von Dominstabilitäten wurden auf ihre relative Häufigkeit, ihre Größe und ihre Geschwindigkeit untersucht. Gravierende zeitliche Veränderungen konnten weder in der Häufigkeit noch in den charakteristischen Eigenschaften beobachtet werden. Es wurde allerdings beobachtet, dass in dem vom stärksten Rückgang der Aktivität geprägten Zeitraum explosive Ereignisse, die direkt einem gravitativen Abbruch folgen, schneller zurückgingen, als explosiv beginnende Ereignisse. Eine Verbindung zwischen Domaktivität und Regenfall konnte über den gesamten untersuchten Zeitraum nicht beobachtet werden. Dies mag allerdings an der über den gesamten untersuchten Zeitraum kontinuierlich sinkenden Aktivität liegen.

Abstract

Merapi volcano in Central Java, Indonesia, is considered one of the most dangerous volcanoes worldwide. Due to the high viscosity of its magma, the lava emerging at the top the volcano cannot flow silently down the flanks of the volcano but builds a lava dome. An indicator for the stability of the lava dome are rockfalls and block and ash flows, which are caused by local instabilities at the dome. When the lava dome reaches a critical size, it collapses. This results in dangerous block and ash flows, which can reach several kilometers into the proximity of the volcano. In the past rockfall and block and ash flow activity has been observed visually or by seismic networks. However, visual observations are often impossible due to bad visibility conditions and until now seismic measurements allow only few insights into the dynamic processes that are involved in instability events, i.e. events of material breaks off the lava dome.

In order to enhance monitoring of lava dome activity, a first prototype Doppler radar system has been installed at the western of the Merapi in October 2001. This system consists of a frequency modulated continuous wave (FMCW) 24GHz Doppler radar. The Doppler spectra recorded by the system give a relative measure of the amount of material moving through the beam as well as information about its velocities. Because the radar system is insensitive for clouds, the system provides first continuous "quasi-visual" observations of dome instabilities. In August 2003 the radar system was upgraded, in order to provide a complete Doppler radar monitoring system. For precise positioning of the radar beam the system has been equipped with an electromechanical mounting. A CCD-camera has also been attached to the radar mirror to better document the radar beam position and for visual observation of the dome. Via radio modems the measured data, images from the camera and status information are transmitted to the Merapi Volcano Observatory, where it can be processed and interpreted. Status information is also sent independent of the radio communication as SMS via a GSM-modem. A second radar system has been installed in January 2005.

From the Doppler spectra we were able to identify three different kinds of processes: sliding material, gravitational break-offs and explosive outbursts. In addition, our Doppler radars provide rain measurements, which can be used to investigate possible correlations between rainfall and dome activity. Due to the large number of instability events that occur during times of high activity, manual processing and

analysis of instability events is not practical for monitoring purposes. Therefore, an automatic classification system has been developed, which is capable of identifying different kinds of instabilities as well as rainfall and disturbances of unknown origin. For the classification of single Doppler spectra two different kinds of classifier models have been used, a neural network and a K-nearest-neighbor classifier. Because events detected by the radar system consist of a series of Doppler spectra, they can contain a sequence of different processes. Therefore, a rule set has been defined, which determines the type of radar event according to the already classified sequence of Doppler spectra.

Between November 2001 and July 2004 about 80000 radar events have been detected. The classification system identified about 57000 of these events as dome instability events. A comparison of the record of detected instabilities with rockfall measurements deduced from the seismic network of the Merapi Volcano Observatory demonstrates the high potential of Doppler radar measurements for monitoring of dome activity. When aligned to the most active area at the dome, the radar detects significantly more events than the seismic system, which is mainly due to the fact that events in the radar data have a shorter duration than events detected by the seismic network. In combination with seismic measurements, the Doppler radar allows to identify changes in the location of the most active area at the dome. The different types of instabilities have been analyzed for their occurrence frequency in terms of size, volume and mean velocity. Significant temporal changes in the relative frequencies or the characteristic properties of the different types of instabilities have not been observed. However, during the period of fastest activity decrease, explosive instability events with a gravitational precursor decreased faster than events starting explosively. A link between rain and dome activity could not be observed throughout the observation period, which might be due to the fact that the activity has been almost continuously decreasing.

Contents

1	Introduction	1
2	Monitoring Volcano Eruptions and Lava Domes with Doppler Radar	7
2.1	The Use of Doppler Radar in Volcanology	8
2.2	Looking Into an Eruption: Strombolian Activity and Lava Fountains	10
2.3	Monitoring Dome Activity	11
2.4	Hazard Mitigation	13
3	Installation of a Doppler Radar Monitoring System at Merapi Volcano, Indonesia	15
3.1	Introduction	16
3.1.1	Monitoring at Merapi	17
3.1.2	Radar observation of volcanic activity	18
3.2	FMCW - Doppler Radar Principle	20
3.2.1	Range resolution	22
3.2.2	Velocity resolution	24
3.3	The Doppler Radar Monitoring System	27
3.3.1	Doppler - Radar Setup	27
3.3.2	The Logging Unit	30
3.3.3	The Observatory Unit	31
3.4	System Setup at Merapi	32
3.5	Observations	35
3.6	Conclusion and Outlook	43

4	Automatic Classification of Dome Instabilities based on Doppler Radar Measurements at Merapi Volcano, Indonesia: Part I	47
4.1	Introduction	48
4.2	System Description	49
4.3	Types of Radar Events	51
4.3.1	Rain	53
4.3.2	Disturbances	54
4.3.3	Dome Instabilities	54
4.4	Detection of Radar Events	58
4.5	Bayesian Decision Theory	62
4.6	K-Nearest-Neighbor Classifiers	64
4.7	Neural Network Classifiers	66
4.8	Single Spectrum Classification	71
4.8.1	Training Data	72
4.8.2	Feature Extraction	73
4.8.3	<i>One-Step</i> Classification	75
4.8.4	<i>Two-Step</i> Classification	81
4.9	Event Classification	87
4.10	Conclusion and Outlook	90
5	Automatic Classification of Dome Instabilities based on Doppler Radar Measurements at Merapi Volcano, Indonesia: Part II	95
5.1	Introduction	96
5.2	System - Setup	98
5.3	Observation of Dome Activity between November 2001 and July 2004	100
5.4	Discussion and Conclusion	108
5.4.1	Sensitivity of the radar system	109
5.4.2	Dynamic Processes During Instability Events	111
5.4.3	Volcanic Activity and Rain	113
5.4.4	Conclusion	116
6	Conclusion and Outlook	119

Bibliography	125
A Software Development	133
B Radar Beam Calibration	138
Acknowledgments	143

Chapter 1

Introduction

Volcanoes are amongst the most spectacular natural phenomena, and people are fascinated by their beauty as well as by their dynamic eruptions. They exhibit a wide variety of eruption styles ranging from effusive eruptions typically resulting in lava flows or lava fountains, over medium sized explosive Strombolian eruptions, to large plinian eruptions with eruption columns of several tens of kilometers in height. Besides earthquakes, floods and storms volcanic eruptions present the largest natural hazards, and compared to earthquakes, floods and storms, they can even influence the earth's climate (see e.g. Schneider, 1983). Volcanic hazards are as diversified as the eruptions themselves. They can be a direct result of the volcanic activity, e.g. lava flows, ash fall, pyroclastic flows and gases, or they can be triggered by a combination of volcanic and non-volcanic processes, i.e. lahars (rain triggered mud and debris flows), landslides and tsunamis. In the Holocene (past 10.000 years) about 1370 volcanoes have erupted and on average about 60 were active each year during the 1990s (Simkin and Siebert, 2000). Many of these volcanoes are located in developing countries with high population densities, which of course increases the potential risk presented by a volcano. During the last century about 78.000 people were killed as a direct result of volcanic activity, most of them during the eruptions of Montagne Pelée in 1902 (28.000 fatalities) and Nevado del Ruiz in 1985 (25.000 fatalities) (Tanguy et al., 1998). Understanding volcanic eruptions is therefore not only of scientific but also of a strong public interest.

One of the most dangerous volcanoes worldwide is Merapi volcano, located on the island of Java, Indonesia, which is one the most active volcanic areas with about 30 currently active volcanoes (Fig. 1.1). Java is part of the Sunda-Arc, where the Indo-Australian plate is subducted under the Eurasian plate. The subducted oceanic lithosphere is rich in volatiles (mainly H_2O and CO_2). The release of volatiles from the subducted slab into the mantle supports the genesis of magmatic melts, which

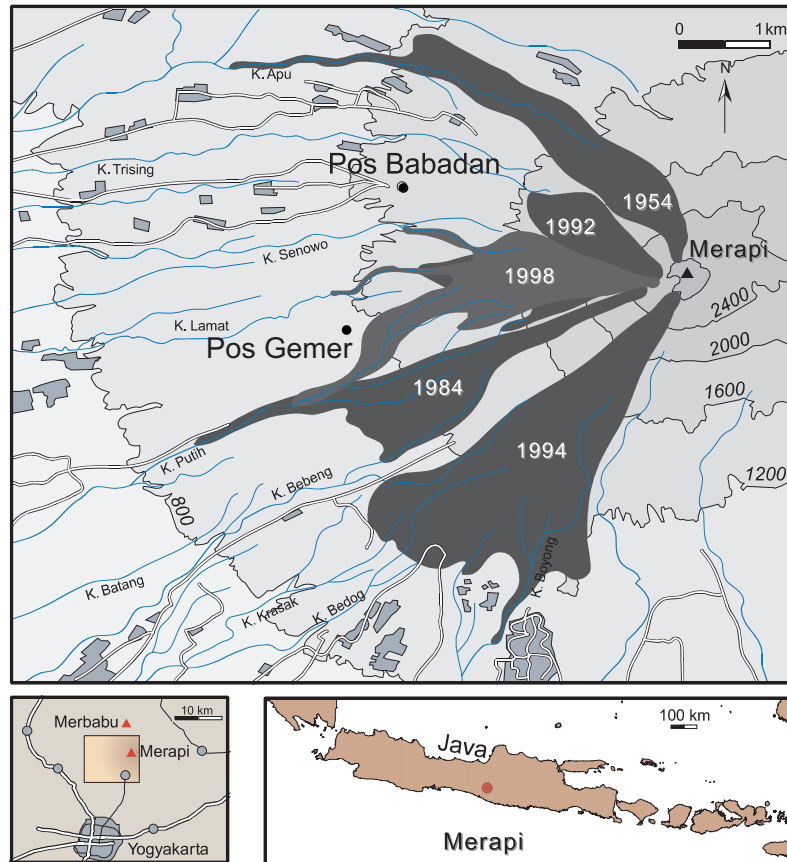


Figure 1.1: Location of Merapi volcano in central Java, Indonesia, and deposit mappings of recent block and ash flows (Schwarzkopf and Schmincke, 2000).

ascent due to their lower density compared to the surrounding mantle rock leading to volcanism. Merapi's magma is basaltic andesite, which is typical for the volcanism in this region. It has a SiO_2 content of about 52–58wt% (Gertisser and Keller, 2003) and has a very high viscosity. Thus, when the magma reaches the surface, it is too viscous to calmly flow down the flank of the volcano, as it is typical for, e.g. Hawaiian volcanoes. Instead, the lava piles up at the top of the volcano and builds a so-called lava dome. Although the magma continuously degases while ascending, it does so at a comparatively low rate and is therefore still rich in gases when reaching the surface (see e.g. Le Guern et al., 1982, and Zimmer and Erzinger, 2003). This property combined with high pressures and temperatures of several hundred $^\circ\text{C}$ make the dome a highly dynamic system. When the dome reaches a critical size, it collapses partly or completely generating hazardous so-called nuée ardente or block and ash flows, which can reach several kilometers into the vicinity of the volcano.

While plinian eruptions occurred at Merapi in the past (the last in 1872), the activity of the last century was dominated by dome building phases with mostly gravitational

collapses. Merapi is considered one of the most dangerous volcanoes exhibiting this type of activity, which was therefore named *Merapi-type* activity. The high risk is a combination of the type of activity and the high population density around the volcano. Due to their fertile soil, the flanks of Merapi are particularly attractive for farmers, and as a consequence about 80000 people live in the so-called *forbidden zone* extending several kilometers around the volcano (see Crandell et al., 1984, and Voight et al., 2000). Therefore, a dome collapse event in 1930 resulted in a large number of about 1300 fatalities. Since 1972 Merapi has been almost continuously active with major dome collapses in 1984, 1994, 1997, 1998, 2001 and 2006. During the 1994 dome collapse about 60 people were killed, and also during the activity in 2006 three people lost their lives, two of which tried to escape a block and ash flow inside a bunker.

Following the catastrophic 1930 eruption Merapi has been observed with increasing effort. Today, a wide variety of geophysical measurement techniques has been setup to monitor the activity at the dome as well as down in the subsurface deep under the volcano. This includes seismic measurements (e.g. Ratdomopurbo and Poupinet, 2000, and Wassermann and Ohrnberger, 2001), ground deformation measurements (Rebscher et al., 2000), gas composition measurements (Zimmer et al., 2000), and electrical and magnetic field measurements (Friedel et al., 2004, and Zlotnicki et al., 2000). Direct visual observations of the active dome still plays an important role. During a volcanic crises the stability of the dome and the most probable direction of a dome collapse has to be assessed in order to evacuate the threatened areas in time. However, due to the tropical climate the summit of Merapi is often covered with clouds and, therefore, continuous visual observations are difficult. An important indicator for the stability of the dome is the occurrence frequency and size of rockfalls and block and ash flows. A fast growing dome can produce several hundred rockfall events per day. When moving down the flank of the volcano rockfalls generate seismic wave, which travel through the volcanic edifice. In the past rockfalls, therefore, have been monitored by seismic measurements (see, e.g. Ratdomopurbo and Poupinet, 2000, and Ohrnberger, 2001). Of course, an active volcano generates various types of seismic signals, most of them originating from the subsurface. Thus, rockfall signals have to be distinguished from other types of seismic signals to provide accurate monitoring.

In order to enhance the observation of the dome stability, two Doppler radar systems have been installed at Merapi. Doppler radars send out electromagnetic waves. When reflected at an object, these waves are received back at the radar. The amplitude of the received signal gives information about the amount of reflecting material and due to the Doppler effect information about the velocities of the objects is also available. Additionally, from the travel time of the waves Doppler radars are able to provide information about the distance of the objects. The Doppler radar technique is relatively new in the field of volcanology and has first been applied at Stromboli volcano, Italy, by Hort and Seyfried (1998) and at Etna, also Italy, by

Dubosclard et al. (1999). In both cases Strombolian eruptions have been observed in order to gather new insights into the dynamic processes associated with this kind of eruption. The Doppler radar monitoring at Merapi volcano started in late October 2001 and marks the first application of this technique to monitor a dome building volcano, providing *quasi-visual* observation of dome processes independent of visibility conditions.

This thesis is structured in four main chapters. Each chapter presents a paper, which has been published or is submitted. Chapter 2 consists of the short paper "Monitoring Volcano Eruptions and Lava Domes with Doppler Radar", which has been published in *EOS* (Voege et al., 2005) and reviews past and present applications of the Doppler radar technique in the field of volcanology.

Chapter 3 "Installation of a Doppler Radar Monitoring System at Merapi Volcano, Indonesia", submitted to *Journal of Volcanology and Geothermal Research*, provides details about the Doppler radar systems installed at Merapi. After a short review of the various monitoring systems installed at Merapi, a thorough description of the measurement principle of the Doppler Radar is given. Because setting up a permanent monitoring system strongly differs from short-term field measurements a great effort has been undertaken in developing the system's infrastructure, including a specifically for this application developed logging unit, data transmission via radio modems and storage of the measured data in a state-of-the-art database system. Examples for the different types of events that are observed by the radar system, i.e. sliding dome material, gravitational break-offs of dome material and explosive outbursts, are given in the paper. A fourth non-dome related type of event is rain fall. In order to show that simultaneous recordings of radar and seismic data enhance the understanding of the dynamic processes during dome instabilities, selected Doppler radar and seismic recordings are compared (seismic data courtesy of Joachim Wassermann, LMU, Munich).

Chapter 4 and 5 is a set of companion papers on "Automatic Classification of Dome Instabilities based on Doppler Radar Measurements at Merapi Volcano, Indonesia, Part I+II", which have been submitted to *Geophysical Journal International*. Because of the huge amount of data, i.e. up to several hundred events per day, manual processing is impossible, especially, in the case of continuous monitoring. Therefore I have developed an automatic classification system which is described in Chapter 4. First, a I review the different types of events that can be discriminated from the radar data and the event detection procedure is described. The first step in the presented classification procedure is the discrimination between five different types of Doppler spectra: disturbances, rainfall, sliding material, gravitational break-offs and explosive outbursts. Disturbances are considered not to be linked to any natural process, however, their source is unknown. Two different classifier models have been applied to Doppler spectra: artificial neural networks and the K-nearest-neighbor method. Both models are based on supervised learning and, thus, they had to be

trained with manually classified Doppler spectra. An important task for classification or pattern recognition is feature extraction. The raw Doppler spectra have been analyzed for features that are characteristic for the different types of processes leading to the definition of so-called feature vectors. A good feature vector definition results in similar vectors for spectra of the same class and very different vectors for spectra of different classes. The feature vectors are fed to the classifier. Several combinations of classifier model and feature vector have been tested. To obtain a good measure of the classification performance I used independent data sets for training, validation and testing. Because radar events consist of a sequence of Doppler spectra, the resulting sequence of classified spectra is analyzed in order to determine the correct event class.

The classification system has been applied to a large data set consisting of radar measurements covering 3 years and a total number of about 57000 instability events. In Chapter 5 "Automatic Classification of Dome Instabilities based on Doppler Radar Measurements at Merapi Volcano, Indonesia, Part II", this data set is used to evaluate the performance of Doppler radar measurements for monitoring dome activity. Therefore, the classified events have been compared to a record of daily numbers of rockfall events, which have been manually identified from seismic traces measured by the seismic network of the Merapi Volcano Observatory. The comparison shows that during times of high activity the radar system identifies considerably more rockfall events than the combination observer–seismic network. However, since the radar does not cover the complete dome a precise alignment of the radar beam to the active spot is necessary. This restriction, however, provides the ability to monitor changes in the location of the activity, especially, when combining radar and seismic measurements. I also analyzed the data for changes in the type of activity, i.e. in the properties and relative occurrence frequency of the different types of instabilities, and I was able to observe a change in the relative number of dome instabilities with initial explosive outburst and with a gravitational break-off followed by an explosive outburst. Because the radar system detects also rain fall I analyzed the radar data for a correlation of rainfall and dome activity, however, no such correlation could be found.

Chapter 6 summarizes the thesis and discusses the role of Doppler measurements for dome monitoring and volcanic hazard mitigation.

Chapter 2

Monitoring Volcano Eruptions and Lava Domes with Doppler Radar

by Malte Vöge, Matthias Hort and Ralf Seyfried

Published in EOS, Transactions of the American Geophysical Union, vol. 86(51), 537–548, 2005

About 10 percent of the world's population lives in the vicinity of one of the planet's approximately 1500 active volcanoes. These volcanoes represent a large threat to human lives and regional economies, especially in highly-populated areas. This makes effective and reliable volcanic hazard mitigation absolutely mandatory.

Because volcanoes are complex systems, hazard mitigation can be achieved only by applying numerous techniques, such as geophysical monitoring, thorough mapping of previous activity, and numerical simulations of different eruption scenarios.

Direct visual observations of eruptions also help in understanding volcanic activity. However, continuous quantitative observations of near-vent processes are scarce because in situ placement of measuring devices in volcanic vents is nearly impossible due to their inhospitable environments. In the past, processes at active vents (Chouet et al., 1974; Ripepe et al., 1993) or domes (Sato et al., 1992) have been characterized mainly by photometry or video recordings. However, neither technique can be effectively applied for continuous measurements because they require good visibility conditions that are not always available.

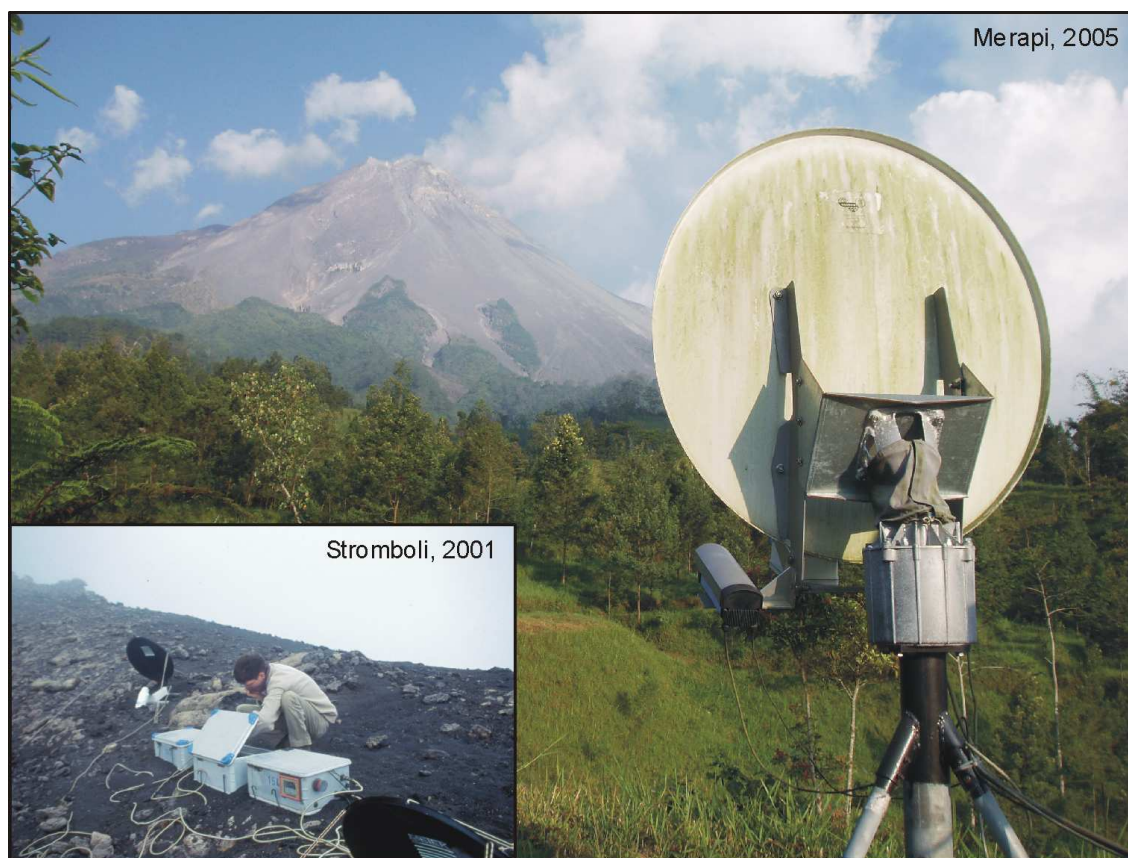


Figure 2.1: The Doppler radar system in action at the Merapi and Stromboli volcanoes.

2.1 The Use of Doppler Radar in Volcanology

Doppler radar-based measurements of material movements at volcanoes, an observational method introduced over the past decade, has become a powerful tool to quantify eruption dynamics. Doppler radar instruments transmit a distinct frequency microwave. When this microwave is reflected at an object, the received signal exhibits a frequency shift that is directly proportional to the object's velocity along the beam (radial velocity). The amplitude of the reflected signal is proportional to the number and individual size of the objects. Thus, by measuring the amplitudes of all frequency shifts within a given bandwidth (velocity interval), a velocity distribution is recovered that reflects a mass movement as a function of velocity. To recover the full three-dimensional velocity vector, data from at least three instruments are needed.

Two different mobile Doppler radar systems have been developed for observing dy-

	MVR-3	VOLDORAD
Signal	Continuous wave, 50mW	Pulsed system, pulse length between 0.4-1.5ms, peak power 60W, pulse repetition 0.05 or 0.1ms
Frequency (wavelength)	10GHz (3cm) 24GHz (1.25cm)	1.238GHz (24 cm) 1.274GHz (24 cm)
Antenna Type	Offset parabolic mirror	Array of 4 Yagi antennas
Sampling rate	1Hz	10Hz or higher
Observation distance	60 cm mirror: 2000m 120 cm mirror: 5000m	500-5000m
Distance resolution	10-1000m	60-220m
Power consumption	30W	200W
Weight	45kg (60cm mirror) 80kg (120cm mirror) (including logging unit and power supply)	60kg (excluding power supply and antennas)
Transportation	60cm system: 3 backpacks 120cm system: 4 wheel drive	4 wheel drive

Table 2.1: Comparison of the two Doppler radar systems currently being used in volcanology

dynamic processes at volcanoes. The French Volcano Doppler Radar (VOLDORAD) system (e.g. Dubosclard et al., 2004) is a pulsed Doppler radar, whereas the MVR-3 (MeTek Volcano Radar) (e.g. Hort and Seyfried, 1998) is a frequency modulated continuous wave (FMCW) system.

The main consequence of this technical difference is that with VOLDORAD, distance is measured through travel time of the microwave, whereas with the MVR-3 the frequency modulation allows for distance resolution. The technical details of both systems are summarized in Table 2.1. Both systems have been used at different volcanoes –Etna and Arenal (VOLDORAD), and Stromboli, Merapi, and quarry blasts near Dresden, Germany (MVR-3)– and data processing and interpretation techniques have been developed (Hort et al., 2003; Dubosclard et al., 2004).

2.2 Looking Into an Eruption: Strombolian Activity and Lava Fountains

The Stromboli volcano in Italy is famous for its continuous eruptions that have occurred for at least the last 5000 years. Two or three active craters explosively erupt on average every 15-20 minutes. Eruptions are driven by ascending gas bubbles within the magma column that explode or collapse upon reaching the surface, giving rise to the typical Strombolian activity of short-lived outbursts of lava. The first Doppler radar measurements of volcanic activity using a mobile prototype FMCW radar were carried out at Stromboli in 1996 and proved that even very weak eruptions that are hardly visible to the human eye could be detected (Hort and Seyfried, 1998).

During 2000-2001, three experiments were conducted, using one MVR-3 in the first experiment and three MVR-3 in the second and third experiments. In May 2000, one instrument was installed at the Pizzo Sopra la Fossa, an older crater rim of Stromboli, about 350 meters away from the active crater (Figure 2.1). A recording of a typical explosion is shown in Figures 2.2a and 2.2b.

Processing of data recorded from 702 eruptions that occurred during two weeks in May 2000 revealed that the average duration of the rise phase (the time from the onset until the ejecta stop rising and start falling back to the ground) of ejected material increased from about six seconds before a heavy rainstorm to 10 seconds after the storm. By analyzing the settling velocities of particles, the average grain size was found to decrease from about eight millimeters before the rainstorm to about four millimeters after the storm [Hort et al., 2003]. The longer rise phase and increased fragmentation can be attributed to the infiltration of rainwater into the volcanic system, though other reasons, such as changes in the conduit geometry, are also possible. During the second experiment in September 2000, three instruments were installed to record the complete eruption vector (Figure 2.2e).

Much stronger eruptions than those seen at Stromboli were observed using VOLDO-RAD at Mount Etna, Italy, in 1998 and 2001 (Dubosclard et al., 2004), as well as at Arenal, Costa Rica, in 2004–2005. At Etna, a close correlation was found between the recorded eruption velocities and the tremor amplitude. Observed time delays between the maximum tremor amplitude and the highest material flux at the vent led Dubosclard et al. (2004) to suggest that the reservoir is located either at a depth of 500 meters or at a depth of roughly seven kilometers. Both depths deduced from the radar measurements are consistent with different reservoir depths suggested by seismic observations. The material flux observations are also consistent with video observations.

2.3 Monitoring Dome Activity

Volcanoes that produce highly viscous magma often develop a lava dome. During dome growth, parts of the dome can break off because of local instabilities, resulting in rock falls or block and ash flows. The whole dome even may collapse, generating devastating pyroclastic flows.

Gunung Merapi is a dome-building volcano located in Central Java, Indonesia. Because of its fertile soil, at least 80,000 people (Voight et al., 2000) live along the flanks of Merapi in the 'forbidden zone' directly affected by the volcano's activity. Major dome collapses have run-out distances of up to 10 kilometers. There have been about 10 major dome collapses within the past century, resulting in more than 1500 fatalities; a 1930 dome collapse alone caused 1370 fatalities.

Numerous techniques have been used over many years to characterize the state of the volcano's activity. However, because Merapi's dome is in clouds for at least half the time, continuous visual observation of the activity at the dome has not been possible.

In collaboration with staff members of the Merapi Volcano Observatory (MVO) in Yogyakarta, Indonesia, the authors of this article installed in October 2001 a MVR-3 Doppler radar to continuously monitor Merapi's dome. The instrument was set up at a distance of about 4.8 kilometers from the dome. In 2003, the system was equipped with a motor-powered, geared head allowing for easy reorientation of the beam (Figure 2.1). A video camera is aligned with the radar beam that is used as a telescopic sight. The previously measured beam intensity distribution is overlain onto the camera image, allowing for precise and easy positioning of the beam.

In order to improve the coverage of the dome, a second instrument was installed in January 2005 at about the same distance but at a different location. Both systems transmit their data and video images in real time via radio link to the MVO where the data is analyzed by MVO staff. The systems can also be remotely controlled via radio from the MVO and via Short Message Service commands from nearly anywhere on Earth.

Two processes that cause material to break off from the dome have been identified: explosive instabilities and purely gravitational instabilities. During an explosive instability (Figure 2.2c) a very broad velocity distribution is observed due to the wide range of angles and velocities at which material is moving with respect to the radar beam. The likely cause for such explosive instabilities is the mechanical failure of material at the dome due to gas overpressure (see also Sato et al., 1992).

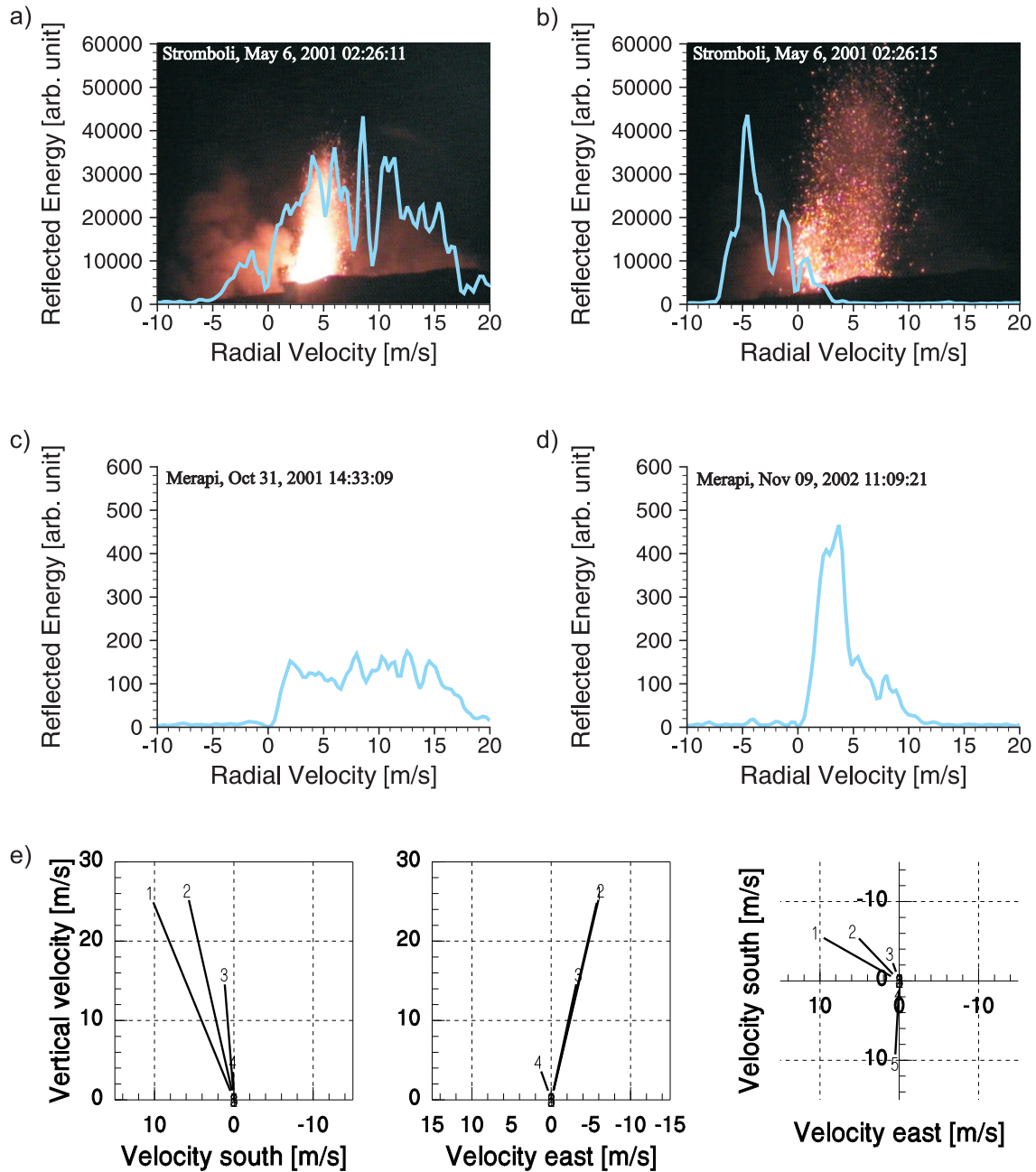


Figure 2.2: (a and b) Two stages of a Strombolian eruption: (a) the initial explosive dispersion and (b) material falling vertically back to the ground. The Doppler spectra are overlying the corresponding video. (c and d) Doppler spectra of instability events at Merapi volcano. (e) Results of a three-dimensional measurement at Stromboli. The small rotation of the eruption vector is probably due to a slight timing problem between the three instruments.

In contrast, the velocity distribution during a gravitational instability (Figure 2.2d) is narrow, with its main peak at low velocities. Also, the material movement is much more focused than during an explosion because material simply slides down the slope. A comparison of these Doppler spectra with those recorded at Stromboli reveals that an explosive instability has a velocity distribution similar to the onset of a Strombolian eruption (compare Figures 2.2a and 2.2c). The velocity distribution of a gravitational instability is similar to that of particles falling back at the end of a Strombolian eruption, when material movement is also nearly unidirectional (compare Figures 2.2b and 2.2d).

2.4 Hazard Mitigation

To provide an easy-to-use tool for hazard mitigation, an online classification system that is able to distinguish between non-volcanic signals (e.g. rain) and explosive and gravitational instabilities is being developed by the authors. Although still under development, this software is already being used by the staff of the MVO to create continuous hourly and daily event-type statistics, which can be used to understand long-term dome growth processes and different types of activity. Thus, this system has the potential to be a valuable asset in supporting decisions of local authorities when analyzing Merapi's state of activity during a future volcanic crisis.

Acknowledgments

Thanks go to Ingolf Bode, Alexander Gerst, Til Hanebut, Jörg Hasenclever, Oliver Hör, Malin Klawonn, Tanja Petersen, Lars Rüpke, Agus Sampurno, Lea Scharff, and Nico Urbanski for their help during different field experiments. We also thank A. Ratdomopurbo from the MVO/BPPTK (Center for Volcano Research and Technology Development), Yogyakarta, Indonesia, for his tremendous support during installation and maintenance of the two permanent stations at Merapi volcano. This work has been funded by the Deutsche Forschungsgemeinschaft through grants to M. Hort.

Chapter 3

Installation of a Doppler Radar Monitoring System at Merapi Volcano, Indonesia

by Malte Vöge and Matthias Hort

Submitted to IEEE Transactions on Geoscience and Remote Sensing, 07/2007

Abstract

Merapi volcano, Indonesia, is one of the most active dome building volcanoes worldwide. Instabilities at the growing dome cause rockfalls and hot block and ash flows, which can reach run-out distances of several kilometers. Therefore, Merapi has been monitored extensively for many years. However, direct visual observation of the dome is often impossible due to cloud coverage of the summit. In October 2001, a first prototype Doppler radar system was installed to overcome this shortcoming. The system is able to penetrate clouds and to observe material movements at the dome, giving valuable information about dynamic processes in the dome area. The system also allows detection of rain fall in several distance intervals. For precise positioning of the beam the system was equipped with an electromechanical mounting in 2003. A CCD-camera attached to the radar mirror documents the radar beam position and provides visual observation of the dome. Recorded data, camera images and status information are telemetered to the Merapi Volcano Observatory, where they can be processed and interpreted. Status information is also sent as SMS via a GSM-modem. Processing the Doppler radar data we are able to discriminate between three different types of instability events: sliding dome material, dome material gravitationally breaking off the dome, and explosive outbursts of dome material due to expansion of volcanic gas. In order to independently verify our



Figure 3.1: Minor block and ash flow on the western flank of Merapi Volcano. The image was taken on July 19, 1998. Picture courtesy Merapi Volcano Observatory.

observations we compared rockfall events detected by the radar system to seismic recordings and found a very good correlation.

3.1 Introduction

Aside from earthquakes, floods, and storms volcanic activity is one of the largest natural hazards to mankind. Every year about 60 volcanoes erupt throughout the world, and during the last 10000 years at least 1500 volcanoes have been active (Simkin and Siebert, 2000). About 10% of the world's population lives in the vicinity of one of these active volcanoes, which are a threat to human lives and economic values. Especially in developing countries many people live in the direct vicinity or even on the flanks of active volcanoes, because volcanic soil is very fertile (Schmincke, 2004), and volcanoes are more and more moving into the focus of tourism. But also in highly industrialized countries there are big cities being threatened by nearby active volcanoes (e.g. Mt. Vesuvius near Naples, Mt. Rainer near Seattle and Fudijama near Tokyo). Therefore volcanic hazard mitigation has become more and more of an issue over the last decades. For an effective and reliable hazard mitigation as much information as possible has to be gathered about the volcano's system. This includes geological and petrological studies (i.e. event stratigraphy), which show patterns in the eruptive behavior, as well as geophysical monitoring. Based on this information hazard maps can be created, and activity alert states can be defined.

Countries located at or near convergent margins are especially endangered by large

earthquakes as well as devastating volcanic eruptions. Indonesia is one of these countries with about 130 active volcanoes (Simkin and Siebert, 1994). One of the most dangerous volcanoes of Indonesia and also worldwide is Merapi Volcano, which is located in Central Java. Merapi is a strato volcano rising 2980m above sea level. Two types of activity have been observed at Merapi: highly explosive plinian eruptions (St. Vincent type) generating high eruption columns and dome building phases. One of the largest documented eruptions of Merapi occurred in 1672, leaving about 3000 people dead (Voight et al., 2000), and the last plinian eruption happened in 1872. Since then the activity at Merapi has been dominated by dome building phases. The SiO_2 -rich basaltic andesitic magma emerging at the top of the volcano is too viscous to flow down the flanks. Instead, it piles up at the top, building a continuously growing lava dome. When the dome reaches a critical size, parts of the dome or even the whole dome can collapse and generate so-called block and ash flows (see Fig. 3.1), which can have run-out distances of more than 10km (see, e.g. Fink and Anderson, 2000, Schwarzkopf et al., 2005, and Voight et al., 2000). The most devastating dome collapse occurred in December 1930. The resulting block and ash flow traveled 12km and destroyed 13 villages completely and 23 villages partly. About 1370 people were killed (Voight et al., 2000). Since 1972 Merapi has been almost continuously active (Schwarzkopf, 2001). About 60 casualties were caused by a dome collapse on November 30, 1994, when a large block and ash flow hit the village of Turgo, which was (and still is) a settlement high up the southwest flank of the volcano. The last major dome collapses occurred in 1998 (Schwarzkopf, 2001), 2001 and 2006, which fortunately did cause only 2 casualties (in 2006). About 80000 people are currently living in the so-called *forbidden zone* (186.4km²) and thus are directly threatened by the volcanic activity (Crandell et al., 1984; Voight et al., 2000). Therefore, a continuous monitoring of the activity at Merapi is absolutely necessary.

3.1.1 Monitoring at Merapi

The Merapi Volcano Observatory (MVO), part of the Volcanological Technical Research Center (VTRC), as well as different research groups from France, the US, Japan, and Germany operate various monitoring systems at Merapi. By far the most extensive monitoring system is the seismic network, which was installed in 1982 (Ratdomopurbo and Poupinet, 2000). The data are continuously recorded on drums and, since 1991, also event-based in digital form. The seismograms are analyzed on a daily basis, and statistics about the different types of events (rockfalls, volcano-tectonic events, multiple-phase events and low frequency events) are created. Besides the VSI network a German research group installed a second network with three seismic arrays each consisting of a broadband and several short period instruments (Wassermann and Ohrnberger, 2001). The data of this system are fed into an automatic analysis program (Earthworm), and into a classification software

(Ohrnberger et al., 2000; Ohrnberger, 2001), allowing an online characterization of Merapi's activity.

Deformation at the flanks of Merapi has been measured by EDM (electronic distance measurement) and, since 1990, by several borehole and platform tiltmeters. The first tiltmeters were installed near the dome to observe displacement correlated to dome growth. Later, tiltmeters have also been set up lower on the flanks of Merapi in order to record the elastic deformation associated with mass displacement further inside the volcanic edifice. In the late nineties the network was extended by four multi-parameter stations, including meteorological instruments as well as GPS antennas and tiltmeters (Rebscher et al., 2000).

Since 1990 the variations in the magnetic field are continuously monitored by four stations (Zlotnicki et al., 2000). Volcanic gases have been collected and analyzed on a monthly basis for many years. Since 1984 the SO₂ flux has been monitored by the MVO using COSPEC. In order to continuously monitor the gas composition as well as temperatures, a measurement station consisting of a gas chromatograph, an alpha scintillation counter, and a thermocouple have been installed at the fumarolic vents of Woro, which is located near the summit of Merapi (Zimmer et al., 2000; Zimmer and Erzinger, 2003). In 2000, a continuous monitoring station for electrical field and ground temperatures was also installed at Woro (Friedel et al., 2004).

Often an eruption or dome collapse is followed by lahars (rain-triggered volcanic debris flows) going down the valleys of Merapi (about 50 followed the 1994 dome collapse). Thus, lahar monitoring has been significantly improved by various measurement techniques, e.g. trip-wire sensors, rain gauges, a weather radar, seismometers, and video cameras (Lavigne et al., 2000a,b).

Because most of the time the summit of Merapi is covered by clouds a continuous visual observation of the dome is not possible. However, an observation of dynamic processes at the dome is important in order to assess its activity as well as its stability. Seismometers are able to detect rockfalls and block and ash flows, but they don't provide information about the triggering processes. Since microwaves penetrate clouds, Doppler radar measurements provide a unique opportunity for quasi-visual observation of dynamic processes at the dome that cannot be observed by any other geophysical measurement technique.

3.1.2 Radar observation of volcanic activity

The first successful applications of radar techniques in the field of volcanology have been made in the mid seventies, when the military radar stations King Salmon

and Sparrevojn (both in Alaska) were used to observe eruption columns. Kienle and Shaw (1979) used those data to estimate the height and the lateral extent of the eruption columns, because this could not be determined visually due to bad weather and darkness. At Mt. St. Helens Harris et al. (1981) and Harris and Rose (1983) used weather radar systems to observe the eruption column of the 1980/82 eruptions. Combining these observations with an eruption column model by Wilson (1976), they were able to estimate the mass eruption rate during the initial phase as well as after 1-2 hours.

Because some of the most active volcanic areas, e.g. Alaska and Iceland, are located along highly frequented aviation routes, and the fact that aircrafts can be severely damaged when flying through volcanic ash clouds, the observation of ash clouds has become of increasing interest. A ground-based C-Band radar was used during the 1992 Mt. Spurr eruption (Rose et al., 1995) to observe the resulting ash cloud in nearly real-time close to the volcano. Additionally, weather satellite data has been used to track the ash cloud for several hours and thousands of kilometers (Schneider et al., 1995). Similar observations have been made by Lacasse et al. (2004) and Rose et al. (2003) at Hekla, Island. In each case the extend of the volcanic ash cloud was successfully tracked by the systems, and estimates for the eruption rates and particle sizes could be derived. Recently, Marzano et al. (2006) have developed an algorithm to derive volcanic ash properties for weather radar observations and successfully applied this method to observations made during the 2004 Grimsvötn eruption (Marzano and Vulpiani, 2006). However, quantitative data about the dynamics near the vent could not be collected by these systems.

The use of Doppler radar observations at volcanoes started during the 1990s. Doppler radars measure the distance and the velocity of moving targets from a remote position. They allow measurements of particle velocities during explosive eruptions and dome instabilities, which lead to rockfalls and block and ash flows. A first experiment was carried out at Stromboli volcano, Italy, in 1996 using a 24GHz frequency modulated continuous wave (FMCW) rain radar (Hort and Seyfried, 1998; Seyfried and Hort, 1999). The experiment proved that even Strombolian eruptions hardly visible to the human eye are detectable using this type of radar. A modified version of the same radar has been used in three more experiments at Stromboli in 2000/2001. In April/May 2000 a clear change in the eruptive behavior from before to after a heavy rainstorm was documented (Hort et al., 2003). In September 2000 the complete velocity vector of Strombolian eruptions could be determined using three Doppler radar systems aiming at the summit from different directions (Voegelé et al., 2005).

A 1.2GHz pulsed Doppler radar called VOLDORAD has been used by Dubosclard et al. (1999) in 1998 at Etna, Italy, and in 2004 at Arenal, Costa Rica (Dubosclard et al., 2004; Donnadieu et al., 2005). At Etna vertical velocities of lava fountains of about 230m/s have been measured. During explosive Strombolian eruptions,

velocities of up to 400m/s occurred. To monitor the growth of the lava-dome of Soufriere-Hills volcano on Montserrat, Wadge et al. (2005) used a 94GHz FMCW ranging radar called AVTIS. AVTIS is designed to measure ranges with a precision of about 1m . The purpose of AVTIS is to create a high resolution topographic model of lava dome's by scanning the dome on a 2-dimensional grid. Repeated measurements reveal even local changes in the dome topography, and thus a detailed investigation of the dome growth is possible. However, the system was not designed to measure Doppler shifts, i.e. dynamic processes with velocities in the m/s range cannot be observed.

To conduct the first Doppler radar observations of dynamic processes at a lava dome, we installed a Doppler radar system at the flank of Merapi volcano in October 2001. A second radar system was installed in January 2005. The aim of the radar observations is to continuously monitor the dome activity and to provide valuable information to the local authorities in case of a volcanic crisis. Therefore, a great effort has been undertaken in developing a stable and reliable monitoring system. Here, we describe the technical development of the Doppler radar monitoring system installed at Merapi volcano. In the next section we start with a detailed description of the principle of the FMCW Doppler radar and the differences to the more commonly used pulsed Doppler radar. The technical infrastructure of the monitoring system, e.g. data logging device, data transmission and processing facilities, are summarized in Section 3.3. Section 3.4 presents the setup of the two Doppler radar stations currently installed at Merapi Volcano. Doppler radar measurements give new insights into the dynamic processes that take place during instabilities at the lava dome. Examples of these are given in Section 3.5 as well as a comparison of Doppler radar observations and seismic observations done by Wassermann and Ohrnberger (2001). Section 3.6 summarizes the properties and facilities of the Doppler radar monitoring system. For the more interested reader, the software controlling the system's components and all its data flows is presented in Appendix A. In Appendix B we detail the calibration measurements help to ensure a precise alignment of the radar beam.

3.2 FMCW - Doppler Radar Principle

Doppler radars send out microwaves of a distinct frequency. When reflected at an object the microwaves are received by the radar, now containing information about distance and velocity of reflecting objects. Most commonly used are pulsed Doppler radars like VOLDORAD (see above), which periodically send out short pulses of microwaves. When reflected at an object, the object's distance from the radar can be calculated from the travel time of the microwave pulse. If the object is moving, the reflected microwaves exhibit a frequency shift, which is known as the *Doppler*

B	Bandwidth of the frequency modulation
T	Duration of one frequency modulation cycle
t_D	Two way travel time of the microwaves
D	Distance between radar and reflecting object
c	Speed of light
λ	Wave length
f	Frequency
v_r	Radial velocity
f_0, ω_0	Base frequency
$\omega_s(t)$	Cycle frequency of the transmit signal
$\psi_s(t)$	Phase of the transmit signal
$s(t)$	Transmit signal
$e(t)$	Received signal
$m(t)$	Mixed signal
$\psi_m(t)$	Phase of the mixed signal
f_m	Frequency of the mixed signal
$M(f)$	Spectrum of the mixed signal
$M(f_i)$	FFT spectrum of the mixed signal
N	Number of samples of the mixed signal per sweep
N_D	Number of range gates
f_{Ny}^m	Nyquist frequency of the mixed signal
N_{sw}	Number of sweep considered for one Doppler spectrum
$p_i(t_j)$	Time-series of $M(f_i)$ over N_{sw} sweeps
$P_i(f_j)$	FFT Doppler spectrum of $p_i(t_j)$
f_{Ny}^p	Nyquist frequency of $P_i(f_j)$
$P(f_k)$	FFT Doppler spectrum of all range gates
$P(i, v_r)$	Doppler spectrum as function of range gate and velocity
$P(i, v_r, t)$	Time-series of repeated measurements of $P(i, v_r)$

Table 3.1: Table of symbols.

shift. This frequency shift is proportional to the velocity component in direction of the radar beam. Because the pulses are short compared to the repetition time they have to be sent out with high power to get a good signal-to-noise ratio.

Frequency modulated continuous wave (FMCW) Doppler radars send out a continuous microwave. In this case the travel time cannot be used to determine distances, and thus more sophisticated hardware as well as signal processing is required. The core component of the radar is a frequency modulated Gunn-diode oscillator with integrated mixing diode (Strauch, 1976). The linear polarized microwaves are fed to an antenna. The backscattered signal is received with the same antenna assembly (monostatic radar). In order to achieve distance or range resolution, the transmitted signal is frequency modulated with the frequency linearly decreasing from $f_0 + B/2$

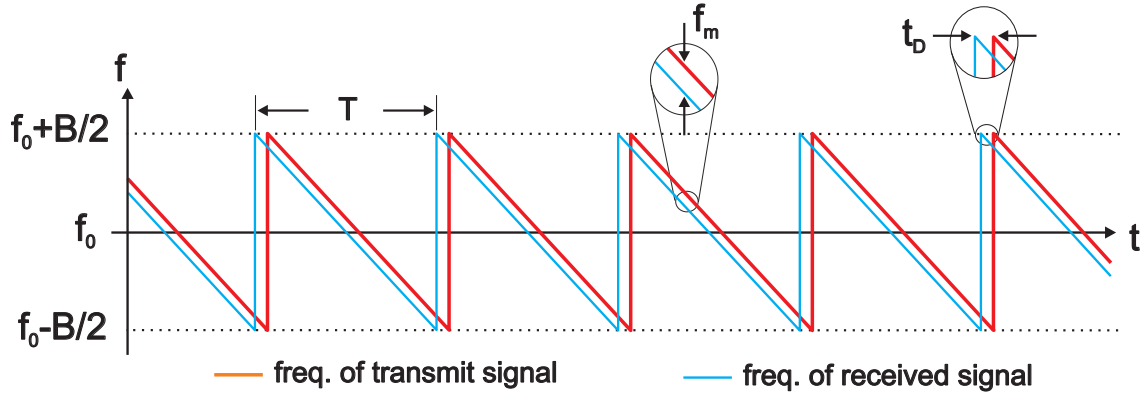


Figure 3.2: Frequency modulation of the transmit signal and its time delayed echo when reflected at a non-moving object. The frequency f_m of the mixed signal $m(t)$ is just the frequency shift between the both signal, which is proportional to the time-delay t_D , and thus to the distance.

to $f_0 - B/2$ and then jumping back to $f_0 + B/2$ (saw-tooth function, see Fig. 3.2). During one of these so-called sweeps the cycle frequency of the transmitted signal is

$$\omega_s(t) = \omega_0 - 2\pi \frac{B}{T} t, \quad \text{for } -T/2 \leq t \leq T/2, \quad (3.1)$$

where B is the bandwidth and T the duration of the frequency modulation, i.e. the duration of one saw-tooth. The phase of the transmitted signal is the integral of its cycle frequency over time between 0 and t :

$$\psi_s(t) = \omega_0 t - \pi \frac{B}{T} t^2. \quad (3.2)$$

Thus, the function

$$s(t) = S \sin(\psi_s(t)) = S \sin\left(\omega_0 t - \pi \frac{B}{T} t^2\right) \quad (3.3)$$

describes the signal transmitted by the Gunn-diode. S is the amplitude of the transmitted signal.

3.2.1 Range resolution

First, we consider a resting target. While the transmitted microwave travels to the target and back to the radar, the transmit frequency is decreasing, due to the frequency modulation (eq. 3.1). Therefore, the transmitted and the received signal

exhibit a frequency difference (see Fig. 3.2) that is proportional to the target's distance from the radar. The received signal can be described by the function

$$\begin{aligned} e(t) &= E \sin(\psi_s(t - t_D)) \\ &= E \sin(\omega_0 t - \omega_0 t_D - 2\pi \frac{B}{2T} (t^2 - 2tt_D + t_D^2)) \end{aligned} \quad (3.4)$$

where E is the amplitude of the received signal and t_D the time delay due to the signal's travel time. The received signal is detected by the mixing diode, which is biased with a fraction of the transmitted signal. The effect of the mixing-diode corresponds to a multiplication of $s(t)$ and $e(t)$:

$$\begin{aligned} m(t) &= S \sin(\psi_s(t)) E \sin(\psi_s(t - t_D)) \\ &= \frac{1}{2} S E \cos(\psi_s(t - t_D) + \psi_s(t)) \\ &\quad + \frac{1}{2} S E \cos(\psi_s(t - t_D) - \psi_s(t)). \end{aligned} \quad (3.5)$$

The first term is the high frequency part of the signal (frequency is approximately $2\omega_0$), which is suppressed by a low pass filter. Thus, the phase of the mixed signal can be written as

$$\begin{aligned} \psi_m(t) &= \psi_s(t - t_D) - \psi_s(t) \\ &= -\omega_0 t_D - \pi \frac{B}{T} t_D^2 + 2\pi \frac{B}{T} t t_D. \end{aligned} \quad (3.6)$$

The frequency of the mixed signal is derived by differentiating $\psi_m(t)$ with respect to t :

$$f_m = \frac{B}{T} t_D. \quad (3.7)$$

The time-delay t_D is given by the object's distance D from the radar: $t_D = 2D/c$, where c is the speed of light. Thus, the frequency shift f_m is directly proportional to the object's distance D and the object's distance can be calculated from

$$D = \frac{cT}{2B} f_m. \quad (3.8)$$

Because $s(t)$ and $e(t)$ are periodic with T , the mixing signal $m(t)$ is also periodic with T . However, because of the frequency jump at the end of a sweep, the $m(t)$ has also a discontinuity at the end of each sweep. Thus, T is the smallest period that is contained in $m(t)$. Therefore, its power spectrum $M^2(f)$ consists of spectral lines only at multiples (harmonics) of $1/T$ (see Fig. 3.3a), and two targets can only be resolved, when separated by a frequency difference of at least $\delta f = 1/T$. Thus, the distance resolution can be calculated from equation (3.8):

$$\delta D = \frac{cT}{2B} \delta f_m = \frac{c}{2B}. \quad (3.9)$$

Therefore, the larger the bandwidth of the frequency modulation B is chosen, the better is the distance resolution.

Now we consider one sweep of duration T digitized with N samples. Because $m(t)$ is real valued, the resulting FFT $M(f_i)$ consists of $\frac{N}{2}$ components at frequencies of $f_i = \frac{i}{T}$, $i = 1, \dots, \frac{N}{2}$. Here, the frequency resolution is again $1/T$, i.e. each spectral line in $M(f_i)$ corresponds to a separate distance range, a so-called *range gate* (see Fig. 3.3a), and the Nyquist frequency of $m(t)$ is

$$f_{Ny}^m = \frac{N}{2T}. \quad (3.10)$$

In order to prevent edge effects, $m(t)$ is multiplied by a window function before the FFT is calculated. This, however, leads to a "leakage" between range gates, i.e. targets also contribute with attenuated amplitude to neighboring range gates as indicated in Figure 3.3. The number of range gates that can be resolved is

$$N_D = \frac{N}{2} \quad (3.11)$$

and using (3.8) the maximum distance that can be reached is

$$D_{max} = \frac{cN}{4B}. \quad (3.12)$$

3.2.2 Velocity resolution

The equations above only hold for non-moving targets, where the frequency shift is only caused by the modulation of the transmitted signal. When the target is moving an additional frequency shift, i.e. the Doppler shift, is observed that is proportional to the target's velocity along the radar beam:

$$f_m = \underbrace{\frac{\Delta f_{vel}}{2}}_{\frac{2}{\lambda}v} + \underbrace{\frac{\Delta f_{dist}}{B}}_{\frac{2D}{cT}}, \quad (3.13)$$

where λ is the wavelength of the microwaves. The velocity v is the projection of the target's 3-dimensional velocity vector onto the radar beam axis, i.e. its radial velocity v_r along the radar beam. Because of the additional frequency shift, the mixed signal is no longer periodic with T . Therefore, the echoes of moving targets do not appear at harmonics of $1/T$ (see Fig. 3.3a). If we were able to get the spectrum of the mixed signal $m(t)$ with arbitrary frequency resolution, targets with different velocities could be discriminated. As long as the condition

$$-\frac{1}{2T} < \frac{2}{\lambda}v_r < \frac{1}{2T} \quad (3.14)$$

holds, the target's echo in the power spectrum will still appear in the correct range gate. Thus, the allowed velocity range is

$$-\frac{\lambda}{4T} < v_r < \frac{\lambda}{4T}, \quad (3.15)$$

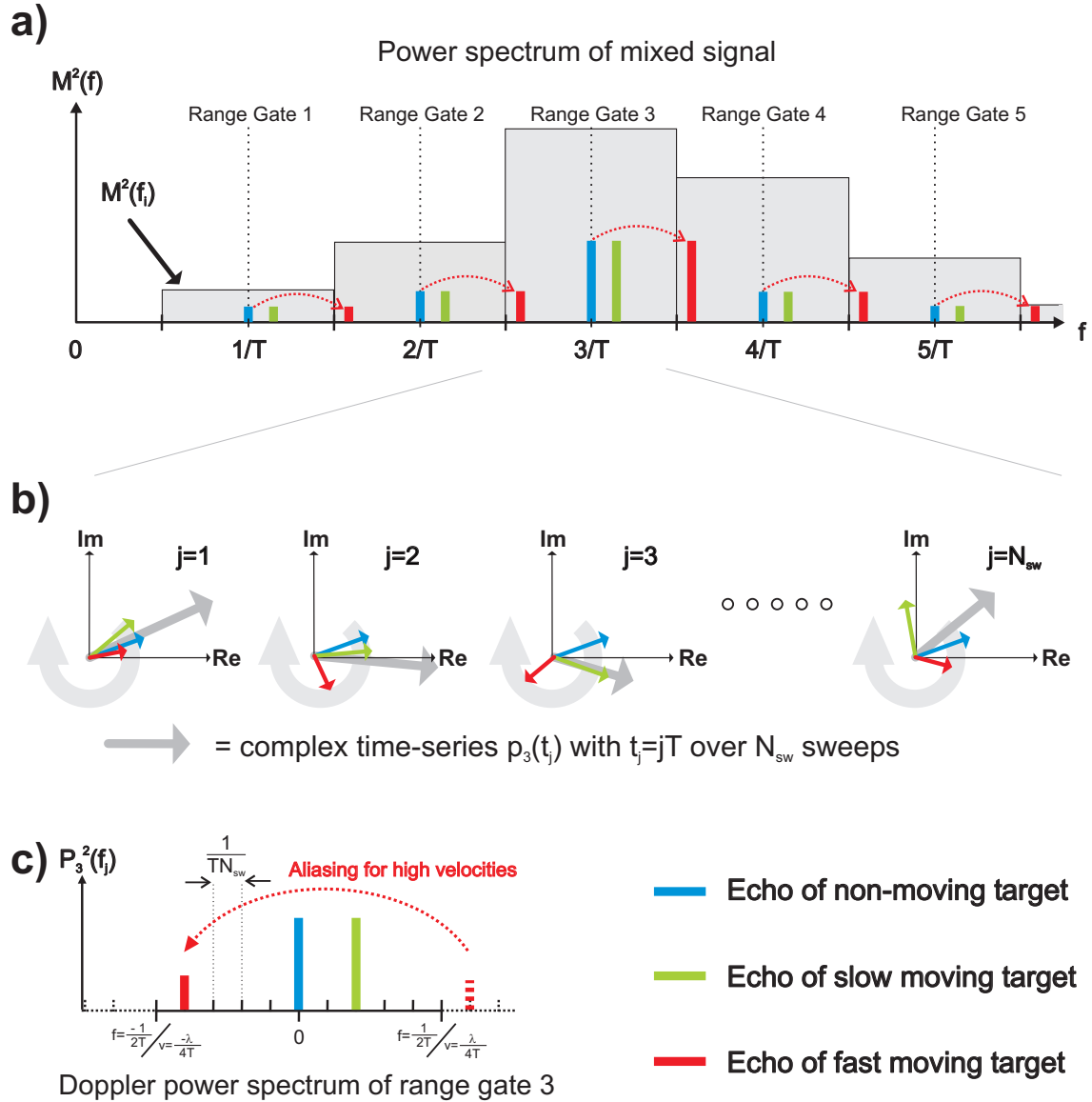


Figure 3.3: (a) Power spectrum of the mixed signal for three targets of different velocity located in range gate 3. The colored bars show spectral components of the theoretical continuous power spectrum $M^2(f)$. Echoes of the non-moving target appear at multiples of $1/T$. Moving targets exhibit an additional frequency shift due to the Doppler effect. The discrete power spectrum $M^2(f_i)$ (gray) of a single sweep digitized with N samples has a frequency resolution of $1/T$, and thus echoes within the corresponding frequency intervals are superimposed. Each component of $M^2(f_i)$ corresponds to one range gate. Note that the echo of the fast moving target (red) contributes to the wrong range gate. (b) Time-series $p_3(t_j)$ of N_{sw} complex power spectrum components $M(f_3)$ for range gate 3 (gray arrows). The colored arrows show the contributing superimposed echoes, rotating with a frequency proportional to their object's velocity. (c) By calculating the FFT $P_3(f_j)$, the frequencies of all phase rotations occurring in $p_3(t_j)$ can be resolved. Because of aliasing the echo of the fast moving object appears at a negative frequency.

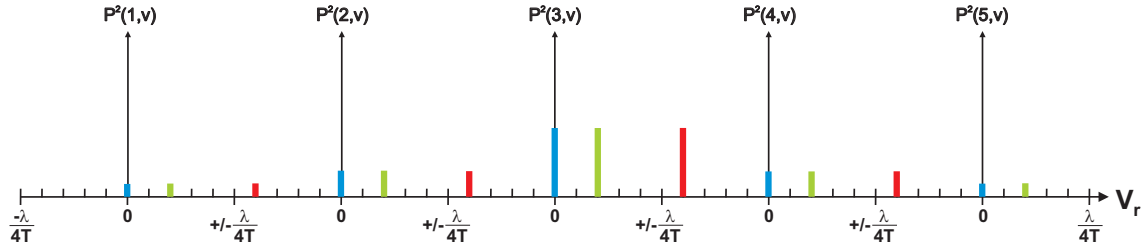


Figure 3.4: Concatenating all single range gate Doppler power spectra $P_i(f_j)$ (see Fig. 3.3) gives a continuous Doppler power spectrum for all range gates. $P(i, v)$ gives the correct echo, even if $v > \frac{\lambda}{4T}$, and thus the red echoes of fast moving objects appear at the correct velocities with respect to the correct range gate (compare Fig. 3.3b). Therefore, the ambiguity of range and velocity can be resolved as long as the signals of neighboring range gates do not overlap.

where objects approaching the radar cause positive velocities, and objects moving away from the radar cause negative velocities. However, because of the limited frequency resolution of the FFT of a single sweep $M(f_i)$, we only get one spectral line for each range gate as indicated by the gray areas in Figure 3.3a. Each complex component of $M(f_i)$ (given by its amplitude and phase) is therefore the superposition of all echoes within the i^{th} frequency range. Thus, there is an ambiguity between range and velocity, which cannot be resolved by analyzing only one sweep.

Therefore, we separately calculate the FFT of N_{sw} subsequent sweeps. Moving targets change their position during subsequent sweeps, and thus the phase of the mixed signal $m(t)$ changes from sweep to sweep, too. The phase rotates repeatedly with a repetition frequency that is proportional to the target's velocity (see Fig. 3.3b).

In order to get the Doppler spectrum for a single range gate i , we consider the i^{th} component of $M(f_i)$ over N_{sw} subsequent sweeps as a new time-series $p_i(t_j)$, where $t_j = jT$ with $j = 1, \dots, N_{sw}$. By calculating a second FFT of $p_i(t_j)$, we can determine the amplitude for each velocity in the corresponding i^{th} range gate (see Fig. 3.3c). Because $p_i(t_j)$ is complex-valued, its FFT spectrum $P_i(f_j)$ also consists of N_{sw} components resulting in a frequency resolution of $\delta f^p = 1/TN_{sw}$, and the velocity resolution is

$$\delta v_r = \frac{\lambda}{2} \delta f^p = \frac{\lambda}{2TN_{sw}} \quad (3.16)$$

If an object is moving too fast, i.e. $v_r \geq \frac{\lambda}{4T}$, its echo will appear in the wrong range gate. However, due to the repetition time T of the sweeps, the Nyquist frequency of $P_i(f_j)$ is $f_{Ny}^p = \frac{1}{2T}$, and we will have aliasing exactly when the echo appears in the wrong range gate. Thus, a target in range gate i with a Doppler frequency of $f > f_{Ny}^p$ appears in range gate $i + 1$ at a Doppler frequency of $f - f_{Ny}^p$ (see Fig.

3.3c), and especially we have:

$$P_i(f_{Ny}^p) = P_{i+1}(-f_{Ny}^p) . \quad (3.17)$$

Therefore, we can simply concatenate the Doppler spectra $P_i(f_j)$ for all N_D range gates, so that we get a continuous Doppler spectrum $P(f_k)$ with $k = 1, \dots, N_D N_{sw}$ frequency components. With this we can describe the Doppler spectrum as a function of range gate i and velocity v (see Fig. 3.4):

$$P(i, v_r) = P(f_k) , \quad \text{with } k = iN_{sw} + \frac{v_r}{\delta v_r} . \quad (3.18)$$

The still existing ambiguity between range and velocity can be solved, as long as the echoes of neighboring range gates do not overlap. For example, the velocity range given in relation (3.15) can be shifted to $0 \leq v_r < \frac{\lambda}{2T}$, if the sign of all velocities is a priori known to be positive. Finally, considering repeated measurements, we get the time-series of Doppler spectra $P(i, v_r, t)$.

3.3 The Doppler Radar Monitoring System

Continuous monitoring of volcanic activity is a complex task and differs significantly from conducting short-term scientific experiments. Usually, in scientific experiments the measured data is stored locally. The data is processed and analyzed after the experiment, which can be very time consuming. A monitoring system, however, has to continuously transmit the data to an observatory, where it can be stored, processed and analyzed online or at least on a daily basis. In order to keep the system running continuously over long periods of time, maintenance is very important. As instruments are often installed in remote places that are difficult to reach, the system should periodically send some information about its operational status.

3.3.1 Doppler - Radar Setup

At Merapi two FMCW Doppler radar systems have been installed. Both are based on a low-cost commercial rain radar. Figure 3.5 shows an image of one of the radar systems. The actual radar device consists of a transmitter/receiver unit and a signal processing unit. To focus the transmitted signal (50mW), the transmitter/receiver unit is mounted at the focus of a parabolic offset mirror. The offset mirror also collects the reflected signal and feeds it back into the Gunn-diode, which mixes the transmitted and received signal. The mixed signal is then processed by the signal processing unit.

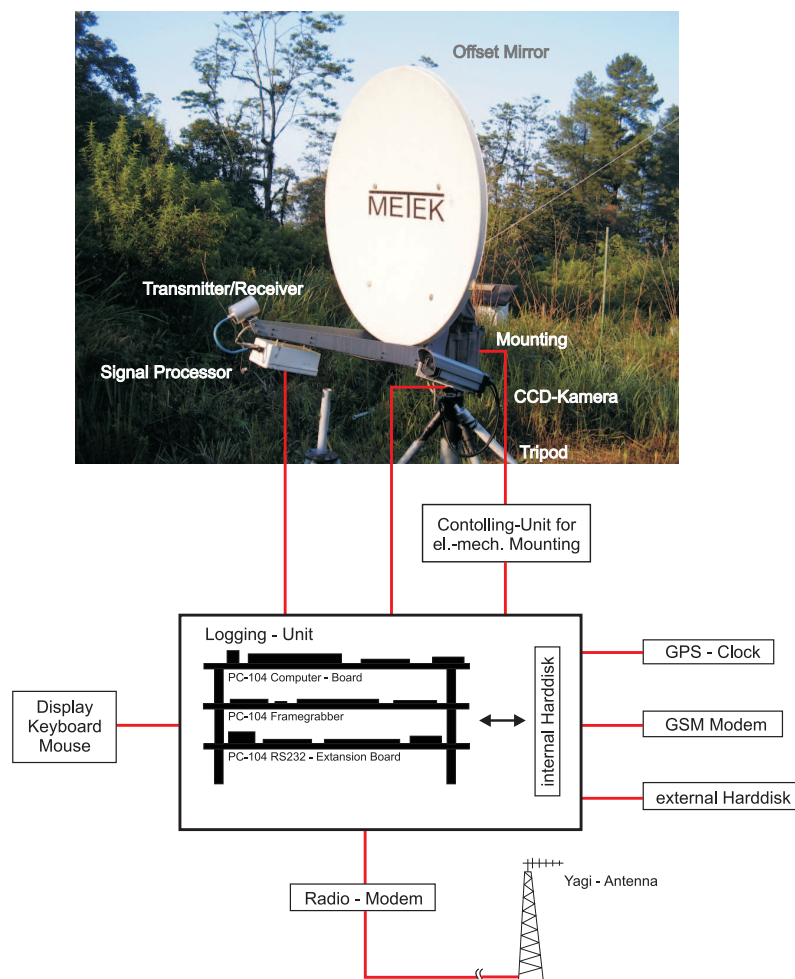


Figure 3.5: Setup of a radar station with additional schematic arrangements. The picture shows the radar device consisting of a 120cm offset mirror, a transmitter/receiver and a signal processing unit. The CCD-camera is attached to the side of the mirror. The electromechanical mounting is able to change the orientation of the mirror/radar/camera assembly in azimuth and elevation. Like the remaining peripheral components, the radar, camera and mounting are connected to the logging unit, which controls the system, stores measured data to disk and sends it to the observatory via radio.

Each frequency sweep of the mixed signal is digitized with 32 samples, thus measurements for up to 16 range gates can be conducted. For each Doppler spectrum 128 sweeps are used, so that each range gate contains 128 spectral lines. The resolution of radial velocities is $0.285m/s$ (see eq. 3.16), and velocity distributions with a width of $36.48m/s$ can be observed without overlapping of neighboring range gates (see Section 3.2). The range gate length can be chosen between 25 and $1000m$. Recording and processing of one Doppler spectrum takes about $50ms$. Individual spectra are stacked for a prescribed amount of time, the so-called integration interval, in order to improve the signal-to-noise ratio. The stacked Doppler spectra are transferred via a serial port to the logging unit. The minimum integration interval is $1s$.

The overall range of the system depends on the size of the offset mirror used to focus the radar beam. For distances up to $1000m$ a small offset mirror ($60cm$ diameter) is sufficient (Hort et al., 2003). At Merapi, however, the distance between radar station and dome is approx. $4.5km$. In this case an offset mirror with a diameter of $120cm$ is required to guarantee a sufficient signal-to-noise ratio.

Most important during the setup of the radar is knowledge of the orientation of the radar beam. Because the opening angle of the $120cm$ offset mirror is 1.5° , a precise alignment of the radar beam is mandatory. Therefore, the radar is mounted on top of an electromechanical mounting. This enables a positioning of the radar beam with a precision of 0.2° . The electromechanical mounting can be accessed by the logging unit via RS232 and a control unit. The mounting is controlled using azimuth and elevation coordinates relative to the instrument's own coordinate system. Since this is fixed, the radar beam can be aligned to previously stored positions without the need of a clear view. Because most of the time the dome of Merapi is covered by clouds, this is very important especially during maintenance work.

Orientation and positioning of the radar beam is controlled by a CCD camera with a zoom lens, which is attached to the side of the offset mirror and whose optical axis is aligned parallel to the center of the beam. The precision of this alignment depends on the configuration of the calibration measurement (see Appendix B). Images of the observed position at the dome can be stored in order to provide a well documented alignment of the radar beam. Images can also automatically be stored on a daily or even an hourly basis, so that visually observable changes at the dome can be documented. In order to align the optical axis of the CCD-camera parallel to the radar beam, calibration measurements are needed. In addition to the parallel alignment of camera and radar beam, these measurements provide an intensity distribution plot that can be overlain onto the camera images. This provides a visual impression of the coverage of the radar beam at the dome. For details about the calibration measurements see Appendix B.

3.3.2 The Logging Unit

The logging unit (Fig. 3.5) controls the whole system and is responsible for a wide variety of tasks: a) Control the radar device and collect data; b) Change radar beam alignment; c) Store data on local harddisk; d) Get images from the CCD-camera; e) Synchronize time; f) Transmission of measured data, images, and status information via radio; g) Send status information via SMS. During measurements, most of these tasks have to be executed simultaneously, requiring a multi-tasking platform. For configurations, beam positioning, and calibration measurements the system needs an easy-to-use graphical user interface.

The computer-core of the logging-unit is a *PC-104⁺* based low-power computer system with a *300MHz* CPU and *128MB* memory. It is fully equipped with an LCD-display, keyboard, and mouse and is operated by Microsoft Windows 2000[®]. The integrated exchangeable harddisk has a size of *80GB*, which is enough to store up to 1 year of data in the current configuration. The system provides a total of 6 COM ports, an Ethernet port and 2 USB ports. It is also equipped with a framegrabber, which is used to collect video images from the CCD-camera attached to the offset mirror.

The radar and the logging unit communicate via RS-232 or RS-422 (Baudrate 115.200) depending on the distance between the instrument and the logging unit. The CCD-Camera is connected via a coaxial cable to the framegrabber. The framegrabber provides live video with 25 frames per second, which is enough for a precise and easy orientation and positioning of the radar beam. For documentation purposes it also takes single images, which can be saved to disk. The system is synchronized to GPS time (UTC) for later correlation of radar data with, e.g., seismic or tilt data. Because the integration interval of the radar systems is usually set to 3 seconds a low cost GPS - clock with a precision of $\pm 0.5s$ can be used, which is also connected via a RS232 port.

The system has to provide the measured data in real-time to the local authorities who are responsible to classify the state of activity of the volcano and send out warnings or evacuate threatened areas. Therefore, the system has to radio the measured data to an observatory, in our case to the MVO, which is located in the city of Yogyakarta about *30km* south of Merapi. Data transmission can be done using multiple logical channels simultaneously, allowing transmission of data from several instruments via the same radio line. The modems are connected to the logging unit via a RS232 connection. In order to transmit all data measured by the radar a special transmission protocol is used (see Appendix A). In addition to radar data, the radio modems can be used to transmit camera images and information about the system's status. The logging unit can also receive basic commands via radio from Yogyakarta, e.g. to reboot the system. For an alternative communication

line the systems have been equipped with GSM modems. Via these modems the logging unit is able to send status information and receive commands as SMSs (Short Message Service). Thus, the system can be controlled from all over the world.

3.3.3 The Observatory Unit

The observatory unit is located in the monitoring room of the MVO, where the data from all monitoring systems installed at Merapi are collected. It's primary task is, of course, to continuously store data measured by the radar systems. Images of the radar system cameras as well as information about the status of the systems can be obtained upon request. Finally, it serves the MVO staff as a platform for processing and analysing of the radar data.

The observatory unit consists of a Windows 2000[©] based computer system and a radio modem to receive data from the radar stations installed at Merapi. To be easily accessible for the MVO staff, it is connected to the MVO's intranet. In case an internet connection is available the system can also automatically send emails, in order to send out status information and images. Currently the observatory unit retrieves data from two radar stations simultaneously. The number of radar systems that can be controlled by the observatory unit is only limited by the radio communication. At the moment we use one radio modem (transmission rate 57.600baud) to receive data from both stations. To reduce the transmission time per Doppler spectrum, the data is compressed to about 25% of its original size before it is sent by the stations.

Instead of storing the data to ASCII-files, it is stored using a client-server SQL database system. Because of its reliability, speed, and good documentation we chose to use the SQL database system called *MySQL*. For each station, the raw data is stored in database tables, each containing one month of data (approx. 550Mbyte). By using index structures, searching datasets by their timestamp is very fast, even for tables of this size. A so-called merge-table provides a logical concatenation of all tables for one station. Thus, datasets of a specific station can be retrieved by only one query to the corresponding merge-table, which takes approximately 5 seconds for 1000 datasets. The database can be accessed via TCP/IP, and thus from every computer inside the MVO's intranet. For this purpose, a client software has been developed that provides easy data access, viewing and processing facilities (see Appendix A).

3.4 System Setup at Merapi

To observe the activity at Merapi's lava dome two Doppler Radar systems were installed on the western flank of the volcano. A first prototype radar station was installed in October 2001 at Pos Babadan. Babadan is located at an altitude of $1280m$ above sea level (asl) and about $4.5km$ away from the active dome (see Fig. 3.6). Being located at the end of a mostly paved road, Babadan can easily be reached by car. It is an official observation post of the MVO and is continuously occupied by a staff member. In addition, Babadan is connected to public power lines, making power supply a much easier task. The prototype station had no electromechanical mounting and no video camera. Data transmission was also limited to pre-processed data, i.e. the total echo power of each range gate. In August 2003 the station has been upgraded, and all components described above were installed. The second radar station has been installed in January 2005 near the former village of Gemer. Similar to Babadan the station is located approximately $4.5km$ from the dome and lies at an altitude of $1305m$ asl. Because of its remote location, this station can only be reached by 4 wheel drive. Here, power is supplied by solar panels.

The two stations differ in one respect. The radar station at Babadan is equipped with the same $24GHz$ Doppler radar that has previously been used at Stromboli volcano. At Gemer a $10GHz$ Doppler radar has been installed. The lower frequency results in a longer wavelength making the instrument less sensitive to small (diameter $< 1mm$) particles. Thus, the station is less affected by ash clouds and rainfall making a detection of dome instabilities easier under such conditions.

When pointing at the dome, the radar beams for both radar stations have a similar elevation angle of about $21-22^\circ$. The opening angle of the radar beams is about 1.5° , and we estimate the slope in the dome area to be tilted about $45-60^\circ$ to the horizontal. Thus, each beam covers an elliptical area of approx. $125m$ width and $250 - 300m$ height. Since the dome is much bigger than this (about $400m$ wide and $200m$ high), a precise alignment of the radar beam is very important for the measurements. For a description of the alignment of radar beam and the camera see Appendix B.

Given the distance of about $4.5km$ to the dome, the range gate length was fixed at $600m$. To reduce the amount of data that has to be transmitted from the radar and stored on disk, only 4 range gates are activated ($1800-2400m$, $3000-3600m$, $3600-4200m$, $4200-4800m$). Figure 3.7a shows a spectrum measured by station Babadan. The last three range gates record activity at the dome and within a few hundred meters distance in front of the dome. In order to detect rain falling at the flank, i.e. having no direct impact to the dome activity, the first range gate observes activities in free air about half way between the instrument and the dome. For the velocity

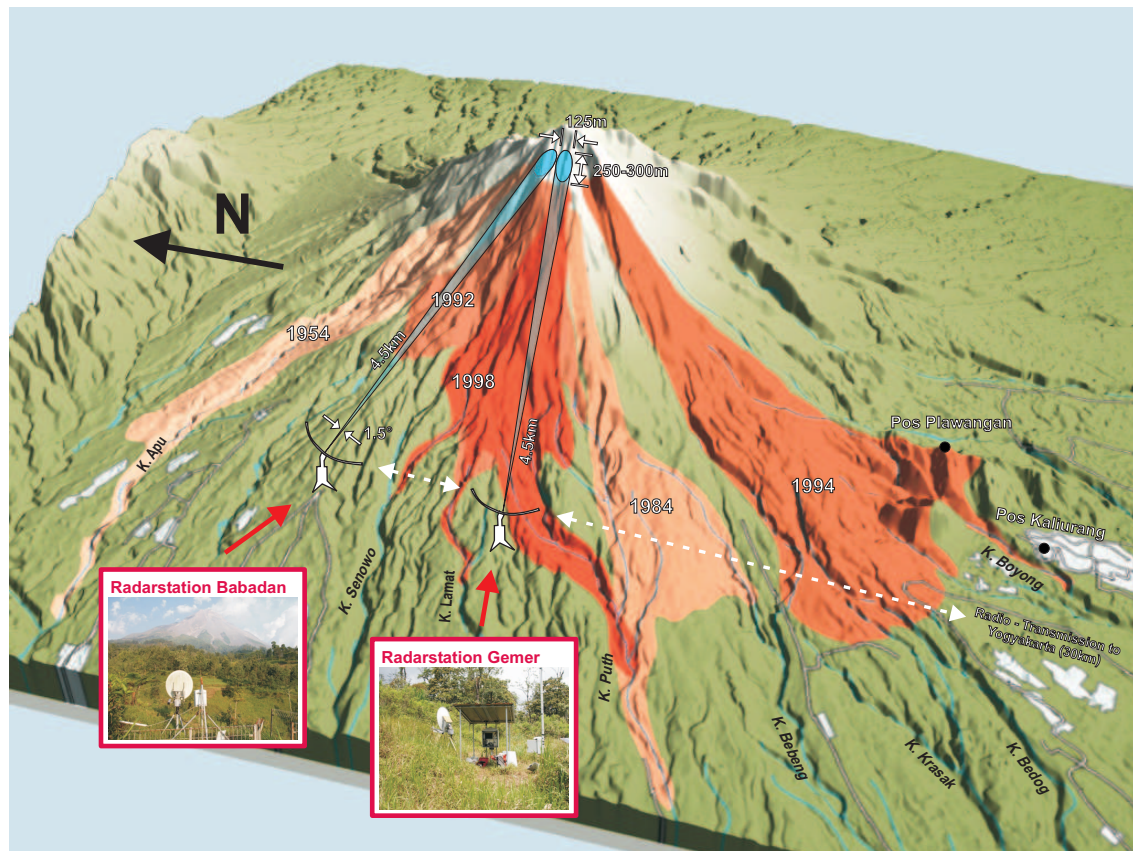


Figure 3.6: System setup at Merapi Volcano. Both stations are located on the western flank of the volcano at a distance of approx. 4.5km , each. Because of the tilted slope each radar beam covers an elliptical area. A direct data transmission from Babadan to Yogyakarta is not possible, thus, the station at Gemer also functions as repeater. Colored areas mark the deposits of dome collapses of the last 50 years (taken from Schwarzkopf and Schmincke, 2000). (Digital elevation model provided by C. Gerstenecker, TU Darmstadt)

range of $0\text{--}36.48\text{m/s}$ we have to assume that only positive radial velocities occur. However, because the elevation angle of the radar beam is quite small, also negative radial velocities are possible, when rain is falling equally tilted due to strong wind. In this case, the range and velocity interpretation shown in Figure 3.7b has to be considered. Because range gates $1200\text{--}1800\text{m}$ and $2400\text{--}3000\text{m}$ are not stored, no negative velocities are available for range gates $1800\text{--}2400\text{m}$ and $3000\text{--}3600\text{m}$.

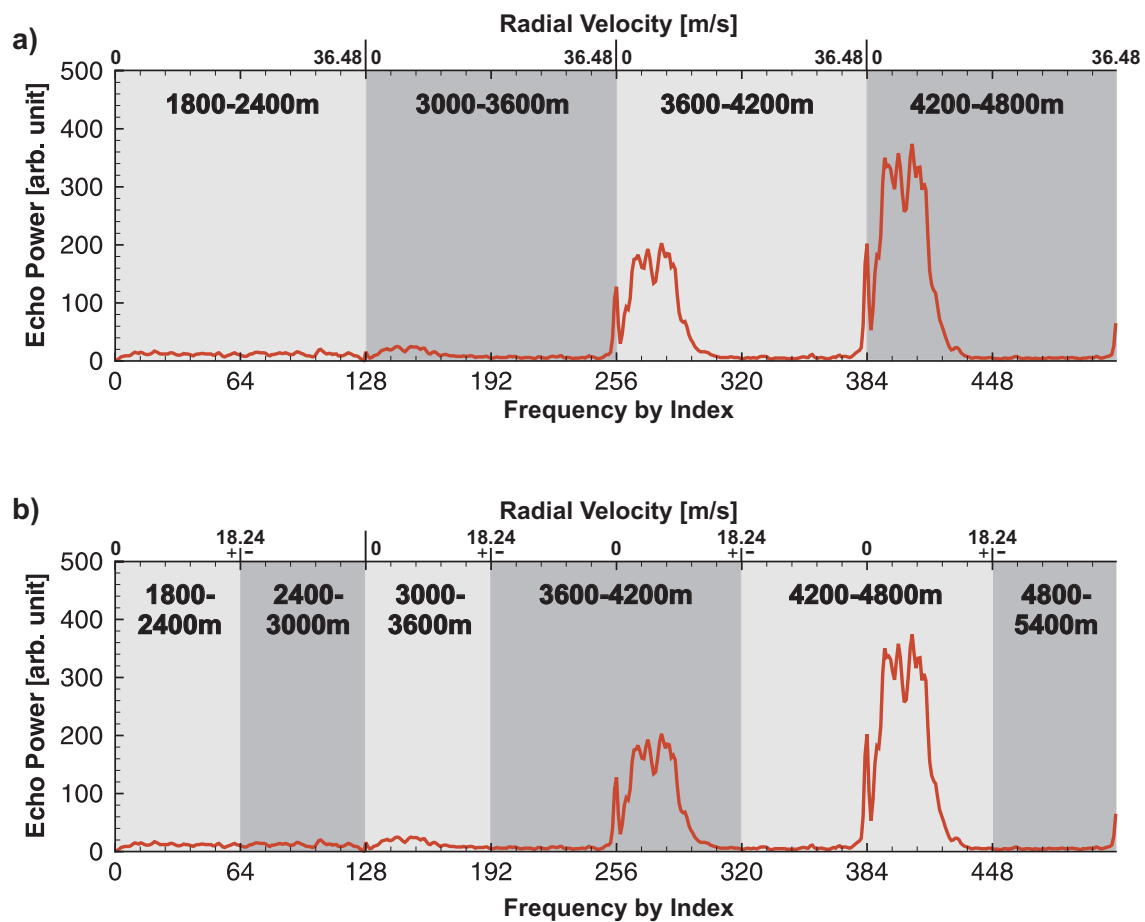


Figure 3.7: Doppler spectrum measured by the radar system at Babadan. (a) shows the original interpretation of distance and velocity for vertical looking rain measurements, where only positive velocities are observed. (b) shows the same measurements as (a) with interpretation of distance and velocity for the measurements at Merapi volcano. Because range gates 3 (1200 – 1800m) and 5 (2400 – 3000m) are not stored, no negative velocities are available for range gates 4 (1800 – 2400m) and 6 (3000 – 3600m). Both plots show a Doppler spectrum of moving dome material. The highest amplitude is observed in the 4200 – 4800m range gate.

3.5 Observations

Active lava domes are highly dynamic systems. The overall dome growth depends on the magma production rate, which can be observed by, e.g. seismic measurements (see e.g. Ratdomopurbo and Poupinet (2000), Hidayat et al., 2000 and Wassermann and Ohrnberger, 2001). The risk of a partial or a full dome collapse, however, also depends on composition of the dome material and the geometry of the dome. An indirect indicator for the stability of a certain part of the dome is the number and the size of instabilities and thus of the resulting rockfalls. Very steep and instable parts of the dome are much more likely to produce a large number of rockfalls or even block and ash flows. In the past rockfalls and block and ash flows could only be detected instrumentally by seismic measurements. However, this has three shortcomings: a) localization of seismic events is not precise enough to attach them to a certain part of the dome, save for the use of arrays, b) during times of high activity with several hundred events per day the duration of several minutes causes events to overlap, and c) seismic records do not directly reveal the instability mechanism.

Doppler measurements are able to overcome these three shortcomings. By focusing on a certain spot at the dome, the two radar systems are able to detect even very weak events. After breaking off the material is moving down the slope of the volcano leaving the radar beam after a short time (usually less than 20 – 30s). Thus, the probability of overlapping events is less likely than for seismic measurements. The Doppler spectra measured by the two radar systems give valuable information about the instability processes and allow the discrimination of different types of instability events. Because of the discrimination of different range gates, the radar measurements also allow the observation of rain falling locally in the dome area, where the installation of rain gauges is extremely difficult. This provides a unique opportunity to analyze the impact of rainfall on dome activity (Voegelé et al., 2006).

As described in Section 3.2, Doppler spectra hold information about echo power as a function of velocity. The amplitude of the echo power is related to the number and size of the particles and thus to the mass moving inside the radar beam. A conversion of the echo power into a total mass is quite difficult and requires knowledge of the particle size distribution and the reflectivity of the material. However, under the assumption that these properties vary only slightly over time, the echo power can be taken as a relative measure of the moving mass. Because the radar beam is pointing directly at the non-moving dome, we would always get very high amplitudes for the echo power of radial velocities near $0m/s$. Since we are only interested in moving material, these amplitudes are suppressed by a filter. To enhance the signal-to-noise ratio, the Doppler spectra are stacked or integrated over a period of 3 seconds.

In order to investigate the evolution of an event, two characteristic values are cal-

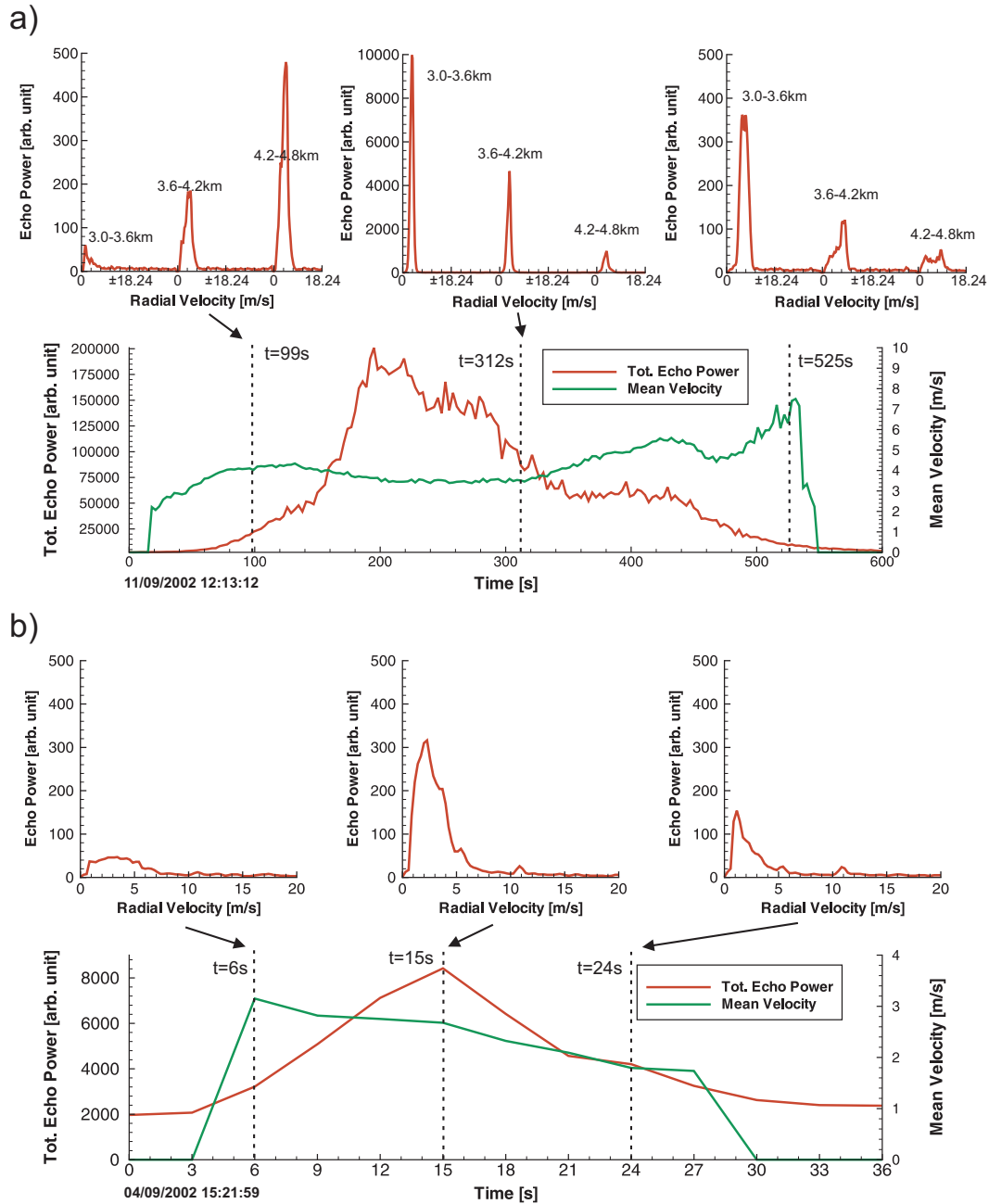


Figure 3.8: Two radar events recorded at station Babadan. (a) shows a typical rain event. The upper plots are Doppler spectra recorded in three consecutive range gates. The lower plot shows the calculated total echo power of the Doppler spectra and the mean velocity calculated from the 4200 – 4800m range gate. (b) shows an event of moving dome material. Here the Doppler spectrum plots focus on the positive velocity axis of the 4200 – 4800m range gate.

culated for each spectrum: the integrated or total echo power and the mean radial velocity. The total echo power of a range gate i at a time t is defined by

$$P(i, t) = \sum_{v_r=v_{\min}}^{v_{\max}} P(i, v_r, t), \quad (3.19)$$

where $P(i, v_r, t)$ is the echo power given by range gate i , radial velocity v_r and time t (Hort et al., 2003). v_{\min} and v_{\max} describe the velocity range that can be resolved in each range gate. The mean radial velocity in range gate i is given by

$$\bar{v}_r(i, t) = \frac{1}{P(i, t)} \sum_{v_r=v_{\min}}^{v_{\max}} P(i, v_r, t) v_r. \quad (3.20)$$

Two kinds of material movement can be observed at the dome: falling raindrops and material breaking off the dome. Figure 3.8a shows a typical rain event. The lower plot shows the evolution of the total echo power (eq. 3.19) and the mean velocity (eq. 3.20) throughout the event. The total echo power rises and decreases slowly. From the Doppler spectra we can see that the ratio of the amplitudes of different range gates changes during the event. At $t = 99s$ the highest amplitude was measured in the range gate extending from 4200 – 4800m. About 3 minutes later at $t = 312s$, the highest amplitude was measured in the 3000 – 3600m range gate. Thus, the target, i.e. rain cloud, has drifted towards the radar system. The shape of the velocity distributions is mainly Gaussian reflecting the raindrop size distribution. The mean velocity (measured in the 4200 – 4800m range gate) is relatively stable at about 3 – 4m/s. However, after about 400 seconds the mean velocity begins to increase slowly to about 7m/s near the end of the event. At $t = 525s$ the velocity distribution in the range gate 4200 – 4800m differs significantly from the Gaussian distribution, which is probably due to stronger winds.

For the movement of dome material we focus on one range gate, because the dome is fixed, and the same range gate will always give the maximum amplitude. Figure 3.7 clearly shows that the highest amplitude for moving dome material is in the 4200 – 4800m range gate. Figure 3.8b shows an event of moving dome material. The total echo power rises and decreases relatively slowly. The sharp increase of the mean velocity is due to the fact that until the echo power reaches a certain amplitude, no reliable mean velocity can be calculated. Starting at 3m/s, the mean velocity decreases only slightly to about 2m/s. The velocity distributions show that the highest echo powers are measured for very low velocities. In the Doppler spectrum the echo power decreases quickly with increasing velocity, and for $v_r > 5m/s$ almost no echo power is detected. The low velocities suggest that the material moves close to the slope and because of the friction of the slope, the moving material cannot accelerate further. Thus, this is interpreted as mostly sliding material.

Figure 3.9a shows an event with higher velocities. Here, the mean velocity rises up to 4.2m/s at $t = 12s$. The corresponding velocity distribution shows high echo

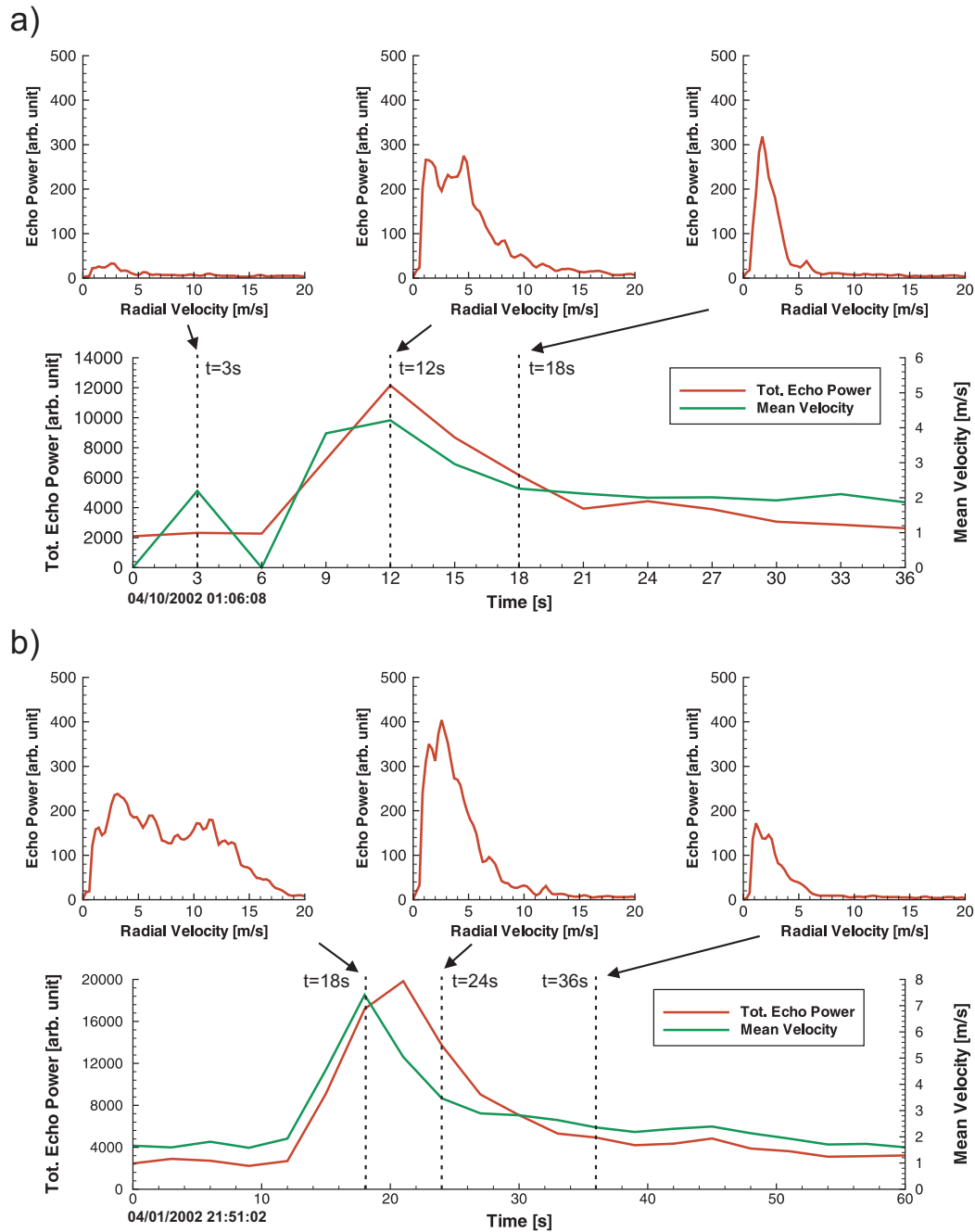


Figure 3.9: Two radar events measured by station Babadan. The upper plots show the positive velocity axis of Doppler spectra from the 4200 – 4800m range gate. The lower plot shows the calculated total echo power of the Doppler spectra and the mean velocity calculated from the 4200 – 4800m range gate. (a) shows an event of material breaking off the dome due to gravitational forces. (b) shows an event where material has been accelerated explosively due to gas overpressure.

power for velocities up to $10m/s$. The higher velocities may be due to either a variation in the particle sizes or, since the measured radial velocities are a function of the true velocity and the angle between the direction of movement and the radar beam, to material moving in a broader range of angles. When material breaks off the dome and fragments, bigger fragments can bounce off the slope and reach higher radial velocities, before they hit the slope again. Smaller fragments remain on the slope and slide slowly due to increased friction. After only 3 seconds do the higher velocities disappear and we only observe sliding material. For $t = 0s$ and $t = 6s$ no mean velocities can be calculated, because the echo power amplitude is too low.

Some events, however, contain significantly higher velocities that cannot be explained by acceleration due to gravitational forces (Hort et al., 2006). Figure 3.9b shows such an event. Both total echo power and mean velocity rise quickly between $t = 12s$ and $t = 18s$. The velocity distribution at $t = 18s$ is very broad. Similar amplitudes for the echo power are measured for velocities of $1 - 15m/s$. The maximum radial velocity is at about $18m/s$. This maximum value and the wide spread of the velocities cannot be explained by gravitational acceleration (see Hort et al. (2006)). Instead, the material movement must have been initiated by an explosion. Any explosion has a certain opening angle, in which the material is accelerated. The radar measures radial velocities

$$v_r = v_t \cos(\alpha), \quad (3.21)$$

where v_t is the unknown true velocity and α the unknown angle between the radar beam and the direction of the movement. Thus, for a large angle α the radial velocity is considerably lower than the true velocity and material moving perpendicular to the radar beam appears at $v_r = 0m/s$. Because v_r is always lower than v_t , the highest radial velocity with a significant echo power amplitude can be assumed to be less than the true maximum velocity of the explosion. Thus, the maximum velocity of the explosion in Fig. 3.9b is at least $18m/s$. The slightly higher echo power for $1 - 7m/s$ suggest that the explosion coincides with a gravitational break-off of material. Whether the explosion is triggered by a gravitational failure of the dome or vice versa cannot be resolved due to the limited time resolution. At $t = 24s$ the explosive part already disappeared, and the velocity distribution shows only material sliding down the slope.

To evaluate the performance of the radar systems, i.e. the ability to detect dome instability events, we compared the radar data to seismic records provided by Joachim Wassermann, from the University of Munich (see Wassermann and Ohrnberger (2001); Ohrnberger (2001)). In Figure 3.10 seismic and radar data are compared for two events. Here, the radar data is plotted as contours. Both seismic and radar data share the same time axis. The event in Figure 3.10a has a distinct onset at $t = 145s$ in both time series. Significant echo power in the radar data is only detectable for velocities below $5 - 6m/s$. Thus, this is a gravitational instability event, where material breaks off the dome and slides downslope. This interpretation corresponds

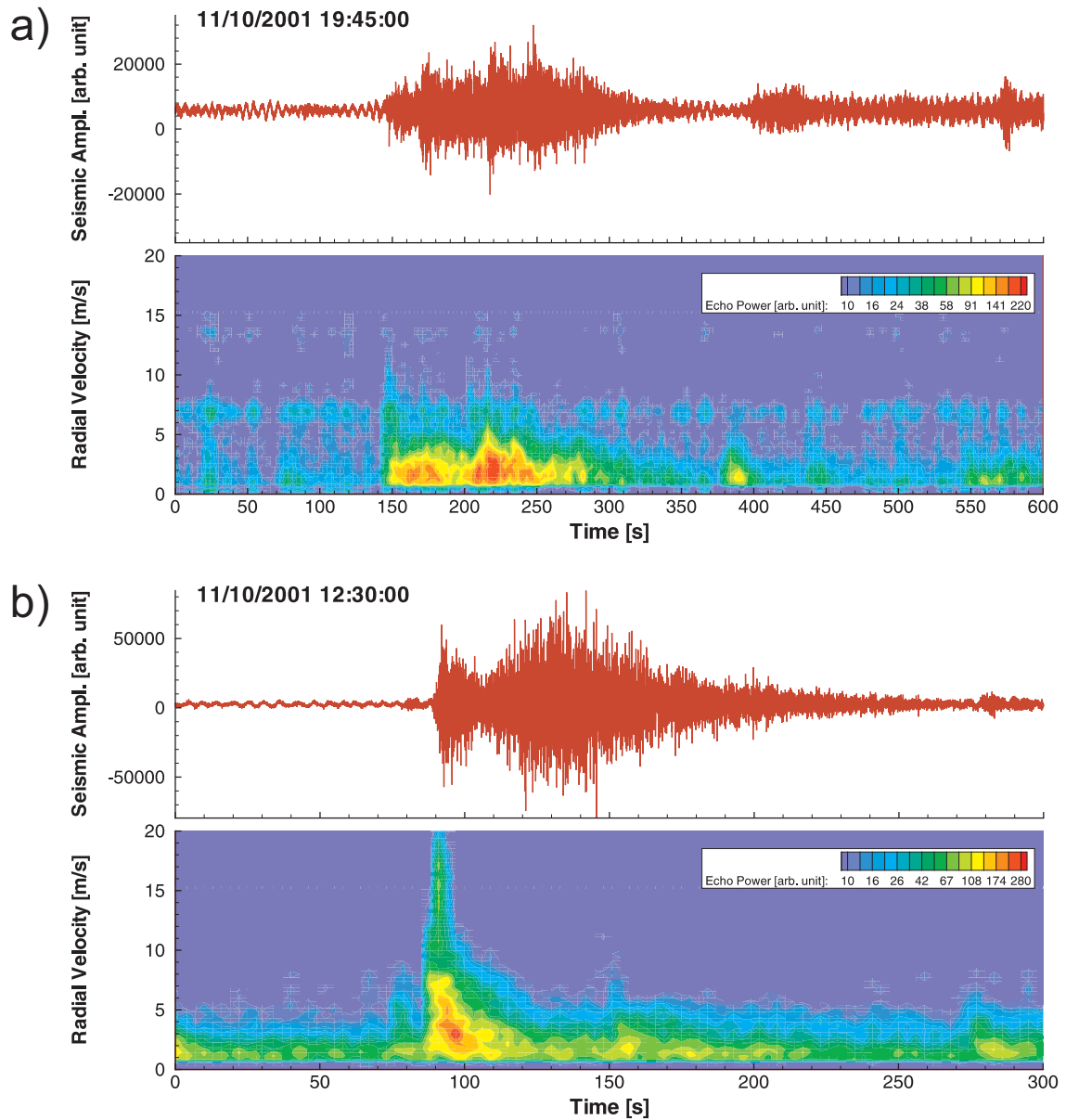


Figure 3.10: Comparison of seismic and radar data for (a) a gravitational, and (b) an explosive instability event. The upper plots show the seismic amplitude recorded at station Pasar Bubar, about 600m from the dome. The lower plots show the corresponding radar data. The horizontal axis represents the time, the vertical axis the velocity and the contour levels represents the echo power. (Seismic data are courtesy of J. Wassermann, pers. comm. 2006)

to the seismic signal, whose envelope rises relatively slowly at the beginning of the event. The event in Figure 3.10b is clearly an explosive instability. At the beginning of the event at $t = 90s$ the echo power rises for velocities up to $20m/s$. After the onset most echo power is measured in the range of $0-5m/s$, which means that during this period the loose material slides downslope. The seismic signal corresponds again very well to this observation. Compared to the event in Figure 3.10a the onset is very sharp, strengthening the interpretation as an explosive outburst. After the explosion the signal is visible for another 150 seconds in the seismic record, which is much longer than the observed time in the radar data. This can be explained by the fact that only the dome is covered by the radar beam. After a short period of time the material leaves the radar beam and slides down the slope of the volcano, where it is still visible in the seismic data. The correlation of radar event type and seismic signal form could be observed for several events. However, a thorough analysis for a larger number of events has yet to be done.

Figure 3.11 shows two comparisons of seismic and radar data, each for a continuous time interval of one hour. Here, the radar signal is plotted as the total momentum, which is calculated by the product of echo power and velocity:

$$Mom(i, t) = \sum_{v=v_{min}}^{v_{max}} P(i, v_r, t) v_r \quad . \quad (3.22)$$

The momentum provides a very good discrimination between noise and events (see Voegelé and Hort, 2006). In Figure 3.11a the correlation between seismic and radar data is very good, almost every peak in the radar data has its counterpart in the seismic data and vice versa. Again, the radar signal shows a relatively short peak for each event, while the events last much longer in the seismic data. The amplitudes of the events do not correlate very well, as events A, B, and C clearly show. While all three events appear to have approximately the same amplitude in the radar data, event B is significantly stronger than A and C in the seismic data. The probable cause of this is the unknown location of the event within the radar beam. Events that occur in the center of the radar beam cause the highest echo power.

Figure 3.11b shows another section of data one hour. Here the correlation between both time series is still good, but event D is only clearly visible in the seismic data, whereas an increase in the radar data can hardly be observed. Thus, the event has not occurred in the center of the radar beam, but at a position, where the transmitted radar signal itself is very weak. Event E shows that on the other hand events are much more likely to overlap in the seismic data, when they follow each other quickly. This happens especially during times of high activity, when a few hundred events can occur each day.

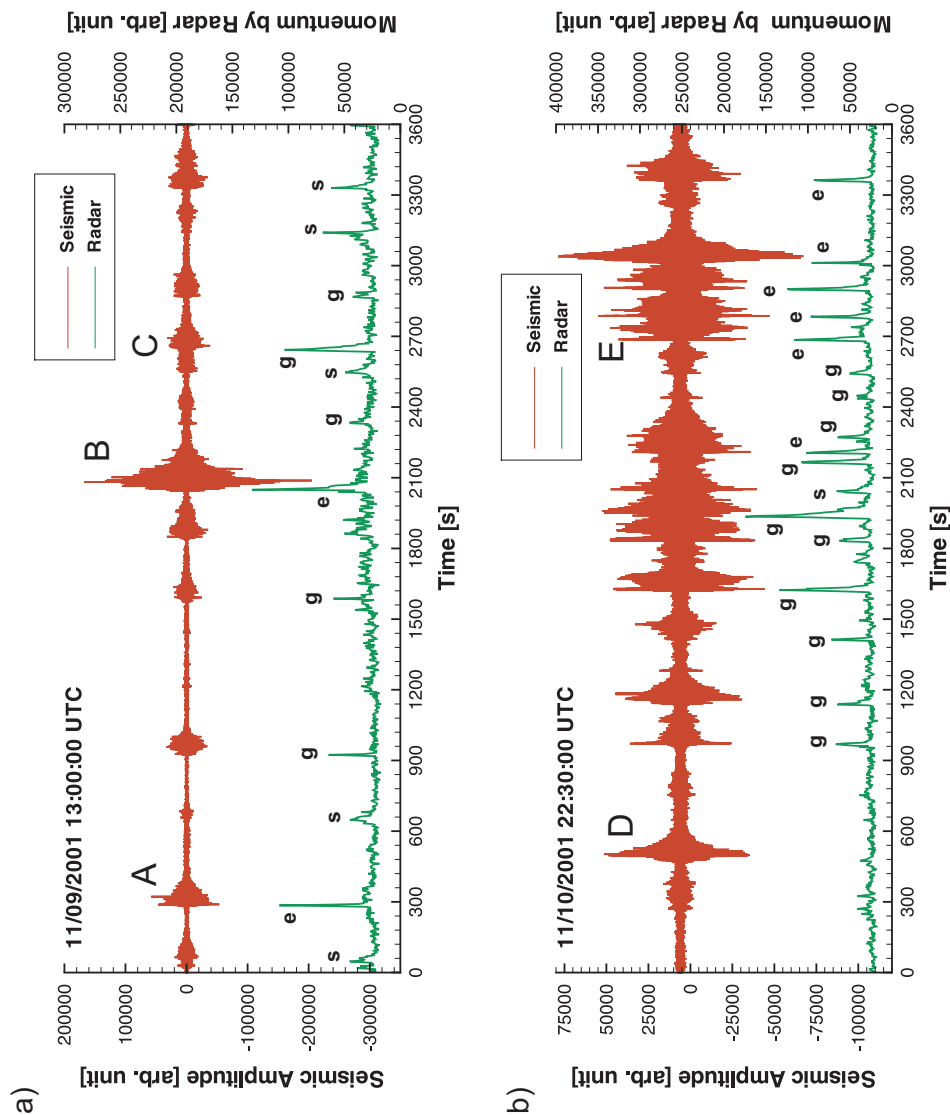


Figure 3.11: Comparison of radar data and seismic records. The radar data was measured at the Babadan station and is plotted as momentum over time. The seismic data was recorded at the station of Pasar Bubar, approx. 600m northwest of the dome. Time in the upper left corner is station time at the begin of the time series. Small letters give the event type according to the radar data: s=sliding material, g=gravitational break-off, e=explosive outburst. Capital letters are referred to in the text. (Seismic data are courtesy of J. Wassermann, pers. comm. 2006)

3.6 Conclusion and Outlook

Although a wide variety of monitoring systems has been installed at Merapi over the last decades, continuous direct visual observation of dome activity is still impossible, because Merapi's summit is often covered by clouds. The Doppler radar is a first approach to enable a continuous, "quasi-visual" observation of lava dome processes. Independent of the visibility conditions, the radar system is able to detect material breaking off the dome generating potentially dangerous rockfalls or block and ash flows. A relative measure of the amount of material involved in the instability events can be given, and information about the dynamic processes causing the instability can be derived from the velocity distributions.

Rockfalls and block and ash flows have been monitored by seismic measurements for many years. A comparison of seismic records and radar measurements shows that the radar technique can enhance the monitoring of such events. A particular advantage of the radar measurements is the short duration of events. During times of high activity seismic events tend to overlap, and especially for events without distinct onset they are difficult to separate from each other. On the other hand, the seismic network at Merapi observes the whole dome area, and thus rockfalls are detected independent of their origin and direction. The setup with 2 radar stations can only observe a relatively small part of the dome. For example the dome collapse in June 14, 2006, occurred to the southeast and was therefore invisible for the two installed radars. To achieve complete coverage for the radar measurements about 5 radar systems would be necessary. However, when combined with seismic measurements, even a single radar system can significantly enhance the monitoring of the location of the most active part of the dome. Consider the radar focused on the most active spot at the dome. When the activity moves to a different location without changing its magnitude, the number of rockfalls in the radar data will decrease, while the events recorded in the seismic data remain constant. The seismics alone would suggest that the activity is not changing, while the radar data would suggest that the activity decreases. A combination, however, would reveal that the activity has merely shifted to another part of the dome, which is crucial information for hazard mitigation.

From the velocity distributions (e.g. Figs. 3.8 and 3.9) we were able to identify different processes, which cause material to break off the dome. During gravitational instabilities, material breaks off due to a structural failure of part of the dome. Because the material is moving close to the slope the material movement is dominated by the friction between material and slope. Therefore, only relatively small velocities are achieved. Especially when the actual break-off is finished, and the material is sliding down the slope, most of the material moves with radial velocities of less than 5m/s . The angle between the radar beam and the material movement has been estimated to be in the range of 38° to 57° (see Hort et al. (2006)). Thus, true max-

imum velocities lie in the range $6 - 9m/s$. During explosive instabilities we observe much higher radial velocities of up to $20m/s$. Because of the broad opening angle associated with explosive outbursts and the uncertain direction of the outburst, we can only estimate that the true maximum velocity is usually at least $20m/s$. The discrimination between gravitational and explosive events is also supported by seismic observation. However, the velocity distributions measured by the radar system give more detailed information on the dominating processes than the seismic data.

The discrimination between multiple range gates provides a way to measure rainfall directly at the dome. The dome area is too hazardous to install rain gauges, and because rainfall might occur very locally, the radar system offers a new source of information to investigate the influence of rain water on dome activity. By storing detailed camera images every hour the system can also help to document visual changes at the dome. When bigger rockfalls or block and ash flows occur, images from before and after the event can be compared. This can help to identify potentially unstable areas of the dome, which can be selected to be monitored by radar.

The radar systems are installed as permanent monitoring systems, and thus a great effort has been made during development to provide stable, reliable systems that can be maintained by the observatory's personnel without intensive training. The radio transmission allows real-time processing of the radar data at the observatory. Because camera images are transmitted upon request, visual observations are also possible at the observatory. Finally, status information can be sent via radio to the MVO and via GSM-modem to each person involved, which helps to maintain the systems efficiently.

In order to provide statistics about the number and size of instabilities on a daily basis, instabilities have to be classified automatically. To achieve this, a software package has been developed, which uses neural network techniques to classify the events (see Voegelé and Hort, 2006). This software has also been integrated into the user interface shown in Figure A.2 in Appendix A.

Future work will include further development of the system infrastructure and, of course, application of Doppler radar monitoring at other dome building volcanoes. Crucial for the monitoring of an active lava dome by Doppler radar is the placement of the system. A safe location within a range of $4 - 6km$ from the dome and direct line of sight to the active area of the dome is needed. The installation of a radar system in a remote area needs a similar effort as for seismic stations, but a radar system has a slightly higher power consumption of about $30W$. Interpretation of the data is straightforward, and it can easily be correlated with other monitoring data. The observations presented in this paper make us confident that radar measurements could significantly enhance the monitoring of dome processes at other dome building

volcanoes, e.g. Soufriere Hills, Montserrat, or Unzen, Japan.

Acknowledgments

We are grateful to the head of the Merapi Volcano Observatory, Antonius Ratdomopurbo, and to the staff of the MVO (especially Agus Sampurno and Anton Sulistio) for their cooperation and continuous support of this project. Thanks to Joachim Wassermann for providing the seismic data that are displayed in Figures 3.10 and 3.11 and to Carl Gerstenecker for providing the digital elevation model of Merapi. Thanks also to A. Gerst, M. Klawonn, and L. Scharff for their help in the field. Discussions with G. Peters, G. Richter and J. Wassermann were greatly appreciated. This work was funded by the Deutsche Forschungsgemeinschaft through grants Ho 1411 13-1, 14-1,2 and 15-1.

Chapter 4

Automatic Classification of Dome Instabilities based on Doppler Radar Measurements at Merapi Volcano, Indonesia: Part I

by Malte Vöge and Matthias Hort

Submitted to Geophysical Journal International, 11/2006

Abstract

Monitoring lava dome instabilities is crucial to efficiently monitor active dome building volcanoes. The Doppler radar technique provides a unique opportunity to gather information about the number of instability events occurring at the growing dome and about the dynamic processes that take place during different types of instabilities. So far, three different kinds of processes have been identified: sliding material, gravitational break-offs and explosive outbursts. In addition, Doppler radars provide rain measurements, which can be used to investigate possible correlations between rainfall and dome activity. Two radar systems have been installed at Merapi volcano in October 2001 and January 2005 to continuously monitor dome instabilities. Due to the large number of instability events that occur during times of high activity, manual processing and analysis of instability events is not practical for monitoring purposes. Therefore, an automatic classification system has been developed, which is capable of identifying different kinds of instabilities as well as rainfall. Two different kinds of classifier models have been applied: (a) neural network and (b) K-nearest-neighbor classifier model. Both classify Doppler spectra according to the underlying dynamic process, i.e. rain, sliding material, gravitational break-off or explosive outburst. The classifiers are able to identify disturbances, which have no

physical source, but are merely artifacts from the radar device itself. Because radar events are sequences of Doppler spectra, a rule set has been defined, which finally determines the event class. In this paper we present the theoretical background for the classification methods as well as details for the given application. All classifiers have been trained and tested on independent data sets to estimate the classification performance.

4.1 Introduction

Merapi volcano is one of the most prominent examples of dome building volcanoes. It is located in central Java, Indonesia, and due to its continuous activity and high population density in the volcano's vicinity, it is considered one of the most dangerous volcanoes worldwide. The lavas of the strato-volcano are of basaltic andesitic composition. Because of its high viscosity the lava forms a dome within an older crater (Voight et al., 2000). The typical eruption style of Merapi is dome extrusion accompanied by partial dome collapses. Dome collapses result in (Merapi-type) pyroclastic flows with run-out distances of several kilometers. Because temperatures reach up to about 500°C (Voight and Davis, 2000) they are particularly hazardous, and due to the high population density fatalities are not seldom. Therefore, Merapi has been continuously monitored for many years using a wide variety of measurement techniques (see e.g. Ratdomopurbo and Poupinet, 2000, Wassermann and Ohrnberger, 2001, Rebscher et al., 2000, Zimmer et al., 2000, Friedel et al., 2004 and Lavigne et al., 2000a).

In order to enhance monitoring of rockfalls and block and ash flows we installed 2 Doppler radar systems at the western flank of Merapi, the first in October 2001 at Pos Babadan and the second in January 2005 at Pos Gemer (see Voege and Hort, 2007). Through measuring the velocity distribution of material movements inside the radar beam, the systems provide useful new information about the processes causing material to break off the dome (see Hort et al., 2006, and Voege and Hort, 2007). So far, selected events have been analyzed manually, and three different types of events have been identified. However, due to the large amount of rockfalls and block and ash flows during times of high activity (several hundreds each day) there is a strong need for an automatic classification of different types of radar events. In recent years similar systems have been implemented for different geophysical observations (see e.g. Dowla et al., 1990, Falsaperla et al., 1996 or Ohrnberger, 2001). Most of them are based on pattern recognition systems that basically consist of five components: (a) sensing, (b) segmentation, (c) feature extraction, (d) classification and (e) post-processing (Duda et al., 2001). The measurement principle is shortly revised in Section 4.2, and in Section 4.3 we summarize the different types of events. Segmentation describes the task of identifying events, i.e. separating single events

from background noise and from each other, which is described in Section 4.4.

One of the most important tasks in pattern recognition is feature extraction. The purpose of feature extraction is to reduce the data by measuring certain *features* or *properties*, whose values are very similar for objects of the same category and very different for objects of different categories. When more than one feature is extracted, each object is represented by a *feature vector* x , where x is in a d -dimensional Euclidean space \mathbb{R}^d . The task of the classifier component is to use the feature vector provided by the feature extractor to assign the object to a class or category. Because perfect classification performance is usually impossible, a more general task is to determine the probability for each of the possible categories. This approach is based on the Bayesian decision theory. In order to determine the probability of an object being of a certain class, two different methods have been used: the K-nearest-neighbor method and neural networks. Although the Bayesian decision theory, the K-nearest-neighbor method and neural networks are state-of-the-art in the field of pattern recognition, we summarize these topics in Sections 4.5–4.6, because they play a key role throughout this paper. When all probabilities are determined, the post-processing task finally decides, to which category the object belongs, given the probabilities calculated by the classifier.

The goal of this paper is to present a procedure to classify different types of radar event, i.e. a sequence of Doppler spectra which significantly differ from background noise. However, it is difficult to define a feature vector of fixed size characterizing all kinds of radar events, because they can differ very much in duration, and because a dome instability event can consist of different consecutive processes. Therefore, we first classify single Doppler spectra according to the underlying process. In order to achieve the best possible classification performance both neural network and K-nearest-neighbor classifiers are tested with different training parameter sets (Section 4.8). When all Doppler spectra of an event are classified, we analyze the resulting sequence of class labels to determine the event class, i.e. the event type (Section 4.9). Because the radar station at Pos Gemer has not collected enough data for a sufficiently large training set, in this paper we focus on the classification of events detected by the radar station at Pos Babadan.

4.2 System Description

The radar system is a frequency modulated continuous wave (FMCW) Doppler radar, which sends out electromagnetic waves with a base frequency of 24GHz . Assuming the particle sizes of the objects do not vary significantly, the amplitude of the received echo power roughly scales with the volume of the reflecting objects (see e.g. Seyfried and Hort, 1999). From the received signal the system repeatedly (at

v_r	Radial velocity
$P(i, v_r)$	Echo power for velocity v_r in range gate i
$P(i)$	Summed echo power in range gate i
Mom(i)	Momentum in range gate i
m_r	Statistical moment of order r
μ	Mean
σ^2	Variance
Skew	Skewness
Kurt	Kurtosis
ω_i	Classes/categories
x	Feature vector
$p(x)$	probability density
$p(x \omega_i)$	State-conditional probability density
$\mathcal{P}(\omega_i)$	Prior probability
$\mathcal{P}(\omega_i x)$	Posterior probability
α_i	Classification action
$\lambda(\alpha_i, \omega_j)$	Loss function
$R(\alpha_i x)$	Expected loss/conditional risk
$\alpha(x)$	Decision function
R	Overall risk
$g_i(x)$	Discriminant function
\mathfrak{R}	Area of the feature space
V	Volume of an area of the feature space
N	Number of training samples
K	Number of samples considered for K-nearest-neighbor estimate
x_i	Input layer units of neural network
y_j	Hidden layer units of neural network
z_k	Output layer units of neural network
t_k	Desired activation/output of output unit k
a_j, a_k	Weighted sum of inputs to hidden/output units
w_{ji}, w_{kj}	Network weights between input-hidden/hidden-output nodes
δ_j, δ_k	Sensitivity of hidden/output units
E	Error function
η	Learning rate
$\Delta w_{ji}, \Delta w_{kj}$	Weight updates
m	Index of learning cycle

Table 4.1: Table of symbols.

Merapi every 3 seconds) calculates averaged Doppler spectra, which hold information on how much echo power has been reflected by objects with certain Doppler frequencies. The Doppler frequency gives two kinds of information about the reflecting object: distance and velocity. The distance measure is very coarse and a maximum of 16 so-called range gates of equal length can be used. Each range gate consists of 128 Doppler frequencies, which are proportional to the object's velocity component in direction of the radar beam, i.e. the radial velocity v_r . The first Doppler frequency of each range gate corresponds to a radial velocity of $v_r = 0m/s$. The velocity resolution is $\Delta v_r = 0.285m/s$.

Figure 4.1 shows a Doppler spectrum measured by the radar. The spectrum consists out of 4 range gates and thus out of 512 frequency components in total, each giving the echo power received for the particular frequency. The frequency axis has an ambiguous meaning and represents a combination of distance and velocity. The radars at Merapi are configured with a range gate length of $600m$, and range gates 4,6,7 and 8 are recorded ($1800-2400m$, $3000-3600m$, $3600-4200m$ and $4200-4800m$). Originally being designed for vertical looking rain measurements, where only positive velocities (towards the radar) are observed (Fig. 4.1a), each range gate has a velocity range from $0 - 36.48m/s$. At Merapi, however, the elevation angle of the radar beam is only about 21° , and especially when rainfall is influenced by strong winds, negative velocities have to be taken into account. Because of the ambiguity of range and velocity, a negative velocity of, e.g. $10m/s$ corresponds to a positive velocity of $36.48 - 10 = 26.48m/s$ in the left neighboring range gate. However, as long as signals in neighboring range gates do not overlap and additional knowledge is available, e.g. about the general direction of the movement, this ambiguity can be resolved. (for details see Voegelé and Hort, 2007). Figure 4.1b shows the interpretation of range and velocity used at Merapi. Each range gate has a velocity axis extending from $-18.24m/s$ to $+18.24m/s$. Because range gates 3 and 5 are not stored, no negative velocities are available for range gates 4 and 6. Instead, negative velocities are available for range gates 3 ($2400-3000m$) and 9 ($4800-5400m$). However, these are not relevant for monitoring of dome activity, because they provide no echoes for dome instabilities. For further details on the measurement principle see Voegelé and Hort (2007).

4.3 Types of Radar Events

Doppler radar measurements provide a unique opportunity to analyze the underlying dynamic processes of dome instabilities. Most important for the characterization of the processes is, of course, the shape of the velocity spectrum in each range gate. A second important aspect is the distribution of the echo power across the range gates, providing information on the location of the event. Since radar events usually

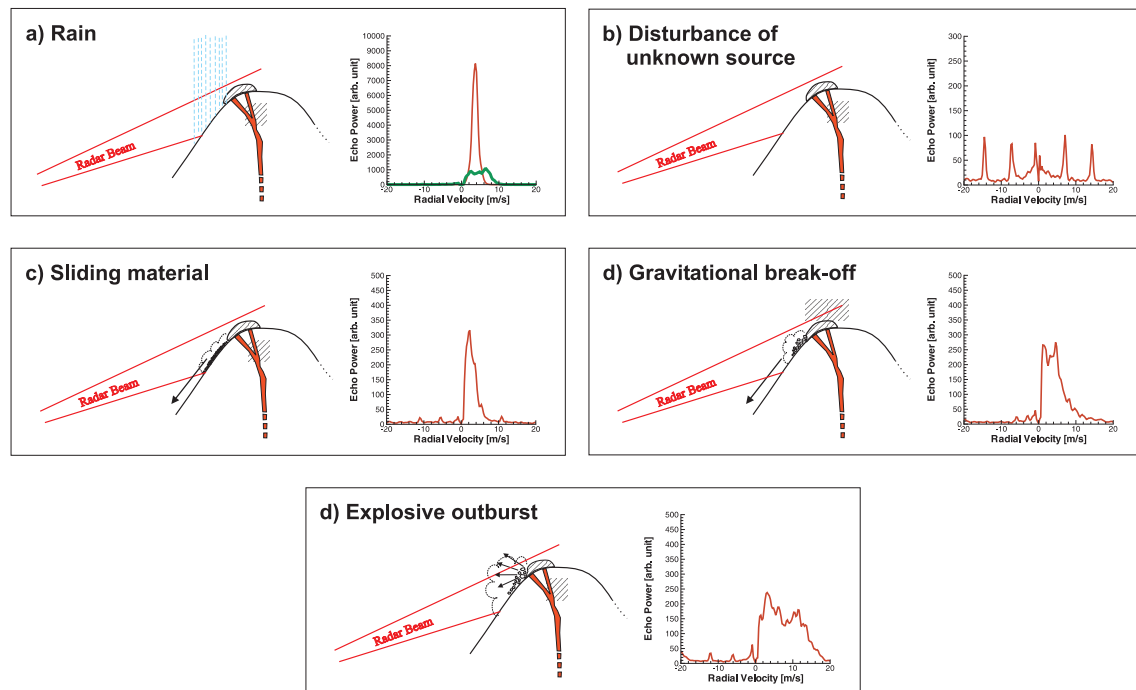


Figure 4.2: Types of Doppler spectra observed at Merapi volcano and sketches of the corresponding dynamic processes. The source of disturbances as shown in (b) is not known. However, a material movement in the dome area is highly unlikely.

efficient feature vectors for the classification.

4.3.1 Rain

The first type of radar event is simple rainfall. Because rainfall can fill a large part of the radar beam and liquid water has strong dielectric properties, the echo power is usually very high. The Doppler spectrum of a typical rainfall looks like a Gaussian peak (see Fig. 4.2a). The measured radial velocities mainly depend on droplet sizes, but they are also influenced by the direction and speed of the wind (see e.g. Rajopadhyaya et al., 1998, Kollias and Albrecht, 2000 and Kollias et al., 2001). Unlike for pure rain measurements, the radar beam is not oriented vertically upward and therefore the influence of wind on the measured velocities can be very strong. In case of strong wind blowing away from the radar, rain appears to have negative velocities. Sometimes the velocity distribution differs from the typical Gaussian distribution (see Fig 4.2a, green curve), which presumably is caused by turbulences, which influence the droplets direction and velocity. Figure 4.3a shows the temporal evolution of a rain event. The rainfall is clearly visible in all three range gates covering the dome. However, in the beginning the rain is only visible in range gate

7 (3600–4200m) and 8 (4200–4800m). After approx. 50s the rain is also visible in range gate 6 (3000–3600m), where it reaches the largest amplitude. After 400s the amplitude in range gate 8 is already very low, while in range gate 6 we still observe a strong echo. Near the end of the event, after about 500s, only range gate 6 shows an echo. Thus, it seems that the observed part of the rain cloud has moved towards the radar.

4.3.2 Disturbances

Figure 4.2b shows a Doppler spectrum with clearly visible disturbances, or so-called ghost echoes. The echoes show a strong symmetry with respect to the $v_r = 0$ axis and do not change their apparent velocities over time. Figure 4.3b shows that only the amplitude of the disturbances strongly fluctuates. Interestingly, the amplitudes of the disturbances scale with the amplitudes of the static echoes, i.e. echoes from the non-moving dome, ($v_r = 0m/s$, see also Section 4.4). Because static echoes carry no information about material movements they have already been suppressed during preprocessing and thus are not visible in Figure 4.2b and 4.3b. Because the flank of Merapi does not move, the ratio of the amplitudes of static echoes of different range gates does not change, and Figure 4.3b shows that the same holds for the disturbances. The symmetry and especially the correlation with the static echoes rule out any association with material movement. Thus, it is very important to distinguish these disturbances from real material movements, so that they can be ignored during further analyzes.

4.3.3 Dome Instabilities

The main purpose of the system is to observe dynamic processes at the dome. Depending on the process that causes the material to break off the dome, the Doppler spectra have different characteristic shapes. In the following, we will shortly describe the interpretation of three different kinds of Doppler spectra that represent material movements at the dome and characterize three different kinds of instability events.

Sliding Dome Material

Figure 4.2c shows a Doppler spectrum with its highest echo power at very low velocities. Only because the static echoes are suppressed, there is no echo power at $v_r = 0$. The echo power decreases rapidly towards higher velocities, and there is no significant echo power for radial velocities greater than $8m/s$. A comparison with measurements at a target region further down slope of Merapi showed that these

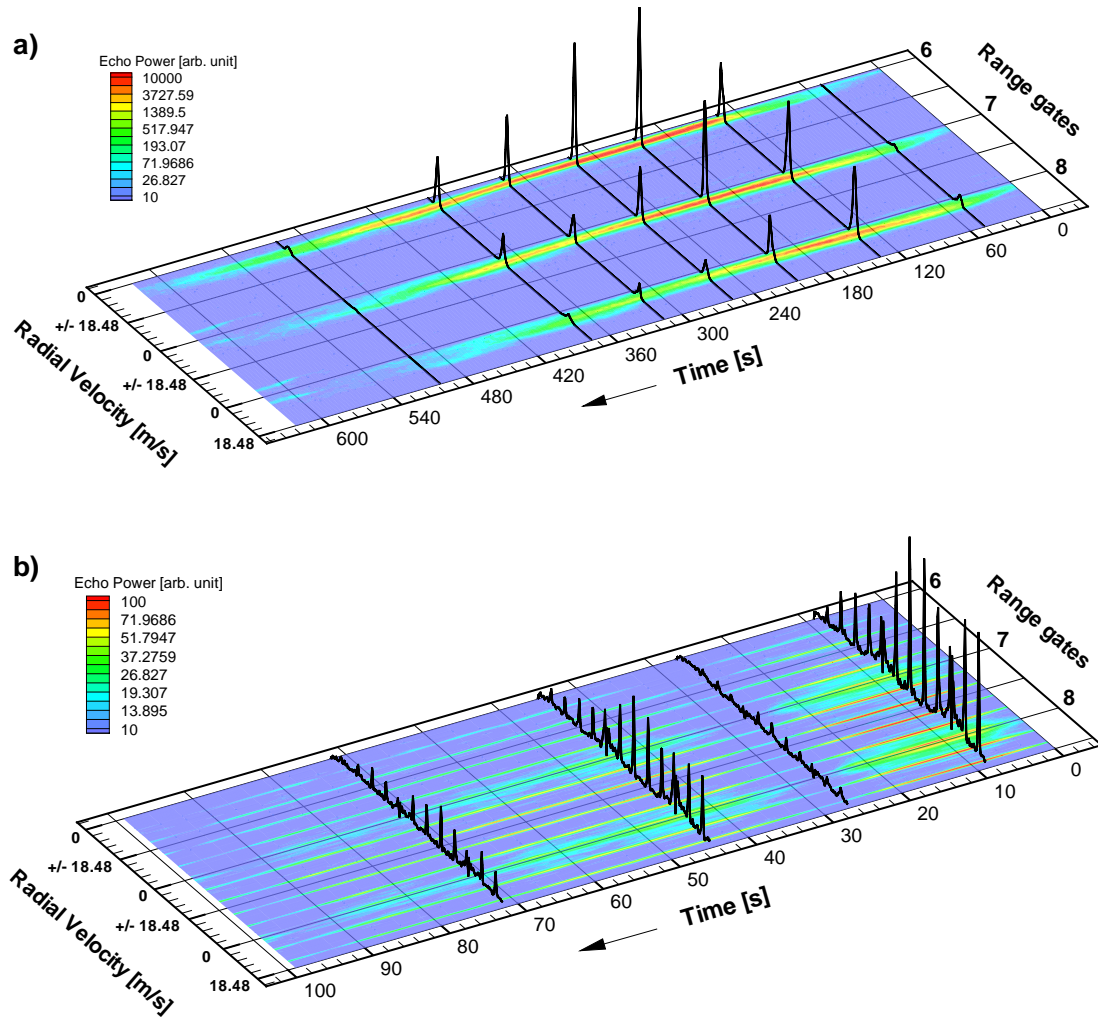


Figure 4.3: Temporal evolution of two radar events in range gates 6 (3000–3600m), 7 (3600–4200m) and 8 (4200–4800m). The rain event in (a) begins in range gate 7 and 8, then moves towards range gate 6. In all range gates the velocity distribution has the same Gaussian shape. The mean velocity is approx. 4m/s throughout the event. (b) shows a time interval with relatively strong disturbances. The so-called ghost echoes appear at the same velocities in all range gates, but vary in amplitude. The stable symmetry with respect to the zero velocity axes is a key aspect for the identification of these disturbances. Please, note the order of magnitude difference in the echo power between rain and disturbances.

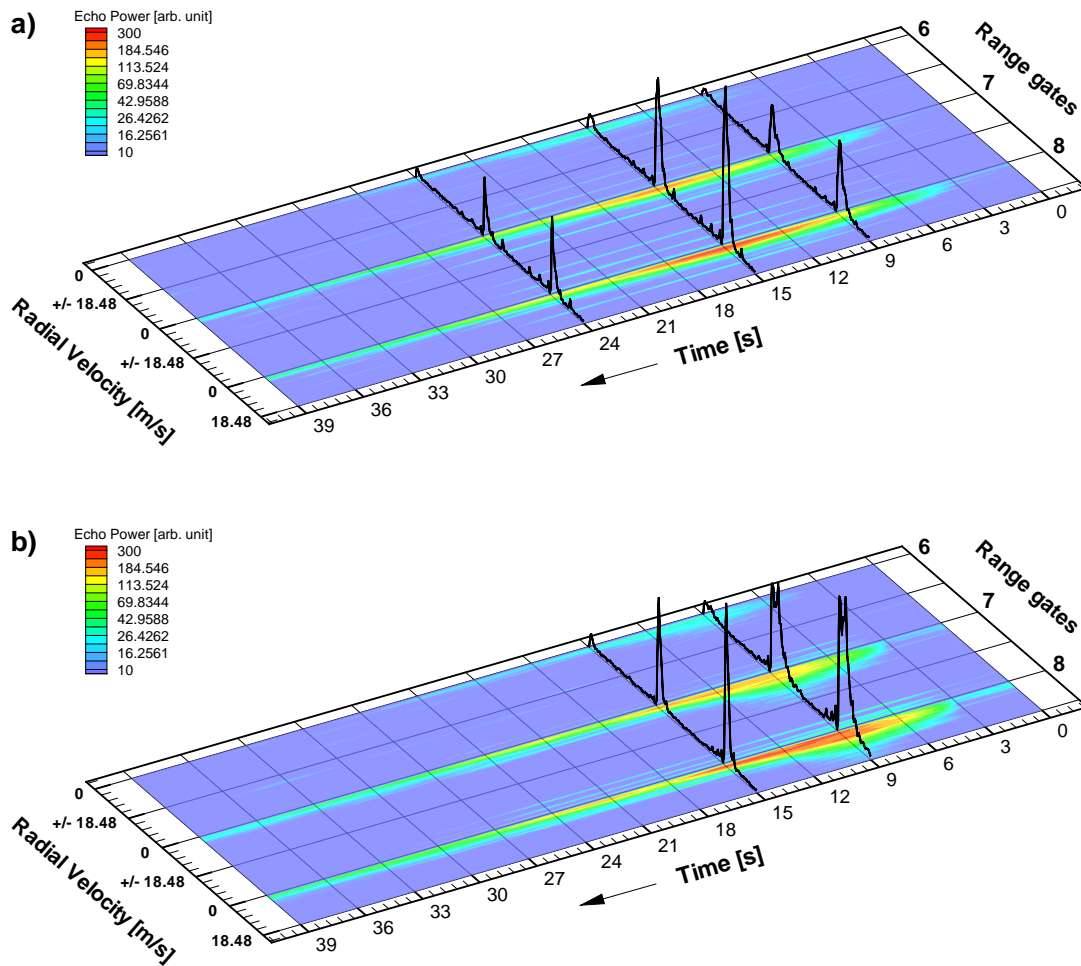


Figure 4.4: Temporal evolution of two radar events in range gates 6 (3000–3600m), 7 (3600–4200m) and 8 (4200–4800m). (a) shows an event of sliding dome material. Throughout the event most of the material is moving very slowly with about 0–4m/s (radial velocity). (b) shows an event with a slightly broader velocity distribution (sec. 6–12), which is interpreted as material breaking off the dome due to gravitation. After second 12 the material is again sliding down the slope and the velocity distributions look the same as in (a).

Doppler spectra are related to material sliding down the slope (Hort et al., 2006). The velocity distributions are not broad, because nearly all material is moving with similar velocities in one direction. Most of the material moves rather slowly because of the friction between material and slope. Some particles or blocks bounce off the slope and reach slightly higher velocities while moving in free air. Figure 4.4a shows that some events exclusively contain sliding material. However, in the following we will see that even when the onset of the event is driven by a gravitational or explosive instability as described below, at the end of the event the released material is always sliding down the slope (see Fig. 4.4b and 4.5a and b). Thus, it is possible that an event registered completely as sliding material has been triggered by those processes above the area observed by the radar.

Gravitational Dome Instabilities

Gravitational instabilities are similar to sliding material. The mean velocity is very low and the maximum echo power is at a velocity near $v_r = 0$. However, compared to sliding material the velocity distribution at the onset of the event is significantly broader and the decrease of the echo power towards higher velocities is less smooth (see Fig. 4.2d). Because of the still rather low velocities, we can rule out that the material has been accelerated by an explosive force and thus is still only driven by gravitational forces. Therefore, the broader velocity distributions at the beginning of the event can have two causes: a) the particles are moving in a broader range of angles, and b) the particle sizes are different. Both can be explained by the initial fragmentation during the break off of dome material. Big fragments are more likely to bounce off the slope and thus to cause higher radial velocities, while smaller fragments remain close to the slope. Therefore, we can assume that for such Doppler spectra the relative amount of bigger fragments is higher than for Doppler spectra representing sliding material. Figure 4.4b shows the temporal evolution of a typical gravitational instability. After the onset with the broader velocity distribution, the fragmented material is sliding down the slope.

Explosive Dome Instabilities

Figure 4.2e shows a Doppler spectrum which has a much broader distribution than those in Figure 4.2c and d. Such a distribution cannot be explained by gravitational acceleration. Hort et al. (2006) show that even if the material originates from above the radar beam gravitational acceleration cannot explain radial velocities above 15m/s (estimated true velocity: $17.8\text{--}25.5\text{m/s}$). Because of the vertical extent of the area covered by the radar beam of about $250\text{--}300\text{m}$, such velocities would be observed for a longer time than only a few seconds. Explosive outbursts at the dome are assumed to be caused by degassing. In most cases the explosive events start with the explosive outburst (Fig. 4.5a), in which case we assume that they are driven from the interior of the dome. In some cases, however, the explosive outburst follows a gravitational instability (Fig. 4.5b), which causes degassing by release of

pressure. In times of high activity, instability events can occur very often, i.e. the time between events can be only a few seconds, or events even overlap. Because it is not always possible to separate overlapping events, we also try to identify events with multiple explosive outbursts (Fig. 4.5b).

4.4 Detection of Radar Events

The first task when classifying radar events is to detect the events and to separate them from background noise. A radar event is defined by a significant increase in echo power in the Doppler spectra, which is related to a material movement inside the radar beam or to a disturbance.

In order to detect events in a time-series of Doppler spectra, we analyze the overall echo power. A first approach is to simply calculate the integrated echo power. Consider $P(i, v_r)$ giving the echo power for the radial velocity v_r in range gate i , the integrated echo power for range gate i is given by

$$P(i) = \sum_{v_r=v_{\min}}^{v_{\max}} P(i, v_r) . \quad (4.1)$$

For the detection of radar events related to material movements in the dome area, we only consider range gates 6, 7 and 8. Thus, the calculation of the total echo power is

$$P_{total} = P(6) + P(7) + P(8) , \quad (4.2)$$

with $v_{max} = 18.24m/s$ and $v_{min} = 0m/s$ for $P(6)$ and $v_{min} = -18.24m/s$ for $P(7)$ and $P(8)$. Figure 4.6d (green line) shows P_{total} for a period of 15 minutes. Figures 4.6a–c show single Doppler spectra at $t = 200s$, $t = 636s$ and $t = 843s$. For simplicity, only the range gate with the strongest echo is shown (range gate 8). Figure 4.6a shows a Doppler spectrum with no significant increase in echo power. Only the background noise is visible and therefore P_{total} is very low. Figure 4.6b shows a significantly increased echo power for positive velocities, indicating a material movement towards the radar. Here, P_{total} also rises significantly. Figure 4.6c also shows an increase in the echo power. However, most of the echo power is measured at velocities near $0m/s$. This is not due to material movement, but is a static echo by the non-moving volcano itself. Usually, such static echoes are suppressed by the signal processing of the radar device. However, due to the large echo from the volcano, slight inaccuracies in the transmit signal generator can cause the suppression to fail, and thus sometimes static echoes still appear. The smaller peaks at ± 2.5 and $\pm 5m/s$ are disturbances as described in Section 4.3.2. While this spectrum should not be considered as significant, P_{total} shows an increase as strong as for $t = 636s$.

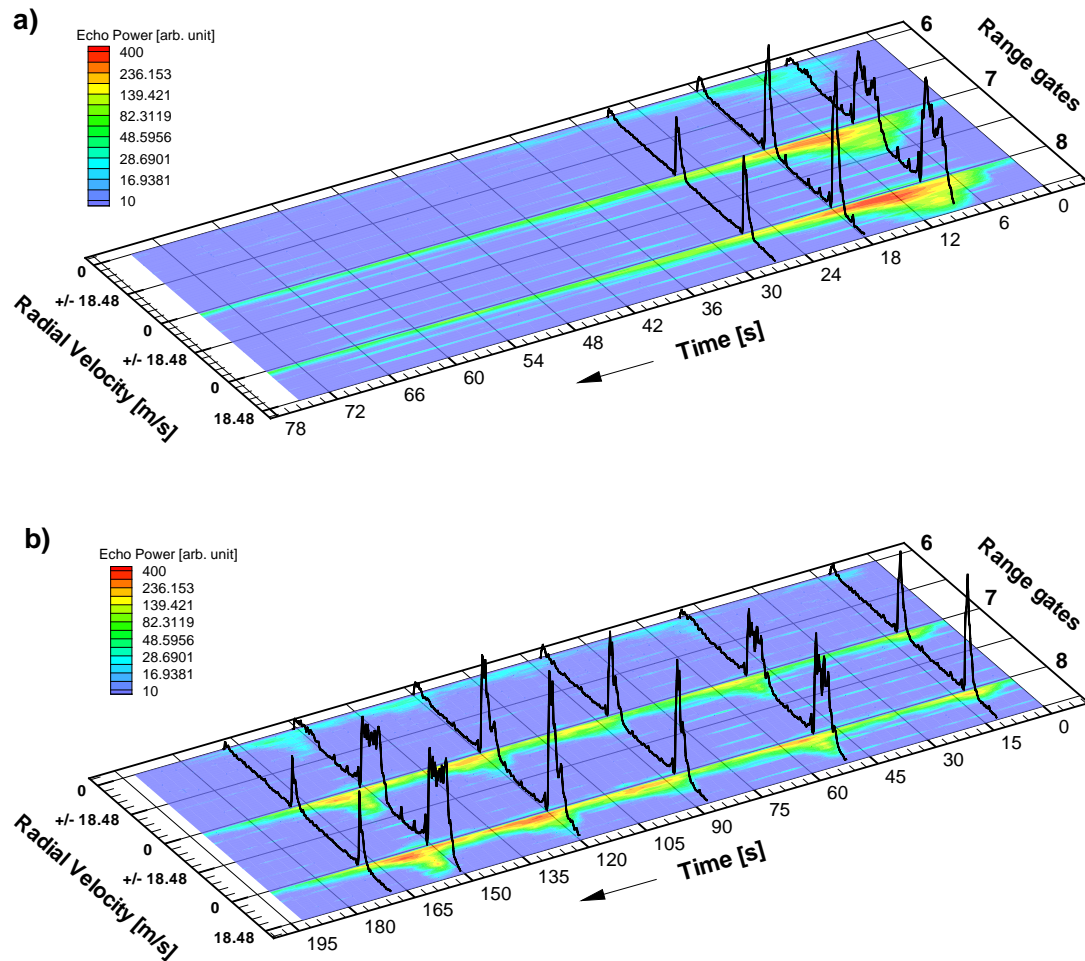


Figure 4.5: Temporal evolution of two radar events in range gates 6 (3000–3600m), 7 (3600–4200m) and 8 (4200–4800m). The event in (a) begins with a very broad velocity distribution with velocities up to 18m/s, which presumably are caused by an explosive outburst. After second 15 the loose material is sliding down the slope. (b) shows a longer time series with mainly sliding material. At second 87 and 120 material is breaking off the dome. Second 51 and 151 show explosive outbursts.

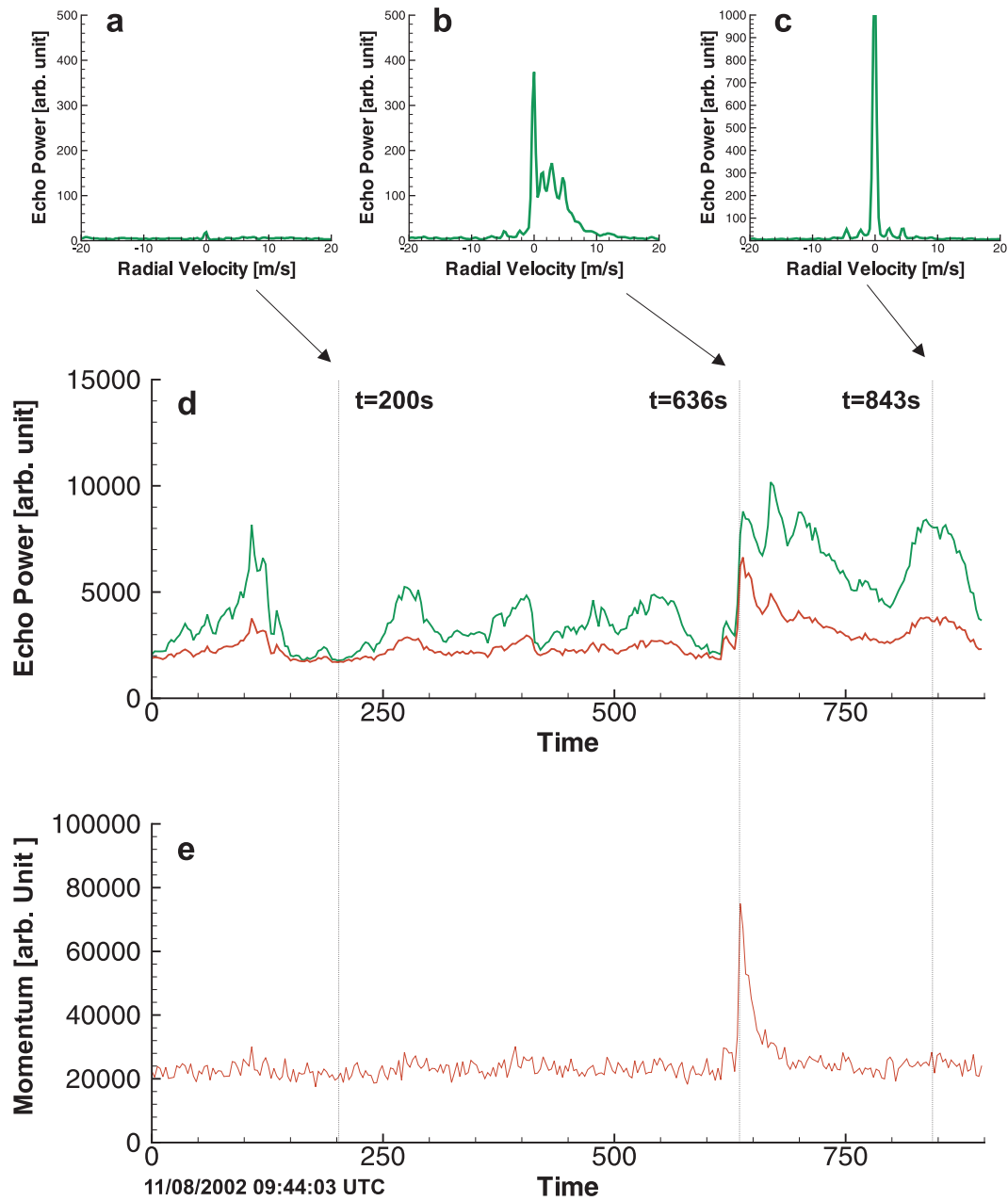


Figure 4.6: Three approaches for the detection of radar events. Plots a–c show three Doppler spectra recorded in range gate 8. While (a) is a pure noise spectrum with no significant echo power, (b) shows a clearly visible material movement. (c) shows a noise spectrum with a strong static echo and so-called ghost echoes, which should not lead to a false detection. (d) shows the calculated total echo power (red: no preprocessing, green: static echoes suppressed) and (e) the calculated momentum for the corresponding time interval. The total echo power does only separate the material movement from unwanted signals, when static echoes are suppressed. However, the momentum is not influenced by ghost echoes and thus gives a much better separation than in (d).

To reduce the strong impact of static echoes, those parts of the Doppler spectra near velocity $v_r = 0m/s$ have to be suppressed when calculating P_{total} . A static echo extends about $\pm 1m/s$ around $v_r = 0m/s$. The easiest way to suppress the static echoes is simply setting the echo power for these velocities to 0. In order to prevent the resulting sharp discontinuities, we use the following definition:

$$P'(i, v_r) = P(i, v_r) \begin{cases} 1 - e^{\frac{-v_r^2}{2\rho^2}} & -1m/s \leq v_r \leq 1m/s \\ 1 & else \end{cases} \quad (4.3)$$

Thus, the echo power for $v_r = 0m/s$ is $P'(i, v_r) = 0$. With increasing/decreasing velocity the influence of the second term decreases exponentially. The parameter ρ is the standard deviation of the Gaussian, which is set to 1.0. Thus, for a velocity of $v_r = 1m/s$ we get $P'(i, v_r) \approx 1/2 P(i, v_r)$. This is sufficient to suppress the static echo at the edges of the influenced velocity range but still leaves some portion of a signal caused by slowly moving targets.

Figure 4.6d (red line) shows $P'_{total}(t)$ for the same period of time. The whole time series is less noisy and the events are better separated from the background noise. But still, there are strong fluctuations, which are caused by ghost echoes. Fortunately, the ghost echoes are approximately symmetric with respect to the $v_r = 0$ axis, which distinguishes them from signals caused by material movements. This symmetry can be used to alter the detection method, so that less disturbances are accidentally detected. Instead of calculating the total echo power, we now calculate

$$\text{Mom}_{total} = \text{Mom}(6) + \text{Mom}(7) + \text{Mom}(8) , \quad (4.4)$$

with

$$\text{Mom}(i) = \sum_{v=v_{\min}}^{v_{\max}} v * P'(i, v) . \quad (4.5)$$

In contrast to $P'(i)$ we now weight each component of the spectrum with its velocity. Since the echo power can be considered to be a rough measure for the mass involved in the movement, $\text{Mom}(i)$ gives a measure of the momentum of the mass movement. The influence of ghost echoes to Mom_{total} is very low. Because of their symmetry the echo power of ghost echoes is equally weighted by positive and negative velocities and thus sum approximately to zero. Figure 4.6e shows that Mom_{total} significantly increases the separation of radar events caused by material movements from noise and disturbances.

The actual detection of events can now be implemented as simple threshold detection. Because all material movements should be detected, independently of whether they have positive or negative velocities, the absolute value of Mom_{total} is calculated and compared to the threshold. Especially for events related to dome activity there is often a sharp increase of Mom_{total} at the onset and a slow decrease at the end of the event. Therefore, two separate thresholds are implemented for the onset and for

the end of an event. By setting the threshold for the onset higher than for the end, we can ensure that only events with a reasonable signal-to-noise ratio are detected, while they are considered to be finished when the signal has decayed to the noise level.

4.5 Bayesian Decision Theory

Bayesian decision theory is the fundamental statistical approach to the problem of pattern classification. It was first introduced by Thomas Bayes (see Bayes, 1763) and is based on quantifying the tradeoffs between various classification decisions using the probabilities and the costs that accompany such decisions. Bayesian decision theory has been the subject of many text books and articles and has been used for a wide variety of applications. For the specific problem of pattern recognition the text books by Bishop (1995) and by Duda et al. (2001) give a fundamental introduction and are the basis for the short derivation presented in the following.

Let $\{\omega_1, \dots, \omega_c\}$ be a finite set of classes/categories and feature vector x a d -component random variable. Then, $p(x|\omega_i)$ describes the state-conditional probability density function for x , i.e. the probability density function for x conditioned on ω_j being the correct category of x . Then, the posterior probability $\mathcal{P}(\omega_j|x)$ can be calculated from Bayes formula:

$$\mathcal{P}(\omega_j|x) = \frac{p(x|\omega_j) \mathcal{P}(\omega_j)}{p(x)} \quad , \quad (4.6)$$

where $\mathcal{P}(\omega_j)$ is the prior probability that the object is of category ω_j and $p(x)$ is defined by

$$p(x) = \sum_{j=1}^c p(x|\omega_j) \mathcal{P}(\omega_j) \quad . \quad (4.7)$$

Bayes formula can be expressed informally by

$$\text{posterior probability} = \frac{\text{likelihood} \times \text{prior probability}}{\text{evidence}} \quad . \quad (4.8)$$

It expresses the posterior probability, i.e. the probability of category ω_j in case we have observed feature vector x , in terms of the prior probability $\mathcal{P}(\omega_j)$, together with the state-conditional probability $p(x|\omega_j)$. $p(x|\omega_j)$ is called the *likelihood* of category ω_j with respect to x , to indicate that the category ω_j , for which $p(x|\omega_j)$ is large, is more "likely" to be the true category. The product of likelihood and prior probability are most important in determining the posterior probability. The *evidence* factor $p(x)$ can be viewed as merely a scale factor that guarantees that the posterior probabilities $\mathcal{P}(\omega_j|x)$ for all categories sum to one.

The goal of Bayesian decision theory is to give a formalism for taking the correct actions for all possible observations. Suppose we have observed a particular feature vector x and we have chosen to take the action $\alpha_i \in \alpha_1, \dots, \alpha_a$. By definition, $\lambda(\alpha_i|\omega_j)$ gives the loss that we incur when taking action α_i , in case ω_j is the true category. Because $\mathcal{P}(\omega_j|x)$ is the probability that the correct category is ω_j , the expected loss taking action α_i is

$$R(\alpha_i|x) = \sum_{j=1}^c \lambda(\alpha_i|\omega_j) \mathcal{P}(\omega_j|x) \quad . \quad (4.9)$$

In decision theory an expected loss is called *risk* and $R(\alpha_i|x)$ is called the *conditional risk*. For each observation, i.e. for each feature vector x , the expected loss can be minimized by selecting the action that minimizes the conditional risk. To verify this rule, assume the *decision rule* or *decision function* $\alpha(x)$, which selects one action of $\alpha_1, \dots, \alpha_a$ for every x . Then, the overall risk R is the expected loss associated with the given decision rule. Given the conditional risk $R(\alpha_i|x)$ the overall risk can be expressed by

$$R = \int R(\alpha(x)|x) p(x) dx \quad , \quad (4.10)$$

where dx is a d -space volume element and the integral extends over the entire feature space. If $\alpha(x)$ is chosen so that $R(\alpha(x)|x)$ is minimized for every x , then the overall risk R is also minimized. Thus, to minimize the overall risk, we first have to calculate the conditional risk $R(\alpha_i|x)$ for each action $\alpha_1, \dots, \alpha_a$ and then select the action α_i that minimizes $R(\alpha_i|x)$. This rule is called *Bayesian decision rule* and the resulting overall risk is called *Bayes risk*.

In a classification problem the actions α_i are usually directly associated with the categories ω_j , i.e. action α_i can be interpreted as the decision to choose category ω_i . In this case, the loss function has to assign high loss for wrong decisions, i.e. $i \neq j$, and low loss for correct decisions, i.e. $i = j$:

$$\lambda_{\text{zero-one}}(\alpha_i, \omega_j) = \begin{cases} 0 & : & i = j \\ 1 & : & i \neq j \end{cases} \quad i, j = 1, \dots, c \quad (4.11)$$

This so-called *zero-one* loss function assigns no loss for correct decisions and a unit loss for any error. Of course, errors have to be avoided, and therefore we have to seek a decision rule that minimizes the probability of errors, i.e. the *error rate*. The corresponding conditional risk for the zero-one loss function is

$$\begin{aligned} R(\alpha_i|x) &= \sum_{j=1}^c \lambda_{\text{zero-one}}(\alpha_i|\omega_j) \mathcal{P}(\omega_j|x) \\ &= \sum_{j \neq i} \mathcal{P}(\omega_j|x) \\ &= 1 - \mathcal{P}(\omega_i|x) \quad . \end{aligned} \quad (4.12)$$

In order to satisfy Bayes decision rule, i.e. to minimize the overall risk, we have to select the action that minimizes the conditional risk for each decision. Thus, we

have to select action α_i that maximizes the posterior probability $\mathcal{P}(\omega_i|x)$, and the rule

$$\text{”Decide } \omega_i, \text{ if } \mathcal{P}(\omega_i|x) > \mathcal{P}(\omega_j|x) \text{ for all } j \neq i.\text{”} \quad (4.13)$$

results in the *minimum-error rate*.

One of the most useful ways to represent pattern classifiers is in terms of *discriminant functions* $g_i(x)$, $i = 1, \dots, c$. The classifier assigns a feature vector x to a category ω_i if

$$g_i(x) > g_j(x) \quad \text{for all } j \neq i. \quad (4.14)$$

A Bayes classifier can easily be represented this way by defining $g_i(x) = -R(\alpha_i|x)$, so that the maximum discriminant function corresponds to the minimum conditional risk. For the minimum-error rate case we would define $g_i(x) = \mathcal{P}(\omega_i|x)$. Because this discriminant function merely chooses the class, which has the highest prior-probability, it is also referred to as *winner-take-all* classification rule. The evidence $p(x)$ does not depend on the category ω_i , and thus an equivalent discriminant function is $g_i(x) = p(x|\omega_i)\mathcal{P}(\omega_i)$.

The structure of a Bayes classifier is determined by the state-conditional probability densities $p(x|\omega_j)$ and prior probabilities $\mathcal{P}(\omega_j)$. Unfortunately, neither the $p(x|\omega_j)$ nor $\mathcal{P}(\omega_j)$ are known in most cases. They have to be approximated, which is usually accomplished using pre-classified training data. While the prior probabilities can easily be approximated by examining, how frequent objects of the various categories occur, this is much more complicated for the state-conditional probability densities $p(x|\omega_j)$. There is a huge number of algorithms for approximating $p(x|\omega_j)$ given pre-classified samples, also called supervised learning. If the density model is known (e.g. Gaussian probability density), parametric methods can be used to determine the parameters for the density function (e.g. *maximum likelihood estimation*). Because in our case the parametric form of the probability densities are unknown, we have to use a non-parametric approach. Two non-parametric approaches have been tested to classify radar events: (a) K-nearest-neighbor method and (b) artificial neural networks.

4.6 K-Nearest-Neighbor Classifiers

Most fundamental techniques for probability density estimation rely on the fact that the probability \mathcal{P} of a vector x falling in a region \mathfrak{R} is given by

$$\mathcal{P} = \int_{\mathfrak{R}} p(x')dx' \quad . \quad (4.15)$$

Thus, \mathcal{P} is a smoothed or averaged version of the density function $p(x)$. Suppose N samples are drawn according to the probability density $p(x)$. The probability that

K of these samples fall in \mathfrak{R} can be estimated by K/N . If we now assume that region \mathfrak{R} is so small that $p(x)$ does not vary significantly within it, we can write

$$\int_{\mathfrak{R}} p(x') dx' \simeq p(x)V \quad , \quad (4.16)$$

where x is a point within \mathfrak{R} , and V is the volume enclosed by \mathfrak{R} . Because K/N is a good estimate of \mathcal{P} , equations (4.15) and (4.16) directly lead to an estimate of the probability density

$$p(x) \simeq \frac{K}{NV} \quad . \quad (4.17)$$

This solution has several problems. If we fix the volume V and take more and more training samples, the ratio K/N will converge, but then we have only obtained an estimate of the (feature) space averaged value of $p(x)$

$$\frac{\mathcal{P}}{V} = \frac{\int_{\mathfrak{R}} p(x') dx'}{\int_{\mathfrak{R}} dx'} \quad . \quad (4.18)$$

In order to obtain $p(x)$ rather than an averaged version of it, $V = \int_{\mathfrak{R}} dx'$ needs to approach zero. However, if we fix the number of samples N and let V approach zero, the region may become so small that it encloses no samples and our estimate $p(x) \simeq 0$ becomes useless. Because the number of training samples is always limited, V cannot be allowed to become arbitrarily small.

This problem is addressed by the K-nearest-neighbor method. Instead of considering a region of fixed volume V , now we let V vary and fix K . Thus, to determine $p(x)$ we consider a hypersphere centered at x and allow the radius of the sphere to grow, until it contains exactly K data points. If the density is high near x , the cell will be relatively small, which leads to good resolution. If the density is low, the cell will grow large, but it will stop soon after it enters a region of higher density.

Together with Bayes formula the density estimation by the K-nearest-neighbor method can easily be used to derive a classification procedure. Consider classes $\omega_1, \dots, \omega_c$ and a data set, which contains N_j data points of class ω_j and N data points in total, so that $N = \sum_{j=1}^c N_j$. To determine the correct class of a new data point x , we draw a hypersphere around it, which encompasses K data points irrespective of their class ω_j . If this hypersphere contains K_j data points of class ω_j , we can approximate the state-conditional densities and the unconditional density in the form

$$p(x|\omega_j) = \frac{K_j}{N_j V} \quad (4.19)$$

and

$$p(x) = \frac{K}{NV} \quad . \quad (4.20)$$

The prior probability can be estimated using

$$\mathcal{P}(\omega_j) = \frac{N_j}{N} \quad . \quad (4.21)$$

Now we can use Bayes formula to give an estimate for the posterior probabilities:

$$\mathcal{P}(\omega_j|x) = \frac{p(x|\omega_j) \mathcal{P}(\omega_j)}{p(x)} = \frac{K_j}{K} . \quad (4.22)$$

Thus, for minimum-error classification we assign each new vector x to class ω_j , for which the ratio K_j/K is largest. This is known as the *k-nearest-neighbor classification rule* and corresponds exactly to the *winner-take-all* rule in Section 4.5. In practice, it involves to find the K nearest neighbors of the new vector x , and then to assign x to the class having the largest number of representatives within these neighbors. For $K = 1$, we have the *nearest-neighbor rule*, which simply assigns a new vector x to the class of the nearest feature vector from the training set.

One disadvantage of the K-nearest-neighbor technique is that all the training data points must be retained, which may lead to problems of computer storage and can result in large amounts of processing to evaluate the density for new data points. Another disadvantage is that the method does not estimate true probability densities, because the integral over the feature-space diverges (Bishop, 1995).

4.7 Neural Network Classifiers

Another approach for building a classifier are neural networks. The idea of neural networks has been inspired by the human brain, which consists of millions of neurons that are connected by synapses. While the functionality of a single neuron is relatively simple, the brain is able to learn and remember by adapting the synapses. In general, for building a neural network, there are no limitations in the choice of network topology. However, the most commonly used type of neural network in pattern recognition is the so-called *multilayer perceptron*. The topology of such a network is organized in successive layers, each consisting of a certain number of neurons, from here on referred to as nodes or units. The input data is presented to the first layer of nodes, called input layer. The last layer is called output layer, because it delivers the resulting data. All other layers are called hidden layers, since they do not directly interact with the environment. Connections are only allowed between nodes of successive layers. Multilayer perceptrons have also the restriction that they are *feed-forward*, which means that the network does not contain feedback loops.

Important for the behavior of a neural network is the model of its nodes. For multilayer perceptrons we use the perceptron model introduced by Rosenblatt (1958). A perceptron computes a single output value from a certain number d of input values and a set bias. Each input of the perceptron is assigned a certain weight. First, the perceptron forms a linear combination of the input values according to its input

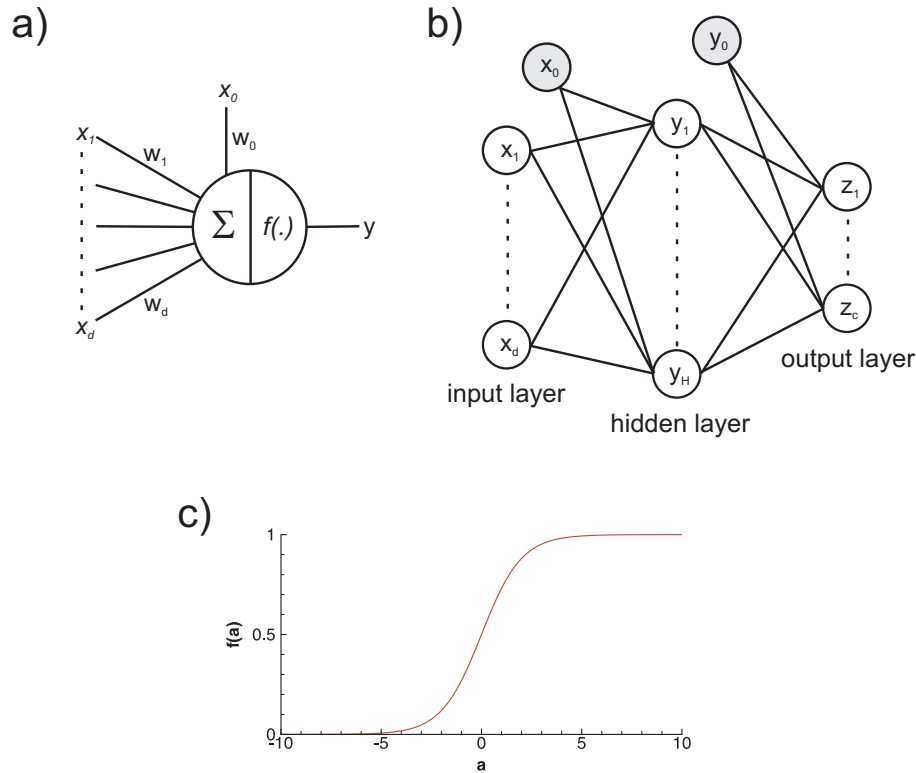


Figure 4.7: Concept of multilayer perceptrons. (a) A perceptron first calculates the linear combination of its input values x_i weighted by w_i . Input x_0 is fixed and set to $x_0 = 1$. Thus, the weight w_0 represents the bias of the perceptron. From the linear combination the output value is calculated by a non-linear activation function $f(\cdot)$. (b) Example of a multilayer perceptron with the input layer, one hidden layer and the output layer. Successive layers are fully connected. Because multilayer perceptrons are feed-forward networks, it contains no feedback loops. The units x_0 , y_0 and z_0 are the bias units. (c) The *logistic sigmoid* activation function $f(a) \equiv \frac{1}{1 + \exp(-a)}$.

weights. From this linear combination the output is calculated using a non-linear *activation function* (see Fig. 4.7a). Mathematically, this can be written as

$$y = f\left(\sum_{i=1}^d x_i w_i + w_0\right) , \quad (4.23)$$

where w_i are the input weights, x_i the input values, w_0 the bias and $f(\cdot)$ the activation function. The bias can be regarded as additional input with a unit value of 1.0 and a weight of w_0 . The activation function most often used in pattern recognition applications is the *logistic sigmoid*

$$f(a) \equiv \frac{1}{1 + \exp(-a)} , \quad (4.24)$$

which is plotted in Figure 4.7c. For small values of $|a|$ the logistic sigmoid function can be approximated by a linear function, thus, in this sense a linear activation function is included as special case. Most important the sigmoid is differentiable, which, as we will see later, is crucial for training algorithms.

Figure 4.7b shows a simple example three-layer network. It consists of an input layer with n_I nodes, one hidden layer with n_H nodes and an output layer with n_O nodes. The layers are fully connected, i.e. each node x_i of the input layer is connected to every node y_j of the hidden layer with the given weight w_{ij} and each node y_j of the hidden layer is connected to every node z_k of the output layer with the weight w_{jk} . With definition (4.23) we can describe the resulting network by

$$z_k = f \left(\sum_{j=1}^{n_H} w_{kj} f \left(\sum_{i=1}^{n_I} w_{ji} x_i + w_{j0} \right) + w_{k0} \right) , \quad (4.25)$$

Despite its simple structure, a three-layer network can describe any continuous function from input to output, given a sufficient number of hidden units, proper non-linear functions and weights (see e.g. Kolmogorov, 1957, Hornik et al., 1992 and Kurková, 1992). Thus, for classification problems we are able to describe any discriminant function by a three-layer network. Although in practice this cannot be achieved with arbitrary accuracy, three-layer networks have provided good performance in many real-life classification problems (Bishop, 1995).

We have to solve several problems, to use a neural network for classification. Obviously the most difficult problem is the choice of the connection weights, which have to be adjusted to fit our training data. The most popular training algorithm for neural networks is called *error backpropagation* (Rumelhart et al., 1986). Starting with an untrained network, a training pattern is presented to the network and the output values at the output layer are determined. These output values are compared to the desired target values and an error is calculated, which minimizes, when the network outputs match the target values. The *training error* on a pattern is considered to be the sum over the squared differences between desired output t_k and actual output z_k :

$$E(w) \equiv \frac{1}{2} \sum_{k=1}^{n_O} (t_k - z_k)^2 , \quad (4.26)$$

where w represents all the weights in the network. The backpropagation learning rule is based on gradient descent. The weights are initialized with random values, and then they are changed in a direction that will reduce the error. Thus, we have to find a procedure to evaluate the derivatives of the error function E with respect to the weights and biases in the network. First, we consider the hidden-to-output unit weights w_{kj} . Each output unit of the network computes a weighted sum of its inputs in the form

$$a_k = \sum_{j=0}^{n_H} w_{kj} y_j , \quad (4.27)$$

where y_j is the activation of a hidden unit. Note that in this notation the bias is introduced as additional unit with index "0" and with fixed activation of "+1". The activation z_k of output unit k is then given by

$$z_k = f(a_k) \quad . \quad (4.28)$$

The error E depends on the weight w_{kj} only via the summed input a_k and activation function $f(a_k)$. Therefore, we can apply the chain rule for partial derivatives to give

$$\frac{\partial E}{\partial w_{kj}} = \frac{\partial E}{\partial a_k} \frac{\partial a_k}{\partial w_{kj}} = \delta_k \frac{\partial a_k}{\partial w_{kj}} \quad , \quad (4.29)$$

where $\delta_k \equiv \frac{\partial E}{\partial a_k}$ is often referred to as *sensitivity* and with (4.27) we get

$$\frac{\partial E}{\partial w_{kj}} = \delta_k y_j \quad . \quad (4.30)$$

In order to evaluate the sensitivity we again use the chain rule and with the definition (4.26) of the error function, we get

$$\delta_k = \frac{\partial E}{\partial z_k} \frac{\partial z_k}{\partial a_k} = \frac{\partial E}{\partial z_k} f'(a_k) = (z_k - t_k) f'(a_k) \quad . \quad (4.31)$$

Together with the *learning rate* η , which defines the step size of the gradient descend, these results give the weight update or learning rule for the hidden-to-output weights

$$\Delta w_{kj} = -\eta \delta_k y_j = \eta (t_k - z_k) f'(a_k) y_j \quad . \quad (4.32)$$

For the input-to-hidden unit weights, this is more complicated. Again by using the chain rule, we get for the derivative of the error function

$$\frac{\partial E}{\partial w_{ji}} = \frac{\partial E}{\partial a_j} \frac{a_j}{w_{ji}} \quad , \quad (4.33)$$

where $a_j = \sum_{i=0}^{n_I} w_{ji} x_i$ is the activation of hidden unit j . The sensitivity of hidden unit j is defined as $\delta_j \equiv \frac{\partial E}{\partial a_j}$ and can be evaluated by yet again using the chain rule:

$$\begin{aligned} \delta_j &= \frac{\partial E}{\partial y_j} \frac{\partial y_j}{\partial a_j} \\ &= - \left(\sum_{k=1}^{n_O} (t_k - z_k) \frac{\partial z_k}{\partial y_j} \right) f'(a_j) \\ &= - \left(\sum_{k=1}^{n_O} (t_k - z_k) \frac{\partial z_k}{\partial a_k} \frac{\partial a_k}{\partial y_j} \right) f'(a_j) \\ &= - \left(\sum_{k=1}^{n_O} (t_k - z_k) f'(a_k) w_{kj} \right) f'(a_j) \\ &= - \left(\sum_{k=1}^{n_O} \delta_k w_{kj} \right) f'(a_j) \end{aligned} \quad (4.34)$$

The sensitivities at the hidden unit are simply the sum of the individual sensitivities at the output units, weighted by the hidden-to-output weights w_{kj} , and multiplied with $f'(a_j)$. Thus, the output unit sensitivities are propagated "back" to the hidden units. The learning rule for the input-to-hidden weights is then

$$\Delta w_{ji} = \eta \delta_j x_i = \eta \left(\sum_{k=1}^{n_O} \delta_k w_{kj} \right) f'(a_j) x_i \quad . \quad (4.35)$$

Like all gradient descent procedures, the behavior of the backpropagation algorithm depends on the starting point. Starting with all weights set to zero would not work, because the back-propagated error would always be zero and the input-to-hidden weights would never change. For this reason the process of learning is usually started with random values for all network weights. Although we have derived the backpropagation algorithm for the special case of the three-layer network, this can also be done for more general feed-forward networks (Rumelhart et al., 1986). Since the introduction of the backpropagation algorithm, several improved versions have been published. Here, we decided to use a relatively simple method for using second-order information to increase training speed, which is called *Quickprop* (Fahlman, 1988). In this method the weights are assumed to be independent, and the descent is optimized separately for each of them. The error surface is assumed to be quadratic and the coefficients for the particular parabola are determined by two successive evaluations of $E(w)$ and $dE(w)/dw$. This leads to the weight update rule

$$\Delta w(m+1) = \frac{\left. \frac{dE}{dw} \right|_m}{\left. \frac{dE}{dw} \right|_{m-1} - \left. \frac{dE}{dw} \right|_m} \Delta w(m) \quad , \quad (4.36)$$

where m is the index of the learning cycles (see Fahlman, 1988). When certain heuristics are imposed, e.g. when the error surface is nearly flat, the method can be significantly faster than standard backpropagation. Another benefit of this method is that each weight has its own learning rate, and thus the weights tend to converge roughly at the same time reducing the problem of nonuniform learning.

There are several different training protocols to train a network by backpropagation. In virtually every case, several passes through the training data are needed to train the network sufficiently. The training protocols can be divided into online training and offline or batch training. During online training the weights of the network are updated after each pattern presentation. In batch training protocol, all patterns are presented to the network before learning takes place. Their corresponding weight updates are summed and then the actual weights are updated. In both cases we have to make several passes through the training data to achieve a well trained network. For backpropagation the online training protocol is usually significantly faster than batch training, especially in the case of large training sets with many similar training examples. Thus, all networks presented in this article have been trained with online training protocol. To make sure that the order of the training patterns has no influence to the training, in each pass or cycle the patterns are presented to the network in random order.

The most common way to represent a discriminant function by a neural network is to define the network topology so that the number of input units matches the dimension of the feature vector and the number of output units matches the number of categories or classes. Thus, each output node z_k corresponds to a category ω_k . For training of the network, the output values of the training patterns are prepared, so that the output value for the correct category is one and all others are zero. In this

application, using the logistic sigmoid activation function has another great benefit: when we present a new pattern to the network, the output values can be interpreted as posterior probabilities for each category to be the true category (Bishop, 1995). However, we have to be cautious with this interpretation, since this holds only, when the network has enough hidden units and when the network weights are trained sufficiently. When, e.g. the output values do not sum to one, they obviously do not represent true probabilities. This mainly happens for samples for a region of the feature space, which is not or only weakly covered by the training data. Ideally, the output of the network will be one for the output node corresponding to the correct category and zero for all other outputs. Because this is not always the case we use the *winner-take-all* rule to determine the classification result (see Section 4.5).

4.8 Single Spectrum Classification

The classification of radar events bears one main difficulty: during an event the underlying process might change, e.g. the explosive onset of an event is usually followed by material sliding down the slope. It is therefore difficult to define features, which provide information about all processes that occur during the event. Another problem is that the duration of events is highly variable, and thus it is difficult to define feature vectors with a fixed number of dimensions. Therefore, we first classify single Doppler spectra according to the underlying processes defined above (rain, disturbances, sliding material, gravitational break off and explosive outbursts) instead of directly classifying complete radar events. When all Doppler spectra of an event have been classified, we can use this information to determine the event class (see Section 4.9).

The conceptual boundary between feature extraction and classification is somewhat arbitrary: an ideal feature extractor makes the job of the classifier trivial; conversely, an omnipotent classifier would not need the help of a sophisticated feature extractor. Therefore, we investigate several different approaches to classify Doppler spectra. They differ in the type of feature vector, the classifier model and the overall classification strategy. First, we will try to build a classifier, which is capable of discriminating all five categories in one step. Using a hierarchical structure as illustrated in Figure 4.8, an alternative approach is to use one classifier to discriminate the categories rain, disturbance and dome instability, and for those spectra classified as dome instability a second classifier determines the sub categories sliding material, gravitational break-off or explosive outburst.

We have tested K-nearest-neighbor (KNN) as well as neural network classifiers. For both classifier models certain parameters have to be chosen. For the KNN classifier model this is just the number K of training patterns, which shall be taken into

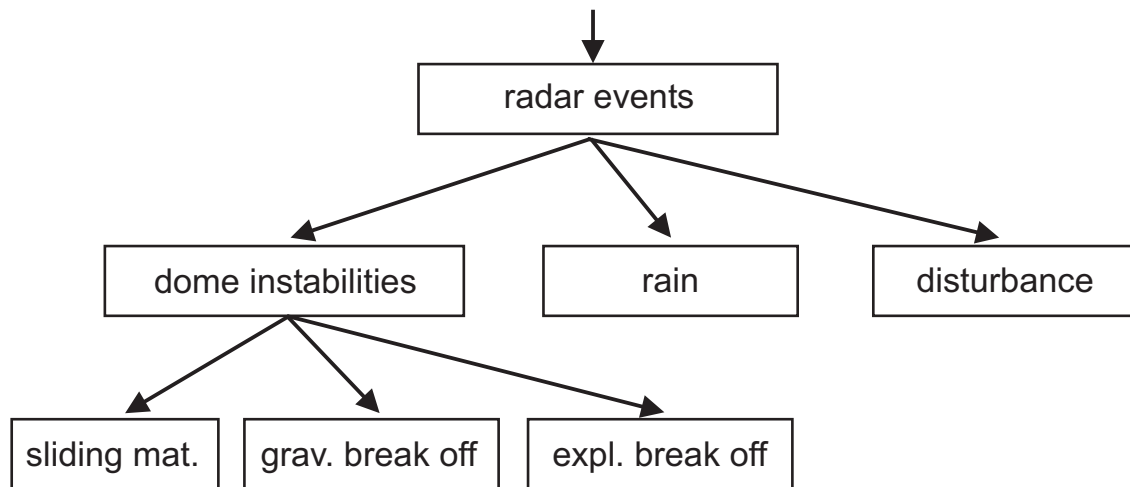


Figure 4.8: Class hierarchy of Doppler spectra observed at Merapi volcano.

account, when determining the posterior probabilities (see Section 4.6). For the neural network classifier model, the most important parameters are the number of hidden units and the learning rate (see Section 4.7). Below we will analyze how these parameters influence the classification results for different types of feature vectors and determine the best choice of model and parameters.

4.8.1 Training Data

The KNN and the neural network classifier model both need supervised learning (see Sections 4.6 and 4.7). Thus, the choice of training patterns is very important to achieve good classification results. Obviously, the more training patterns we use, the better we can train our classifier, because the coverage of the feature space is better. However, in practice we won't have an arbitrary number of training patterns at hand.

Not only the size, but also the composition of the training patterns is important. The relative numbers of patterns of each class determines the prior probabilities in the Bayes formula (see eq. (4.6)). In our case the prior probabilities are not fixed, but change over time. On the one hand, instabilities are much more likely to occur in times of high dome activity than at times of low dome activity. On the other hand, rain events are much more likely in the rainy season than during the dry season. Therefore, we want to consider the prior probability of all types of Doppler spectra to be equal, and we have to make sure that our training data sets consist of an equal number of patterns of all categories. For the generation of the training

data sets, we have selected several hundred Doppler spectra from April and May 2002, since this has been the most active period that we were able to observe so far. For each category 200 spectra have been manually classified.

To validate the accuracy of a classifier we use a procedure called *cross-validation*. The training data is divided into three disjoint sets of equal size. The first set is used as training set to train the classifier. The second set –the validation set– is used to determine the best classification parameters. Thus, the classifiers are somehow influenced by the validation set, which might lead to some over-fitting to the validation set. Therefore, the third set –the test set– is used to evaluate the classification accuracy on a completely independent set of pre-classified samples.

4.8.2 Feature Extraction

In Section 4.3 we discussed Doppler spectra of each type of event, and the characteristic properties have been described. Now, we have to look for differences in these properties, which can be used to define feature vectors for the classification.

The rain event shown in Figure 4.3a indicates that rain events typically drift across the range gates, and thus the distribution of the echo power between range gates 6, 7 and 8 is variable. Contrary to this, dome instabilities have a fixed ratio of the amplitudes in range gate 7 and 8. Only for very strong events there is an echo visible in range gate 6. Of course, this property does not give any information to discriminate the different types of dome instabilities. Disturbances also have the same fixed amplitude ratio in range gate 7 and 8, because they are somehow related to the static echoes (compare Section 4.3). Thus, the distribution of the echo power across the range gates only helps to discriminate between rain and all other types of events.

A second useful property is the symmetry of disturbances with respect to the velocity $v = 0m/s$. Rain can also have negative velocities, and thus when the rainfall is perpendicular to the radar beam, can have symmetric velocity distributions. Dome instabilities, however, always involve exclusively positive velocities. Thus, the amplitude ratio between negative and positive velocities can be used to distinguish disturbances and dome instabilities, but it can lead to false classifications of disturbances and rain events. Both properties do not help to distinguish between different types of dome instabilities. The amplitude ratio of range gates 7 and 8 and that of negative and positive velocities is the same for all three instability types. The types of instability differ only in the shape of the velocity distribution velocity of range gate 7 and 8.

One way to characterize the shape of a velocity distribution is to use statistical moments. For a random variable X with density function $f(x)$ the statistical moment of order r with respect to value a is defined as

$$m_r(a) = \int_{-\infty}^{\infty} (x - a)^r f(x) dx \quad . \quad (4.37)$$

From this we can derive the definition of the mean and the variance:

$$\mu = m_1(0) = \int_{-\infty}^{\infty} x f(x) dx \quad , \quad (4.38)$$

$$\sigma^2 = m_2(\mu) = \int_{-\infty}^{\infty} (x - \mu)^2 f(x) dx \quad . \quad (4.39)$$

However, these values only give useful information about the location and the broadness of the distribution. Additional information can be gathered using the third and fourth statistical moments, which lead to the definition of the *skewness* and *kurtosis*:

$$Skew = \frac{m_3(\mu)}{\sigma^3} \quad , \quad (4.40)$$

$$Kurt = \frac{m_4(\mu)}{\sigma^4} - 3 \quad . \quad (4.41)$$

The skewness of a distribution gives information about the symmetry of a distribution. The symmetric Gaussian distribution has a skewness $Skew = 0$. When the distribution is tilted towards lower values we have $Skew > 0$ and when it is tilted towards higher values, $Skew < 0$. The kurtosis describes, if the distribution is peaked or rather flat. For peaked distribution we will get $Kurt > 0$ and for flat distributions $Kurt < 0$.

To calculate the statistical moments for the velocity distribution of range gate i , we have to consider the density function $P(i, v)/P(i)$ (see eq. 4.1), i.e. the echo power as function over velocity divided by the total echo power for range gate i . We also convert the integral in (4.37) to a sum, since we only have discrete velocities from v_{min} to v_{max} :

$$m_r^i(a) = \frac{1}{P(i)} \sum_{v=v_{min}}^{v_{max}} P(i, v) (v - a)^r \quad . \quad (4.42)$$

Before we calculate statistical moments, we have to do some preprocessing to reduce unwanted effects. First, we again eliminate the static echoes, since they do not carry any information. Second, the background noise is a problem for the calculation of statistical moments as it is not related to the velocity distribution of moving material. Because it is very stable, it can simply be removed by subtracting a

constant value determined from the training data. Finally, we set all resulting negative values to zero, since negative echo power values do not make sense in a velocity distribution.

Most of these characteristic features have different ranges of values, which leads to some problems. For the KNN classifier model, this is quite intuitive. Suppose our feature vectors contain two features, one in the range $[0, 1]$ and the other in the range $[0, 100]$. When the KNN classifier calculates the distances between training and test samples, the second feature would influence the result much more than the first one and the classification result would only depend on feature two. The same effect can be observed for neural networks. During training the network will adjust weights for the feature 2 input much more than for the feature 1 input. The error will hardly depend on feature 1.

In order to avoid such difficulties, the input patterns can be *standardized* such that for each feature mean and variance are normalized to zero and one, respectively (Duda et al., 2001). To achieve this, we calculate mean and variance for each feature from the training set. Then, the standardized version of a pattern is calculated as follows: (a) we subtract the corresponding calculated mean from each feature of the pattern, and (b) we divide each resulting value by the corresponding variance. Subsequently, the standardized version of the training set has a mean of zero and a variance of one for each feature. Any new pattern, which is presented to the classifier after training, has to be subject to exactly the same transformation before classification. Of course, this transformation only fits arbitrary new data, if the training data provides good coverage of the feature space.

4.8.3 *One-Step Classification*

In our first approach we try to build a classifier, which is capable of discriminating all five categories at once. Considering the observations described above we have designed four different feature extractors, which have been tested with both the neural network and KNN classifier model.

Definition of Feature Vectors

Our first type of feature vector is simply based on the original data. If our classifier model is powerful enough, it will be able to find the important information that discriminates our categories. Thus, the feature vector is just a copy of all relevant parts of the Doppler spectrum, i.e. all spectrum lines of range gate 6, 7 and 8.

	Feature description	Dimensions
$F1$	Preprocessed spectrum of rang gate 6–8	320
$F2$	Summed echo power for positive velocities for range gate 6 and for positive/negative velocities for range gates 7 and 8	5
$F3$	Summed echo power, mean, standard deviation, skewness, and kurtosis of the velocity distribution for each of the range gates 6–8	15
$F4$	Summed echo power, mean, and standard deviation of the velocity distribution for each of the range gates 6–8	9
$F5$	Preprocessed positive half of rang gate 8	64
$F6$	Preprocessed positive half of rang gate 8 including suppression of disturbances	64
$F7$	Mean, standard deviation, skewness, and kurtosis of the velocity distribution of range gate 8	4
$F8$	Mean and standard deviation of the velocity distribution of range gate 8	2

Table 4.2: Definitions of feature vectors.

The resulting feature vector consists of 320 components. To reduce the influence of unimportant information we have to do some preprocessing. First, we eliminate the static echoes, because they carry no information. Especially for neural network classifiers, we have to be cautious with Doppler spectra of very different amplitude. Training a Doppler spectrum with high amplitudes would cause much larger weight updates than spectra with low amplitudes. This leads to a non-uniform learning process. To prevent this effect, we scale the feature vector linearly, such that the maximum feature value is exactly 1.0 and the vector lies within the interval $[0, 1]^{320}$. This type of feature vector will from here on be referred to as $F1$. Feature vector $F2$ consists of only 5 values, each giving the summed echo power for either the positive or the negative velocities of a particular range gate. While for range gate 6 only positive velocities are available, these summed echo power values are included for positive and negative velocities for range gates 7, and 8. Again, we suppress the static echoes and scale the feature vectors to the interval $[0, 1]^5$. This feature vector does not contain any information about the shape of the velocity distributions. For feature vector $F3$ we calculate the summed echo power of each of the range gate 6, 7, and 8, this time without distinguishing positive and negative velocities. Infor-

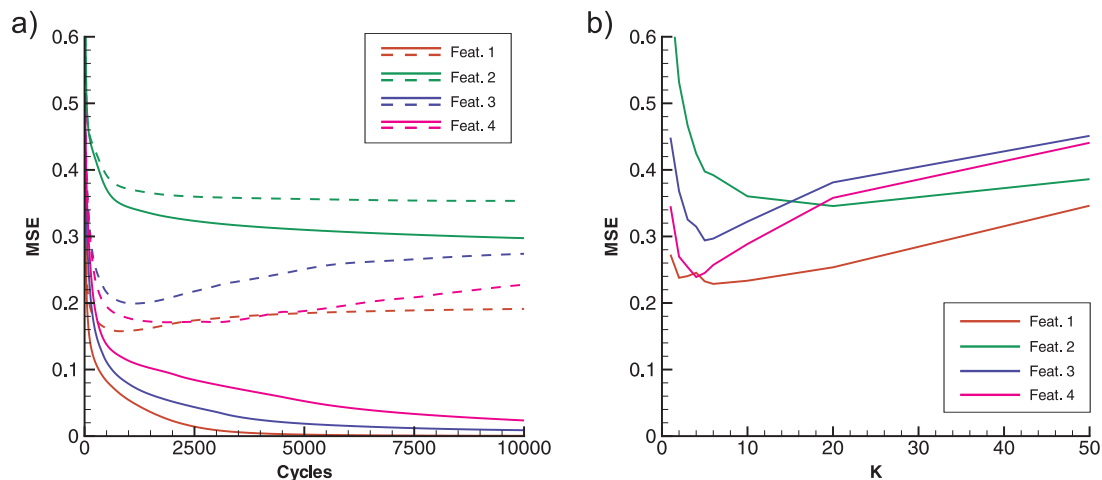


Figure 4.9: Mean squared errors (MSE) of the learning procedure for feature vector types F1–F4 for the "one-step" classification. (a) shows the learning curves for neural network with 25 hidden units, trained with a learning rate of $\eta = 0.01$. Solid lines represent the training set and dashed lines the validation set. (b) shows the MSE of the validation set of KNN classifiers for different values of K .

mation about the location and shape of the velocity distribution of each range gate is represented by the mean, variance, skewness and kurtosis, which are calculated as described in Section 4.8.2. The resulting feature vector still only consists of 15 components. Because the vector contains values from different domains, we now have to standardize all feature vectors (see Section 4.8.2). To analyze the influence of the skewness and kurtosis, feature vector type $F4$ is calculated exactly like $F3$, while omitting the skewness and kurtosis components. Thus, the feature vector $F4$ consists of only 9 components.

Training and Performance Tests

Figure 4.9a shows learning curves of neural networks, i.e. the mean squared error (MSE) as a function of learning cycles for all four types of feature vectors. For each feature vector the same network topology with 25 hidden units has been used. The learning rate η has been set to 0.01. These parameters have been chosen empirically, which will be investigated later in this section. Solid lines represent the MSE for the training set and the dashed lines for the validation set. At the beginning of the training procedure, both training error and validation error are very high, since not much learning has taken place. The training errors decrease monotonically and reach asymptotic values. The errors for the validation sets, however, reach a minimum after a certain number of training cycles and increases afterwards with

further training. This effect is called *loss of generalization* (see e.g. Bishop, 1995 and Duda et al., 2001). Too long training will cause the network to learn a precise representation of the training set. The goal of network training, however, is to build a statistical model of the process which generates the data. A network with good generalization makes good decisions for new inputs, rather than precisely representing the training data. Therefore, the minimum of the validation error can be used to decide, when to stop training.

Both training and validation error show that of all feature vectors the performance of feature vector $F2$ is by far the worst. This is obviously due to the fact that $F2$ does not contain information about the shape of the velocity distributions. Feature vectors $F1$, $F3$ and $F4$ show a much better performance. For $F1$ and $F3$ the validation error reaches its minimum faster than for $F4$, but the lowest errors are reached for $F1$ and $F4$, which differ only slightly. For both $F1$ and $F4$ the loss of generalization is moderate, so that it is relatively easy to define the stop criterion for training.

Figure 4.9b shows the MSE for KNN classifiers with feature vectors $F1$ – $F4$ applied to the validation set. The only parameter for the KNN classifier is the number K of nearest neighbors in the training set, which are taken into account to determine the correct category of samples from the validation set. For our test, K has been varied between 1 and 50. Considering the size of our training sets of 66 samples per category, greater numbers of K would average the posterior probabilities over a large part of the feature space (see above Section 4.6). Like for the neural networks the performance of feature vector $F2$ is significantly worse than for the other feature vectors. For $F1$, $F3$ and $F4$ the minimum of the validation error is reached for values of $K \approx 5$. Again, features $F1$ and $F4$ show the best performance.

While for the KNN classifier we can only vary the parameter K , we now try to adjust the network topology and the learning rate to enhance the classification performance of the neural network classifiers. Because feature vectors $F1$ and $F4$ showed best performance, we focus on these two. Figures 4.10a and b show learning curves for networks with 5, 25 and 100 hidden units. The learning rate has again been set to $\eta = 0.01$. For both feature vectors $F1$ (Fig. 4.10a) and $F4$ (Fig. 4.10b) the network size does not change the classification error significantly. For $F1$ the loss of generalization is larger for the small network with 5 hidden units than for larger networks. But since the large network with 100 hidden units does not enhance the performance, the network with 25 hidden units is the best choice. For $F4$ the differences are even less. Again the network with 25 hidden units shows the smallest loss of generalization, and thus we will further explore the performance for this network size.

Figures 4.10c and d show learning curves for learning rates of 0.001, 0.01 and 0.05.

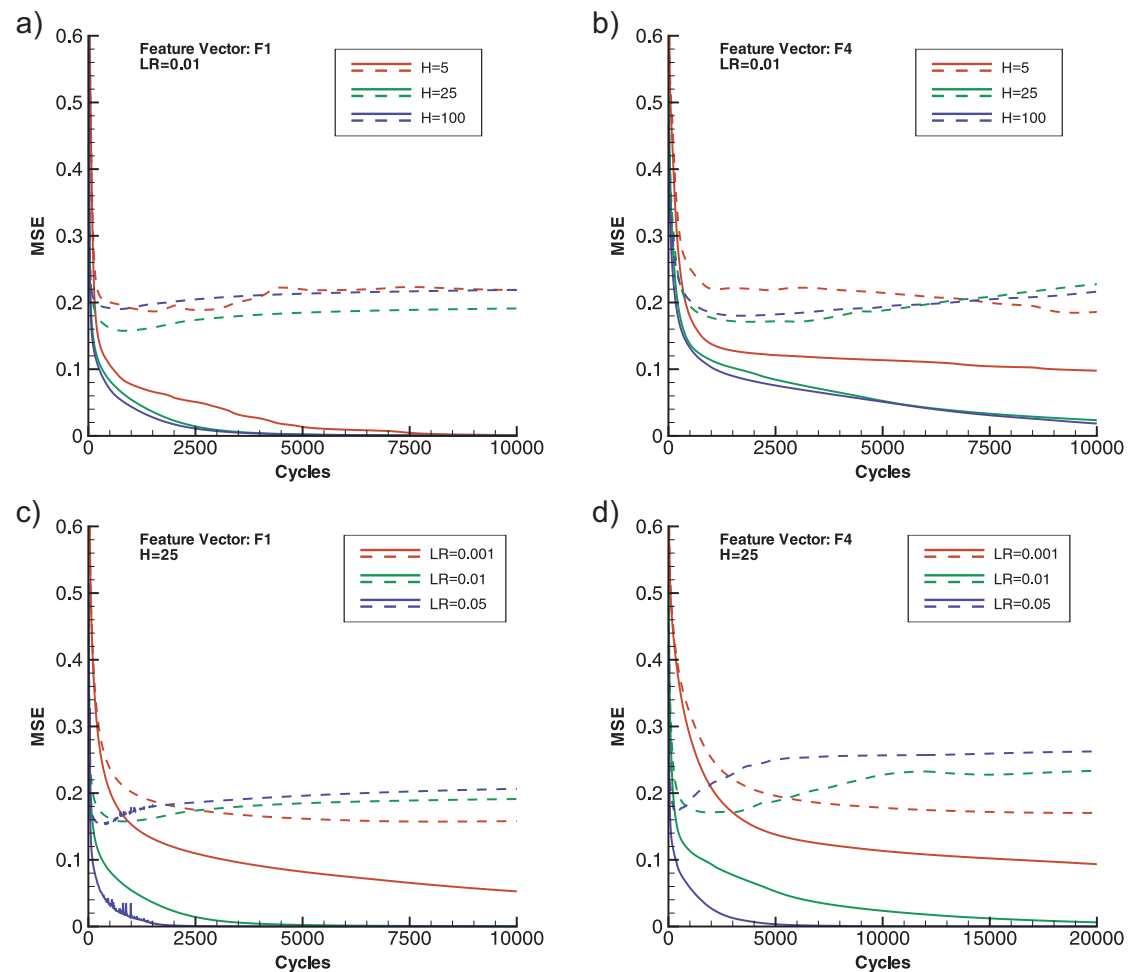


Figure 4.10: Learning curves for neural networks for feature vector type F1 (left column) and F4 (right column) for the "one-step" classification. Plots (a) and (b) show learning curves for 5, 25 and 100 hidden units, trained with a learning rate of 0.01. Plots (c) and (d) show learning curves for learning rates of 0.001, 0.01 and 0.5 for networks with 25 hidden units.

The network size is set to 25 hidden units. For *F1* (Fig. 4.10c) we can see that the minimum of the validation error is reached earlier for higher learning rates. However, even though for a learning rate of $\eta = 0.05$ the minimum is reached quickly, the loss of generalization rises equally fast afterwards. Also the validation error is relatively spiky, which indicates that the learning rate is too high. The minimum of the validation error for a learning rate of $\eta = 0.01$ is reached earlier than for $\eta = 0.001$, but both minima have approx. the same MSE. Because $\eta = 0.001$ has the smallest loss of generalization, this is the best choice. For *F4* (Fig. 4.10d) the minimum of the validation error is again reached earlier for higher values of η . The minima have similar values for all learning rates. However, for $\eta = 0.001$ the loss of generalization is the smallest and, and thus the stop-criterion is easy to define so that we can be

a)

Single-Step Spectrum Classification	$F1$	$F4$
Neural Network	90.61 %	88.79 %
KNN	86.67 %	84.55 %

b) Neural Network
($F1$, $H=25$, $\mu = 0.001$, cycles=3000)

	D	R	S	G	E	U
D	63	1	2	0	0	0
R	7	58	1	0	0	0
S	2	0	61	3	0	0
G	0	0	4	56	6	0
E	0	0	0	5	61	0

c) KNN
($F1$, $K=5$)

	D	R	S	G	E	U
D	61	1	4	0	0	0
R	12	51	2	0	0	1
S	0	0	62	4	0	0
G	0	0	5	56	5	0
E	0	0	0	10	56	0

Table 4.3: (a) Classification results for the "one-step" classification of single Doppler spectra for neural network and KNN classifiers with feature vectors $F1$ and $F4$. (b) Confusion matrix for neural networks using feature vectors $F1$. (c) Confusion matrix for the KNN classifier also using $F1$. (D=disturbance, R=rain, S=sliding, G=gravitational, E=explosive, and U=unknown)

sure to reach the best possible classification performance.

After selecting the classification parameters, we can now use the test set to analyze the actual performance of the different classifiers. Table 4.3a shows the resulting classification rates for all combinations of classifiers and feature vectors $F1$ and $F4$. All classification rates are approx. in the range of 85–90%. For both types of classifiers feature vector $F1$ has a better performance than $F4$, in both cases about 2%. The performance of the neural network classifier is about 4% higher than for the KNN classifier for both feature vectors. Table 4.3b and c show the corresponding so-called confusion matrices for both classifiers and feature vector $F1$. A confusion matrix consists of a row and a column for each category. Rows represent classifications by the expert and columns classifications by the classifier. Each cell of the confusion matrix gives the number of patterns that have been classified by the expert and the classifier corresponding to the row and the column of the matrix. The confusion matrix of a perfect classifier would only consist of entries in the main diagonal, where the classifications of expert and classifier match. All other matrix cells show which kind of misclassification have occurred, e.g. the entry in row "R" and column "I" is the number of rain events which have been classified as instability. Thus, the confusion matrix allows to examine where in particular the classification

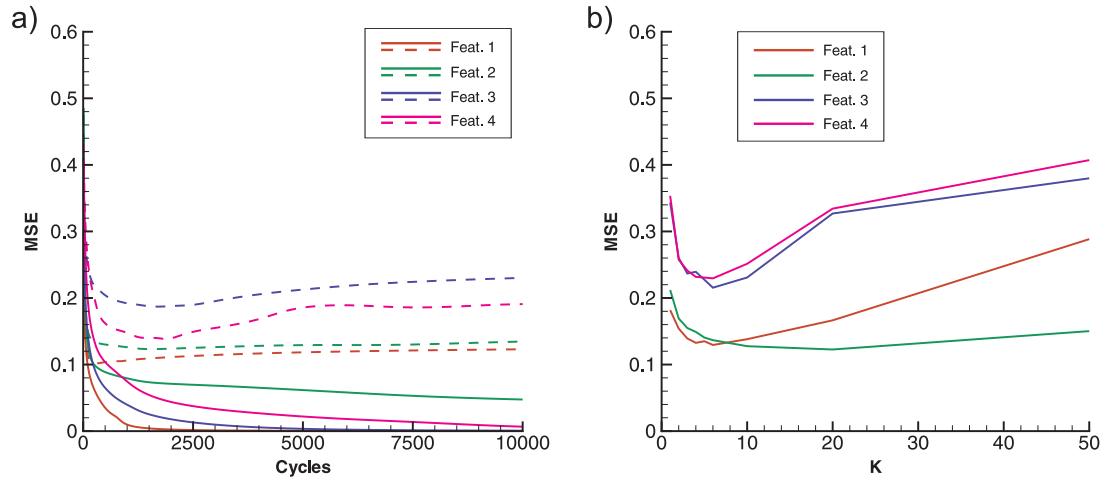


Figure 4.11: Mean squared errors (MSE) of the learning procedure for feature vector types F1–F4 for the first step of the ”two-step” classification. (a) shows the learning curves for neural network with 25 hidden units, trained with a learning rate of 0.01. Solid lines represent the training set and dashed lines the validation set. (b) shows the MSE of the validation set of KNN classifiers for different values of K .

has problems. The confusion matrices for both classifiers show that especially the discrimination between disturbance or rain spectra on one side and all kinds of instability spectra on the other side is very accurate. The discrimination of sliding material, gravitational break-offs and explosive outbursts is a little more accurate for the neural network than for the KNN classifier. For both the discrimination between sliding material and gravitational break-offs is better than between gravitational break-offs and explosive outburst. Sliding material and explosive outburst are well separated, which is due to the fact that their properties are very different.

4.8.4 *Two-Step Classification*

In order to increase the performance we now take into account the hierarchical structure of the categories. The first step in the classification procedure is to discriminate disturbances, rain, and dome instabilities. In the second step, we take all Doppler spectra, which have been classified as dome instability and discriminate between sliding material, gravitational break-offs, and explosive outbursts. The decisions in the first and second step are based on very different properties of the Doppler spectra. While for the first step the distribution of echo power across the range gates is most important, the second step (i.e. the discrimination between the different instabilities) depends mostly on the shape of the velocity distributions.

Definition of Feature Vectors

For the first classification step we tested the same feature vector types as for the "one-step" classifier. For the second classification step, we concentrate on the shape of the velocity distributions. The shape of the velocity distribution is also always the same for ranges 6, 7 and 8. Thus, we can limit our feature extraction to the positive velocity axis of range gate 8, which gives the strongest signal for dome instabilities. Again, to present all necessary information to the classifier, the easiest way is to take the original data. Thus, feature vector $F5$ consists of the 64 spectrum lines of the positive velocity axis of range gate 8 with the obligatory preprocessing: elimination of the static echoes and reduction of the background noise. Sometimes relatively weak disturbances are superimposed on an instability signal. Because we do not want to consider disturbances in this classification step, we try to eliminate them. After the background noise has been subtracted from the spectrum all significant signal components are separated by intervals of zeros. Because disturbances are relatively sharp peaks compared to instability signals, we simply search for signal components with a width smaller than a certain threshold and set all found intervals to zero. Feature vector $F6$ is defined like $F5$ including this additional preprocessing step. Like before both feature vectors are scaled linearly onto the interval $[0, 1]^{64}$. The representation of the velocity distribution by statistical moments is given by feature vectors $F7$ and $F8$. $F7$ consists of the mean, variance, skewness and kurtosis, while $F8$ only consists of the mean and the variance. The amplitude of the signal is not considered. For both $F7$ and $F8$ we do the same preprocessing as described above for $F6$. Additionally, the training sets are standardized (see Section 4.8.2).

Training and Performance Tests

Figure 4.11a shows the learning curves for the neural network classifiers and Figure 4.11b the classification errors of the KNN classifiers for different values of K . The error is generally less than for the "one-step" classifiers, because instead of 5, we have only 3 output values, which contribute to the squared error of one sample. For both the neural network and the KNN classifier, feature vectors $F1$ and $F2$ have smaller validation errors than $F3$ and $F4$. Thus, information on the shape of the velocity distributions as represented by mean and variance appears to disturb the classification process. Especially the good performance of feature vector $F2$ indicates that this information is not necessary for this classification step.

For feature vectors $F1$ and $F2$, Figure 4.12 shows learning curves for different network sizes and learning rates. For $F1$ a network with 5 hidden units seems to be too small, the validation error rises quickly after reaching its minimum (see Fig. 4.12a). The differences between 25 and 100 hidden units are negligible. For $F2$ the

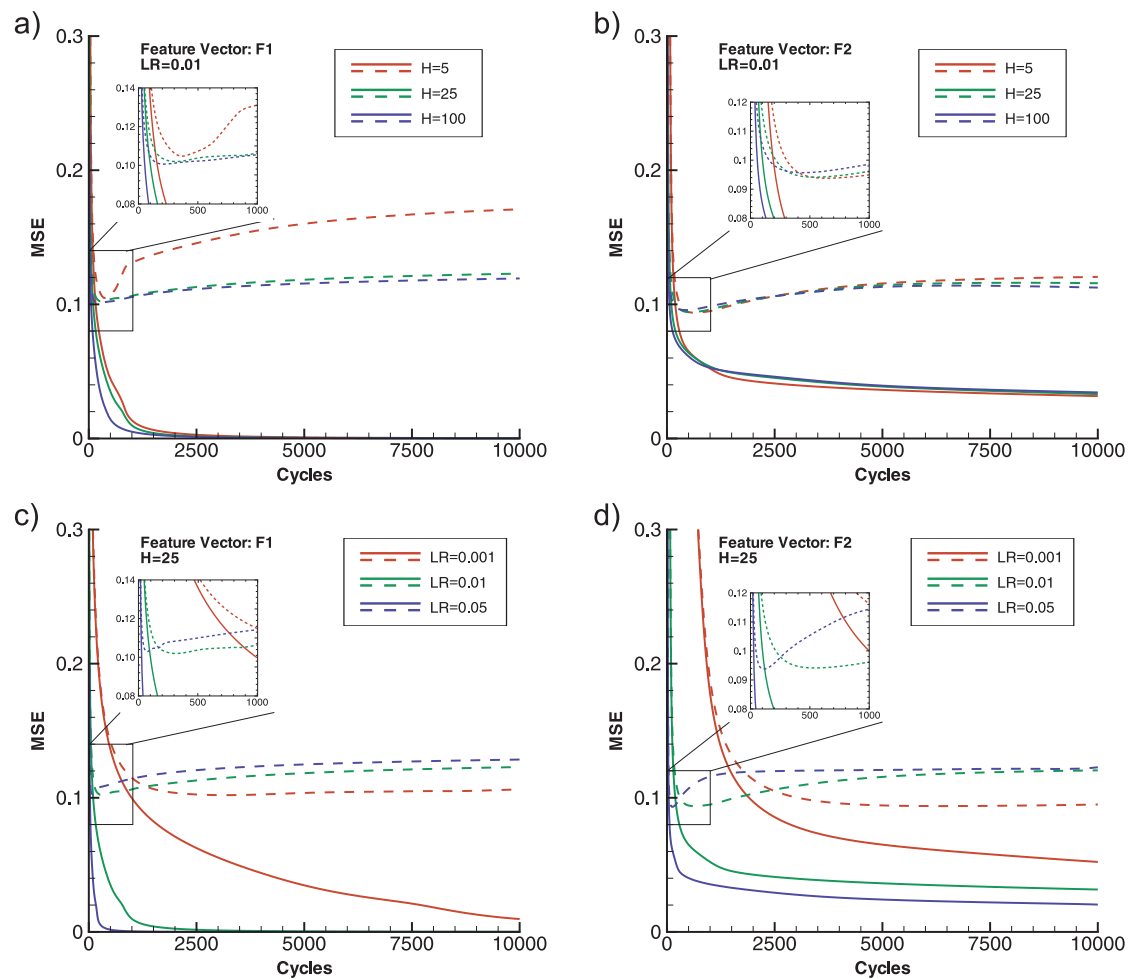


Figure 4.12: Learning curves for neural networks for feature vector type $F1$ (left column) and $F2$ (right column) for the first step of the "two-step" classification. Plots (a) and (b) show learning curves for 5, 25 and 100 hidden units, trained with a learning rate of 0.01. Plots (c) and (d) show learning curves for learning rates of 0.001, 0.01 and 0.05 for networks with 25 hidden units.

network size does not have a significant impact (see Fig. 4.12b). The error for $F2$ is a little less than for $F1$. Figures 4.12c and d show learning curves for a medium network sizes of 25 hidden units. For both $F1$ and $F2$ the validation converges best for a learning rate of $\mu = 0.001$. For $\mu = 0.01$ and $\mu = 0.05$ the errors reach their minimums quickly, but for $\mu = 0.001$ the loss of generalization is less, and thus it is easier to set the stop-criterion for training. Still the validation error of $F2$ is a little less than for $F1$.

Figure 4.13 shows the learning curves for neural networks and the classification errors for KNN classifiers. For neural networks both feature vectors based on statistical

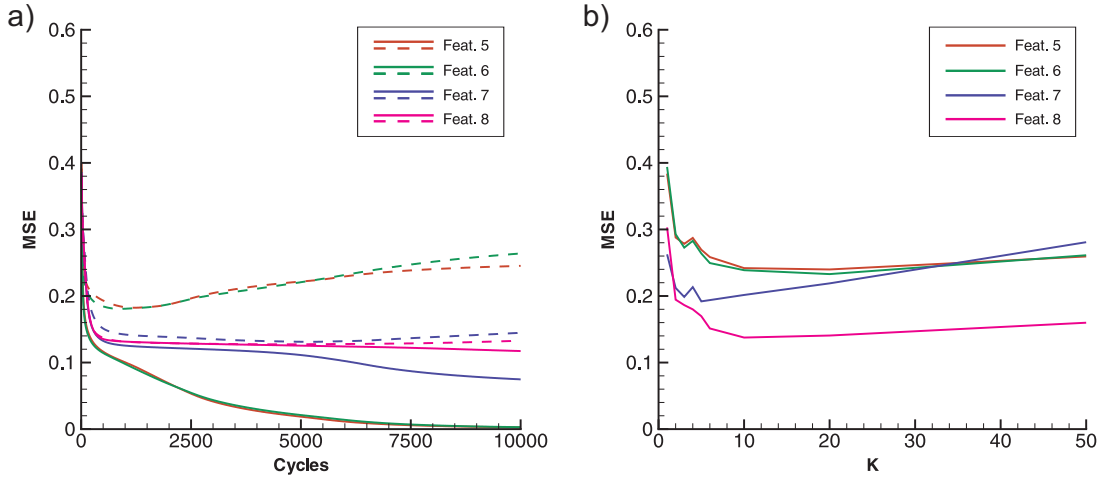


Figure 4.13: Mean squared errors (MSE) of the learning procedure for feature vector types F5–F8 for the second step of the "two-step" classification. (a) shows the learning curves for neural network with 25 hidden units, trained with a learning rate of 0.01. Solid lines represent the training set and dashed lines the validation set. (b) shows the MSE of the validation set of KNN classifiers for different values of K .

moments ($F7$, $F8$) show smaller validation errors than those based on original data ($F5$, $F6$), only their training errors are higher. Thus, with original data reproduction of the training set is very good, but the generalization to new data is bad. Also for the KNN classifiers, the classification error is less for $F7$ and $F8$. Generally, the neural networks have smaller errors than the KNN classifiers, only for $F8$ the errors are approximately the same. For $F8$ the best value of K is about 10.

Figure 4.14 shows the learning curves for different network sizes and learning rates for $F7$ and $F8$. For $F7$, the large network with 100 hidden units has the smallest validation error, with its minimum at about 2500 learning cycles (see Fig. 4.14a). Figure 4.14c shows that for this network a small learning rate of 0.001 converges too slowly and for a higher learning rate of 0.05 the loss of generalization is very high even after a few learning cycles. For $F8$ (see Fig. 4.14b) the learning curves are almost the same for 5, 25 and 100 hidden units, so there is no need for a big network and we chose the medium network size with 25 hidden units. The best learning rate is again $\mu = 0.01$. It has only a slightly higher minimum of the validation error, but the loss of generalization is very moderate. For some of the network configurations in Figure 4.14 the validation error lies below the training error. The high training error can be due to a weak expressiveness of the feature vector. However, in this case we would expect the validation error to be even higher. In our case, it is most probably due to the fact that the categories of instabilities are not defined precisely. The transitions between sliding material and gravitational

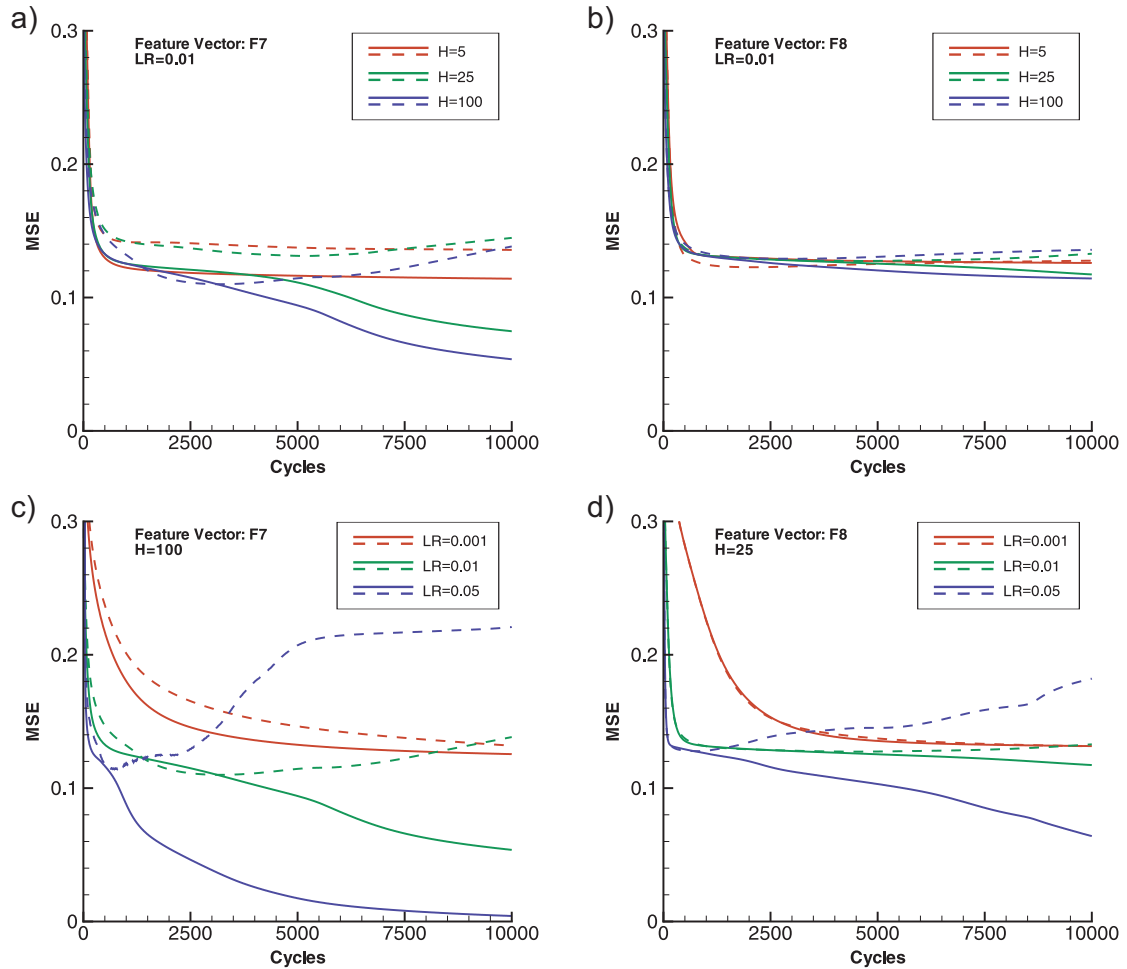


Figure 4.14: Learning curves for neural networks for feature vector type F7 (left column) and F8 (right column) for the second step of the "two-step" classification. Plots (a) and (b) show learning curves for 5, 25 and 100 hidden units, trained with a learning rate of 0.01. Plots (c) and (d) show learning curves for learning rates of 0.001, 0.01 and 0.5 for networks with 25 hidden units.

break-off as well as between gravitational break-offs and explosive outbursts are fuzzy and when an expert classifies the samples of the training set, he might label two sample differently, although they differ only slightly. This will cause the training error to be relatively high, because the network cannot map both samples exactly to the correct outputs. For the validation set, however, the influence is smaller, because the error is always higher for samples near the decision boundary.

To analyze the performance we again applied the different classifiers to the corresponding test sets. Table 4.4a shows the resulting classification rates for both classification steps. In the first classification step feature vector $F2$ achieves a clas-

a)

two-step Spectrum Classification	Step 1		Step 2		Combined $F2+F8$
	$F1$	$F2$	$F7$	$F8$	
Neural Network	90.91 %	93.94 %	90.91 %	90.91 %	90.61
KNN	89.39 %	91.92 %	87.88 %	88.89 %	88.18

b) NN – Step 1
($F2$, $H=25$, $\mu = 0.001$, cycles=6000)

	D	R	I	U
D	62	2	2	0
R	6	58	2	0
I	0	0	66	0

c) KNN – Step 1
($F2$, $K=20$)

	D	R	I	U
D	63	1	2	0
R	9	53	3	1
I	0	0	66	0

d) NN – Step 2
($F8$, $H=25$, $\mu = 0.01$, cycles=4000)

	S	G	E	U
S	56	3	0	0
G	6	53	7	0
E	0	8	58	0

e) KNN – Step 2
($F8$, $K=10$)

	S	G	E	U
S	65	1	0	0
G	5	51	10	0
E	0	2	64	0

f) NN – Combined $F2+F8$

	D	R	S	G	E	U
D	62	2	2	0	0	0
R	6	58	1	1	0	0
S	1	0	64	1	0	0
G	0	0	5	51	10	0
E	0	0	0	2	64	0

g) KNN – Combined $F2+F8$

	D	R	S	G	E	U
D	63	1	2	0	0	0
R	9	53	2	1	0	1
S	1	0	63	2	0	0
G	0	0	3	50	10	3
E	0	0	0	1	62	3

Table 4.4: (a) Classification rates for neural network and KNN classifiers for the "two-step" classification for single spectra. (b)–(c) Confusion matrices for step 1 using feature vector $F2$. (d)–(e) Confusion matrices for the step 2 using feature vector $F8$. (f)–(g) Confusion matrices for the complete classification procedure using feature vectors $F2$ (step 1) and $F8$ (step 2). (D=disturbance, R=rain, I=instabilities, S=sliding, G=gravitational, E=explosive and U=unknown)

sification rate that is about 1–2% higher than for $F1$, with 93.94% for the neural network and 91.92% for the KNN classifier. Presumably, the large feature vector $F1$ includes too much unimportant information, which in some cases confuses the classifier. For both feature vectors the neural network achieves classification rates that are about 1–2% higher than for the KNN classifier. For the second classification step the results are similar, although the differences between feature vectors $F7$ and $F8$ are even smaller. Thus, including the skewness and kurtosis of the velocity distribution does not enhance the classification performance. Again, with 90.91% the neural networks achieve a classification rates that is about 2–3% higher than for the KNN classifiers. The confusion matrices in Table 4.4b and c show that for step one we again have a very good discrimination between rain and disturbances on the one hand and instabilities on the other hand. The confusion matrices for step two (Table 4.4d and e) also show that we again have a very good discrimination between sliding material and explosive outbursts. However, for the discrimination between sliding material and gravitational break-offs and between gravitational break-offs and explosive outbursts we still get a significant number of misclassifications.

In order to compare the "one-step" and the "two-step" classification procedures, we tested the complete "two-step" classification procedure with the same test set that has been used to test the "one-step" classifiers. Here, we choose feature vectors $F2$ for step one and $F8$ for step two. A comparison with Table 4.3 shows that the performance is almost the same as for the "one-step" classification, especially for neural networks. Also, the confusion matrices in Table 4.4e and f show that we still have a very good discrimination between non-instability and instability spectra. However, the discrimination between the different types of instabilities could not be enhanced.

4.9 Event Classification

So far we have designed procedures to classify single Doppler spectra. The goal, however, is to classify complete radar events, which contain a sequence of several Doppler spectra. In order to determine the category of an event, we first classify each Doppler spectrum of the event separately as described in the previous sections. For each spectrum the result is a class vector consisting of five probabilities, one for each spectrum class (see Sections 4.5–4.7). In the following we describe, how the class of the complete event can be determined by analyzing the sequence of class vectors.

First, we discriminate events of disturbances, rain and instabilities. Therefore, we sum up all class vectors of the sequence and divide it by the length of the sequence, which results in an average class vector. Thus, this class vector represents the aver-

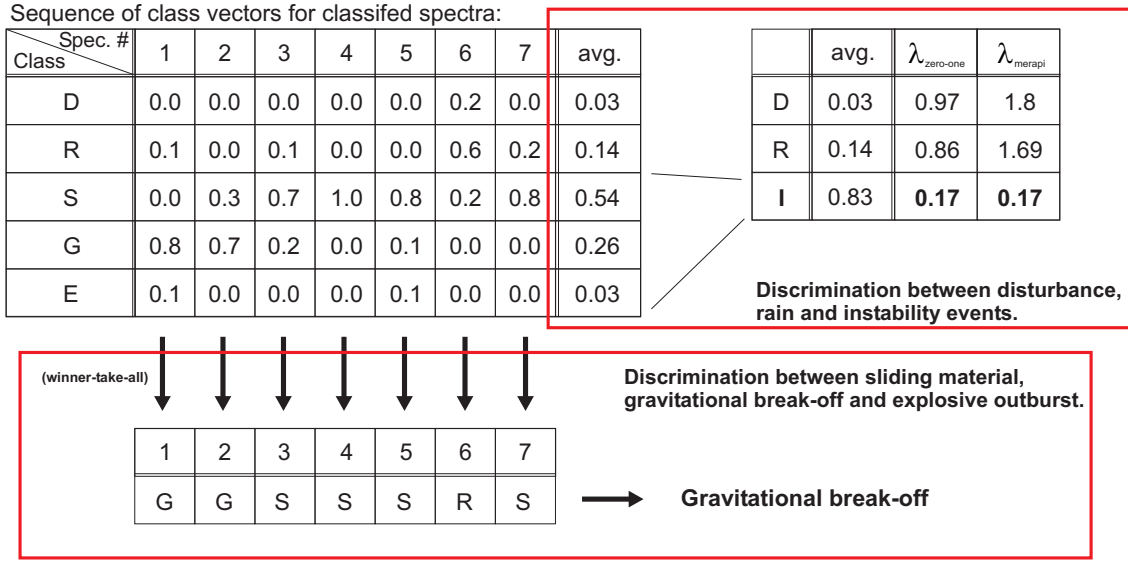


Figure 4.15: Classification of a radar event given a sequence of already classified single Doppler spectra represented by their class vector (upper left table). First, we determine from the average class vector if the event is an disturbance, rain or instability event (upper right table). In case the event is a instability, the class vectors of all spectra are evaluated by the "winner-take-all" rule, and from the resulting sequence of spectrum class labels the type of instability event is determined (lower table).

age classification of single Doppler spectra for the complete event. From this average class vector we determine the class of the event according to the Bayesian decision rule (see Section 4.5). In order to apply the Bayesian decision rule we need a loss function. The easiest choice is the zero-one loss function $\lambda_{\text{zero-one}}(\alpha_i, \omega_j)$ (see eq. (4.11)). However, the confusion matrices in Table 4.3 and 4.4 show that an instability spectrum is more likely to be classified as rain spectrum than vice versa. This is due to the fact that rain events often drift across the range gates. Therefore, it happens that for some of the Doppler spectra of a rain event the echo power is similarly distributed across the range gates as it is typical for instability spectra. Besides that, it is especially undesirable to classify rain as instability. Because the echo power for rain events is often very high (see Section 4.3) such misclassifications have a strong impact on the analysis of the number and size of instability events (see companion paper Voegelé et al., 2006). The same holds for disturbances and instabilities. Therefore, we define another loss function $\lambda_{\text{merapi}}(\alpha_i, \omega_j)$, which associates higher loss for disturbances and rain events being wrongly classified as instability:

$$\lambda_{\text{merapi}}(\alpha_i, \omega_j) = \begin{cases} 0 & : i = j \\ 1 & : i \neq j \text{ and } j \neq 2 \\ 2 & : i \neq j \text{ and } j = 2 \end{cases} \quad i, j = 1, \dots, c \quad (4.43)$$

where α_0 and ω_0 correspond to disturbances, α_1 and ω_1 to rain and α_2 and ω_2 to

instabilities. Regardless of which loss function we use, we can now apply equation (4.9) to calculate the conditional risks for each event class and the class with the smallest risk is considered to be the true class. For an illustration of the procedure to discriminate disturbance, rain and instability events see Figure 4.15.

In case an event is classified as instability, we still have to determine the type of instability. Usually, explosive instability events contain all three types of spectra. After the actual outburst, the loosened material is tumbling or sliding down the slope and will cause spectra of the classes sliding material or gravitational break-off. Gravitational events consist of a gravitational break-off, which is also followed by sliding material. Only events whose Doppler spectra are all classified as sliding material, are considered as sliding material events. Therefore, we take the sequence of class vectors, but now we evaluate the spectrum class of each single spectrum using the *winner-take-all* rule (see Fig. 4.15), i.e. the Bayes decision rule with zero-one loss function (see Section 4.5). The result is a sequence of class labels, which can now be analyzed according to the following rules:

1. If one spectrum is labeled as an explosive outburst, the event is labeled as explosive outburst,
2. else, if at least one spectrum is classified as a gravitational break-off, the event is labeled as gravitational break-off,
3. else, the event is label as sliding material

Because the event has been classified as instability beforehand (see above) no or only very few Doppler spectra in the sequence might be classified as disturbance or rain, which therefore can simply be ignored.

We tested the event classification with a test dataset of 450 events, 90 of each event category. We combined both loss functions described with several Doppler spectrum classifiers. The resulting classification rates are shown in Table 4.5a. Generally, the loss function $\lambda_{\text{merapi}}(\alpha_i, \omega_j)$ performs slightly better than $\lambda_{\text{zero-one}}(\alpha_i, \omega_j)$ with about 1–2%. The "two-step" neural network spectrum classifier using feature vectors $F2$ and $F8$ achieved the best classification rate with 88.22% ($\lambda_{\text{zero-one}}$) and 89.59% (λ_{merapi}), respectively. The confusion matrices in Table 4.5b and c show that for $\lambda_{\text{zero-one}}(\alpha_i, \omega_j)$ significantly more non-instability events have been classified as instability than vice versa. As expected, $\lambda_{\text{merapi}}(\alpha_i, \omega_j)$ results in a larger number of misclassifications of instability events, which are labeled as disturbance or rain. Since the choice of the loss function only influences the discrimination between disturbance, rain and instability events, the classification errors within the different types of instability are almost equal. They only differ, where an instability has been classified as disturbance or rain event or vice versa.

a)

	$\lambda_{\text{zero-one}}(\alpha_i, \omega_j)$	$\lambda_{\text{merapi}}(\alpha_i, \omega_j)$
one-step-NN (<i>F1</i>)	81.78 %	84.00 %
one-step-NN (<i>F4</i>)	85.56 %	87.56 %
one-step-KNN (<i>F1</i>)	72.67 %	74.22 %
one-step-KNN (<i>F4</i>)	81.11 %	82.44 %
two-step-NN (<i>F1+F8</i>)	83.11 %	84.59 %
two-step-NN (<i>F2+F8</i>)	88.22 %	89.56 %
two-step-KNN (<i>F1+F8</i>)	82.44 %	84.00 %
two-step-KNN (<i>F2+F8</i>)	86.89 %	88.89 %

b)

two-step-NN (*F2+F8*) / $\lambda_{\text{zero-one}}$

	D	R	S	G	E	U
D	78	1	7	1	0	3
R	6	81	2	0	0	1
S	0	1	83	6	0	0
G	0	0	13	68	9	0
E	0	0	1	2	87	0

c)

two-step-NN (*F2+F8*) / λ_{merapi}

	D	R	S	G	E	U
D	87	1	2	0	0	0
R	7	82	1	0	0	0
S	0	1	83	6	0	0
G	4	0	13	65	8	0
E	1	0	1	2	86	0

Table 4.5: (a) Classification rates for the discrimination of disturbance, rain and instability events for all combinations of spectrum classifiers and loss functions. (b) Confusion matrix for "one-step" neural network spectrum classifier and the $\lambda_{\text{zero-one}}(\alpha_i, \omega_j)$ loss function. (c) Confusion matrix for "two-step" neural network spectrum classifier and the $\lambda_{\text{merapi}}(\alpha_i, \omega_j)$ loss function.

The "two-step" Doppler spectrum classifiers achieved significantly better classification rates than the corresponding "one-step" classifiers, although the performance has been equally good during the tests with single Doppler spectra. Generally, we again observe that neural network classifiers have better performance than the corresponding KNN classifier.

4.10 Conclusion and Outlook

The Doppler radar technique provides a unique opportunity to observe dynamic processes at active lava domes. Three different kinds of dome instability have been identified using Doppler radar observations. Because a spectrum is recorded every 3 seconds a manual analysis of radar events is time consuming. During periods

of high activity several hundred instability events can occur each day. Therefore, an automatic classification system is mandatory in order to continuously monitor different types of dome instability events. Such a system was described in this paper.

One main difficulty for the classification of radar events is the choice of characteristic features, which are fed into the classifier. Radar events consist of a sequence of Doppler spectra of variable length. Because the physical process driving an instability can change during an event, it was found to be difficult to define feature vectors with fixed length, which are able to characterize complete radar events. Therefore, we first classify single Doppler spectra and then classify the event by analyzing the sequence of classified Doppler spectra. Two different strategies have been followed to classify Doppler spectra of the categories disturbance, rain, sliding material, gravitational break-off and explosive outburst: a) discriminating all five categories at once and b) first discriminate disturbance, rain and instability spectra and then discriminate the different types of instability spectra. All classification procedures and feature vectors have been implemented using either a neural network or a KNN classifier.

The performance of the classification of the different types of spectra mainly depends on the type of feature vector. For the discrimination between disturbances, rain and instability spectra we achieve a classification accuracy of about 94%. However, subdividing the classification task into two steps does not enhance the classification performance for single Doppler spectra, neither for the discrimination between disturbances, rain and instabilities, nor for the different types of instabilities. The overall classification rate for both the "one-step" and the "two-step" classification approach is about 90%.

Both classifier models provided good performance, the neural network classifier has only a slightly better performance than the KNN classifier. The neural network has also the advantage that it is much less consuming in computation time than the KNN classifier. The neural network is trained before it is applied to new data. When new data is presented to the network, the calculation of the outputs is very fast, because the network size is relatively small. The KNN classifier does not need to be trained before classifying new data. Instead, it calculates the euclidean distance between the new pattern and each pattern in the training set. Depending on the size of the training set and the size of the feature vector, this can be very time consuming. However, for the KNN classifier only parameter K has to be chosen, and the fact that no time consuming training has to be done, the KNN classifier is especially suitable for testing a large number of feature vectors for their expressive power.

The classification of events has also been tested with two different approaches. The discrimination between the disturbance, rain and instability events showed signifi-

cantly better performance for the special $\lambda_{\text{merapi}}(\alpha_i, \omega_j)$ loss function, than for the standard $\lambda_{\text{zero-one}}(\alpha_i, \omega_j)$ loss function. Table 4.5c shows that only about 1.1% of non-instability events have been classified as instability and with 2.2% only slightly more instabilities have been classified as non-instability.

The discrimination between the different types of instability events has a higher rate of misclassifications. Only 86.6% of the instability events have been correctly classified. However, even for the expert, who assembles the training sets it is not always easy to decide, e.g. whether an instability event contains an explosive outburst or if it is merely a bigger gravitational break-off. This is due to the fact that the characteristics of sliding material, gravitational break-offs and explosive outbursts are continuous, and thus the boundary between the different types of instabilities is somewhat fuzzy. Disturbances, rain and instabilities can be discriminated much easier by the expert. In some cases a rain spectrum might look like an instability spectrum, but this is rare and usually does not persist for a complete event. In some cases the events of different types overlap or superimpose, meaning they occur at the same time. Of course, in this case a clear classification is not possible.

Based on the sequence of classified Doppler spectra we can further discriminate different types of explosive events. Some events start with an explosive outburst, others start with a gravitational break-off or sliding material followed by an explosion. In addition, we can distinguish between explosive events with single or multiple outbursts. To define decision rules we count the explosive instances, i.e. intervals of explosive spectra interrupted by non-explosive activity. If there is more than one explosive instance, the event is considered as multiple explosive outbursts. Besides that, we can determine the time offset between the beginning of the event and the first explosive spectrum. If this offset is less than 6 seconds, i.e. only one other spectrum occurred before the outburst, we consider the explosive outburst as initial.

The classification system developed in this paper has been applied to a huge data set of radar events, which has been acquired at Merapi volcano between November 2001 and July 2004 and contains about 80.000 events. In part II of this paper (Voegelé et al., 2006) the classified radar events have been used to analyze the dome activity during this period of time.

Acknowledgments

We are grateful to the head of the Merapi Volcano Observatory, Antonius Ratdompurbo, and to the staff of the MVO (especially Agus Sampurno and Anton Sulis-

tio) for their cooperation and continuous support of this project. We also thank the Stuttgart Neural Network Simulator Group for providing their neural network software package "SNNS". This work was funded by the Deutsche Forschungsgemeinschaft through grants Ho 1411 14-1,2 and 15-1.

Chapter 5

Automatic Classification of Dome Instabilities based on Doppler Radar Measurements at Merapi Volcano, Indonesia: Part II

by Malte Vöge, Matthias Hort, Ralf Seyfried and Antonius Ratdomopurbo

Submitted to Geophysical Journal International, 11/2006

Abstract

In this paper we analyze a 3 year long time series of activity at Merapi volcano, Indonesia, which was recorded using a Doppler radar system. Between November 2001 and July 2004 about 57000 events associated with dome instabilities have been recorded by the radar system. Because of the huge amount of data an automatic classification system has been developed, which identifies different types of instabilities at the lava dome (i.e. sliding material, gravitational break-offs and explosive outbursts) as well as rainfall. Comparing the record of detected instabilities to rockfall measurements deduced from the seismic network of the Merapi Volcano Observatory, we are able to demonstrate the high potential of Doppler radar measurements for monitoring of dome activity. When aligned to the most active area at the dome, the radar detects significantly more events than the seismic system. In combination with seismic measurements, the Doppler radar allows for identifying changes in the location of the most active area at the dome. This is particularly helpful since the dome of Merapi is covered by clouds about 50% of the time. Additionally, the radar data can help to distinguish between rockfalls and multiphase events in the seismic

measurements.

The different types of instabilities have been analyzed for their occurrence frequency in terms of size, volume and mean velocity. Significant temporal changes in the relative occurrence frequencies or the characteristic properties of the different types of instabilities have not been observed. However, during the period of fastest activity decrease, explosive instability events with a gravitational precursor decreased faster than events starting explosively. Because the radar system is able to observe rainfall, the data has been analyzed for a link between rain and dome activity. Throughout the observation period no such link could be found, however, this might be due to the fact that the activity has been almost continuously decreasing.

5.1 Introduction

Merapi volcano, located in Central Java, Indonesia, is one of the most active dome building volcanoes worldwide, with about 70 major eruptions since 1548 (Simkin and Siebert, 1994). Since 1972 Merapi is continuously active with periods of increased activity in 1984, 1994, 1997, 1998, 2001 and 2006. The activity is dominated by expulsion of viscous and highly crystalline basaltic andesitic lavas, which form dome structures. Partial or total collapses of these structures lead to highly destructive pyroclastic flows, so-called nuée ardente or block and ash flows, which can have run-out distances of several kilometers. Due to the high population density in the vicinity of Merapi volcano, it is considered one of the most dangerous volcanoes of this kind. A major dome collapse caused about 60 fatalities in 1994 (Voight et al., 2000) and during the activity in 2006 three people lost their lives although extensive evacuation was in place. In order to reduce the hazard associated with eruptions of Merapi volcano, it has been monitored for many years.

In the past, dome activity has mainly been observed by seismic measurements. Two types of seismic signals are believed to be directly linked to dome growth: multiphase signals (MP) and signals caused by rockfalls and block and ash flows. Multiphase events are associated with magma transport just beneath the dome (Ratdomopurbo and Poupinet, 2000) leading to an increase in dome volume. Rockfalls and block and ash flows are associated with instabilities at the dome and lead to a decrease in dome volume. Figure 5.1 shows the record of the daily number of rockfalls, which have been detected by the seismic network of the Merapi Volcano Observatory (MVO) between February 2000 and July 2003. In July 2000, the number of multiphase events started to increase and a new period of dome growth began. The number of rockfalls did not follow this trend immediately, which indicates that early on the growing dome was relatively stable. In late December the multiphase events rose more quickly and starting at January 10, 2001, the number of rockfalls also increased dramatically, indicating that the dome was beginning to become

unstable. The peak of the activity is marked by a partial dome collapse, which occurred in two stages on January 28 and February 10 (e.g. Friedel et al., 2004). This record demonstrates the important role of these monitoring parameters for hazard mitigation. While multiphase events give early information about emerging dome activity, in this case several month in advance, the number of rockfalls give important information about the stability of the growing dome and how probable a collapse is in the immediate future.

The goal of our Doppler radar measurements at active lava domes is to enhance the observation of dome instabilities and the resulting rockfalls and block and ash flows. Doppler radar measurements can overcome some drawbacks of visual and seismic monitoring of rockfalls. Visual observations of rockfall activity usually give only qualitative but no quantitative information about the number and size of rockfalls. Furthermore, visual observations require continuously good visibility conditions, which is scarce because the summit of Merapi is often covered by clouds. Seismic measurements are mainly intended to observe changes inside the volcanic edifice. During high volcanic activity various types of events are observed in the seismic data, e.g. long-period events, short period events, multiphase events, etc. (Ratdomopurbo and Poupinet, 2000). Thus, seismic events induced by rockfalls can be superimposed by events that originate inside the volcano. The higher the activity, the more probable it is that seismic events overlap. Especially rockfall events are likely to overlap, because they usually have a relatively long duration of several minutes. The radar system, however, focuses exclusively on the dome, and thus only the first few seconds of a rockfall event are observed. This results in a better discrimination of succeeding rockfall events (Voegelé and Hort, 2007). The drawback of focusing solely on one spot of the volcano can be overcome by installing more radar systems, which together cover a larger area.

Because the radar mainly observes the onset of a rockfall event, we use the term "instability event" to describe an event of increased echo power in the radar data, which is associated with a rockfall. So far, three types of dome instability events have been identified using radar measurements: sliding material, gravitational break-offs and explosive outbursts (see Hort et al., 2006; Voegelé and Hort, 2007). In order to monitor these different types of instabilities, an automatic classification system has been developed, which is described in the companion paper (Voegelé and Hort, 2006). In this paper we analyze a 3 year record of Doppler radar monitoring at Merapi volcano starting in October/November 2001. The most active period has been observed between November 2001 and January 2003. In 2004 and 2005 the activity was very low and also the data quality from 2005 is relatively bad due to technical problems. The recent activity in 2006 has only partially been monitored by the systems. Unfortunately, the activity was directed towards the southeast, while the radar systems have been installed in the west and southwest of the volcano, and thus most of the activity could not be observed. For the investigations presented in this paper we therefore focus on the period between November 2001 to July 2004.

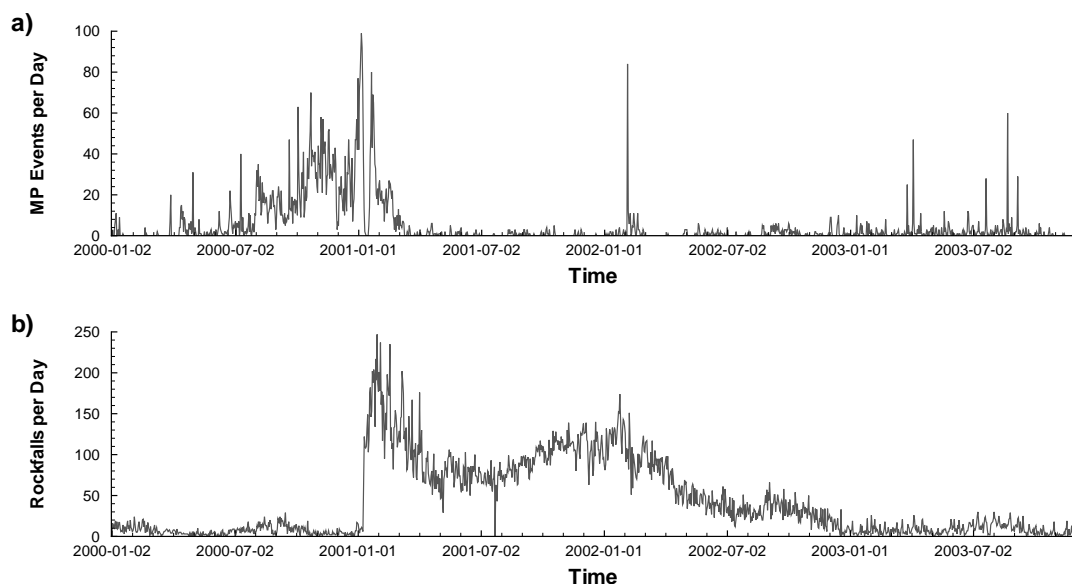


Figure 5.1: (a) Daily number of seismic multiphase events from January 2001 to November 2003. (b) Daily number of rockfall events for the same period.

Two radar stations have been installed at Merapi volcano at Pos Babadan and Pos Gemer, respectively (see small map in Fig. 5.2). Since the station at Pos Gemer has not been installed before January 2005 we will only show data from the radar system at Pos Babadan.

After a short introduction to the radar system in Section 5.2, we will compare rockfall monitoring results from seismic and radar measurements (Section 5.3) and investigate the record for temporal changes in the type of activity, e.g. the number and size of different types of instabilities and mean event velocity. Because the radar system is also able to observe rainfall at the dome, we also look for correlations between rainfall and dome activity. All observations will be thoroughly discussed in Section 5.4.

5.2 System - Setup

The first radar station was setup in late October 2001 at Pos Babadan, an observation post on the western flank of the volcano at an altitude of 1280m above sea level. The distance from the active dome is about 4.5km (see Fig. 5.2). The station is equipped with a frequency modulated continuous wave (FMCW) Doppler radar with a base frequency of 24GHz. The radar system is intended to detect material



Figure 5.2: Setup of the radar station at Pos Babadan on the wester flank of Merapi. The map in the upper left corner shows the locations of stations Babadan and Gemer as well as the deposits of recent dome collapse events. Deposit mappings are taken from Schwarzkopf and Schmincke (2000). (Digital elevation model provided by C. Gertenecker, TU Darmstadt)

movements in the dome area and to provide information about distance and velocity of moving targets. The distance resolution is rather coarse, and a maximum of 16 distance intervals of equal length, so-called range gates, can be resolved. The velocity resolution is 0.285m/s ranging from -18.24m/s to $+18.24\text{m/s}$ in each distance interval. We note that the measured velocities are radial velocities, i.e. the velocity component in direction of the radar beam. Targets approaching the radar have positive radial velocities, whereas targets moving away from the radar have negative radial velocities. In order to measure the complete velocity vector of a mass movement, at least three radar systems are necessary (Voegel et al., 2005). The echo power received by the radar is a function of the total volume of the reflecting material and the particle size distribution. Because the volcanic material moving during an instability event does not fill the complete radar beam, the echo power also depends on the location of the material movement relative to the center of the beam. Thus, under the assumption that the particle size distribution does not vary significantly between different events, and that we observe the precise position of the most active spot at the dome, we can assume that the echo power roughly scales with the size of an instability event.

When aligned to the dome, the radar beam has an elevation angle of about 21° (Fig. 5.2). The opening angle of the radar beam is about 1.5° . We estimate the slope at the dome to be about $45 - 60^\circ$, and thus the area covered by the radar beam at

the dome is an elliptical area of approximately $125m$ width and $250 - 300m$ height. The range gate length is set to $600m$ and data from the range gates $1800 - 2400m$, $3000 - 3600m$, $3600 - 4200m$ and $4200 - 4800m$ are stored. For a detailed description of the system see (Voege and Hort, 2007).

5.3 Observation of Dome Activity between November 2001 and July 2004

During the observation period between November 2001 and July 2004 about 80000 radar events have been registered. A radar event is considered, when the echo power in the Doppler spectra increases significantly compared to the background noise. Such events can be due to rainfall, a dome instability, or it can be a disturbance (see Voege and Hort, 2006). Of course, we are particularly interested in events associated with dome instabilities. In total about 57000 instability events have been identified by the classification system described in Voege and Hort (2006).

In order to demonstrate the performance of Doppler radar measurements to observe dome activity, we compare instabilities detected by radar to rockfalls detected by the seismic network of the MVO. Because the rockfall measurements of the MVO have only been available as number of rockfalls per day, we generated the corresponding record for instabilities detected by the radar. We note that the analysis of the seismic data is currently done by an automated processing system. The seismograms used in this study, however, have been analyzed manually. Figure 5.3 shows the daily number of rockfalls/instabilities identified from the the seismic measurements (green) and by detected the Doppler radar (red) from December 2000 to July 2004. Unfortunately, the activity from January to October 2001 has not been observed by the radar system because it was installed in late October 2001. In February/March 2002 there is no radar data available for a period of about 3-4 weeks. This is due to a system damage by lightning. After the system has been repaired, the radar beam had to be realigned to the active spot at dome. From then on, there are no additional significant data gaps until November 2003.

From October 2001 to March 2002 the number of rockfalls deduced from the seismic data increases slightly from about 105 to 120 events per day. Following March 2002 the number of rockfalls continuously decreases. Only slight increases are visible in September 2002 and August 2003. Clearly, the instability events in the radar data roughly follow the overall trend of the seismic rockfall events. However, during times of high activity the number of instabilities observed by the radar system is much higher than in the seismic data. As the activity decreases, the number of instabilities in the radar data approaches the number of rockfalls detected by the

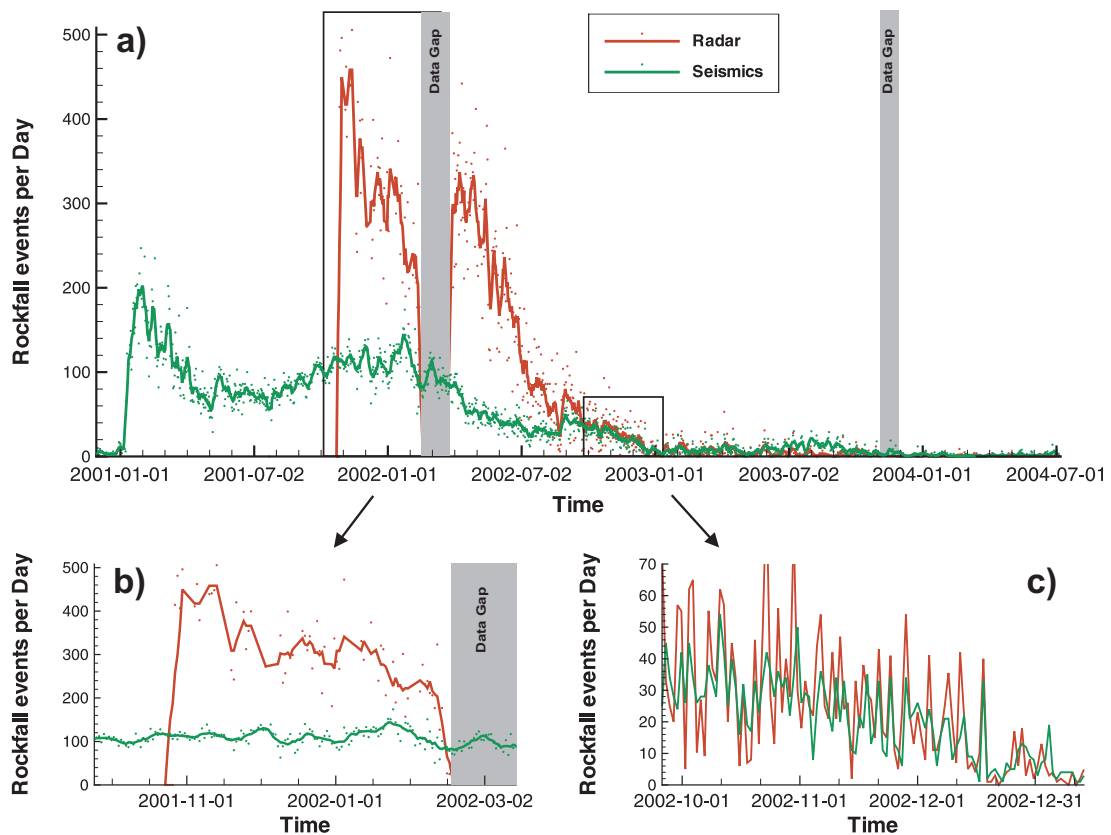


Figure 5.3: (a) Daily number for rockfall events detected by the radar system (red) and the seismic network (green) between December 2000 and July 2004. Note that the radar measurements started in late October 2001. Dots show the actual number of events for each day, while the lines show the running 7-day average. The lower plots show details from October 2001 to March 2002 (b) and from November 2002 to February 2003 (c). In order to emphasize the good correlation between seismic and radar data, in (c) the lines represent the non-averaged values.

seismic network. Figure 5.3c shows the good correlation between both data sets from November 2002 to March 2003. Here, not only the trend matches, but also the rather strong fluctuations appear to correlate well. While the overall trends match most of the time, this does not hold for certain time periods. Especially, from October 2001 to March 2002 the number of instabilities detected by the radar decreases, while the number of seismically deduced rockfalls slightly increases (see Figure 5.3b). Also, the radar data does not follow the slight increases in the seismic data in September 2002 and August 2003 (Fig. 5.3a). The slightly increased activity in September 2002 is hardly visible in the radar data and during August 2003 we detect no increase in activity using the radar.

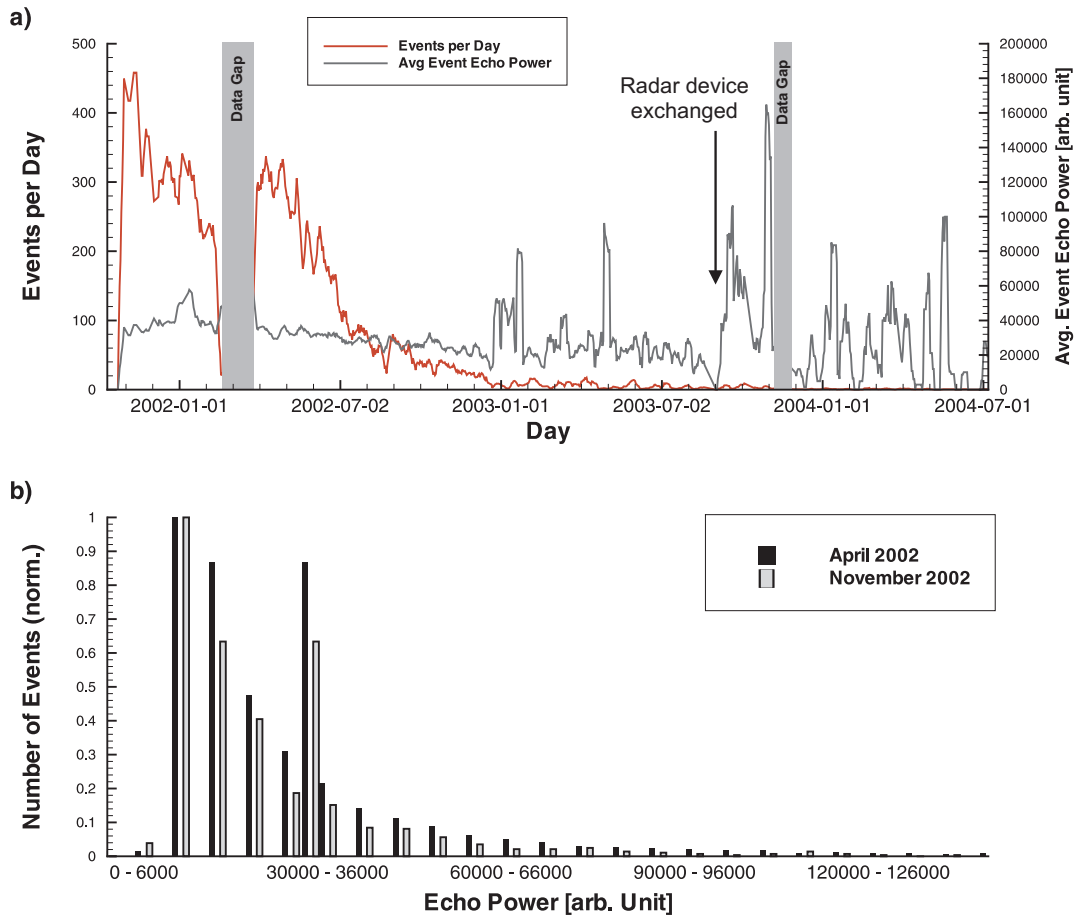


Figure 5.4: (a) Comparison of the daily number of rockfall events and the daily averaged event echo power. The event echo power is calculated by summing up the total echo power of all Doppler spectra of an event. (b) Comparison of the event echo power distributions during April and November 2002.

The echo power received by the radar system scales roughly with the volume of the material that moves through the beam (see Section 5.2). Thus, the summed echo power over the whole duration of a radar event, in the following referred to as event echo power, is an approximate measure for the event size. Figure 5.4a shows the daily averaged event echo power. For comparison the red line shows the daily number of instability events. While the number of events decreases between April and November 2002 from about 340 events to 40 events per day, the average event echo power remains roughly constant throughout this time period. A similar observation holds for the period from October 2001 to February 2002. Only following January 2003 the data shows more scatter, which is due to a weak statistical basis (small number of events). Figure 5.4b shows that in fact the distribution of event sizes estimated by the event echo power does not change significantly from April to

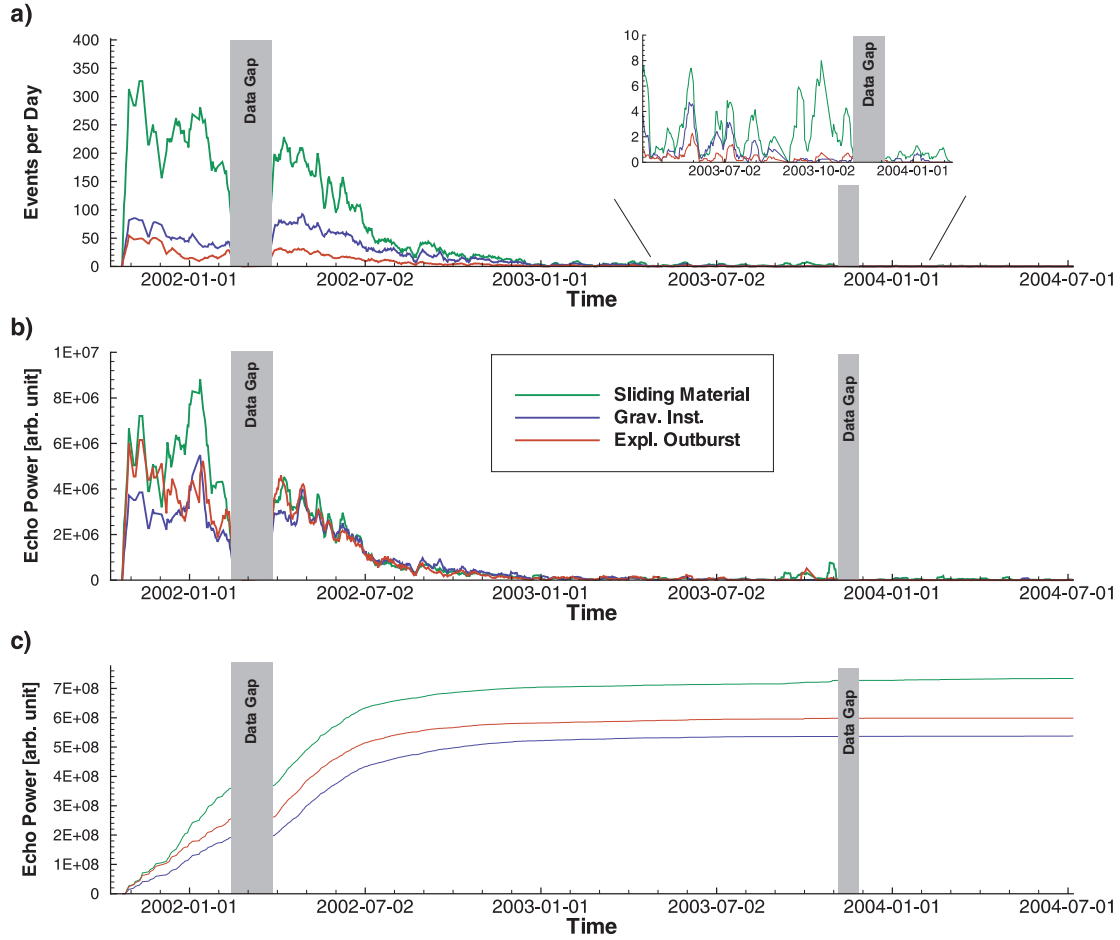


Figure 5.5: Comparison of occurrence frequency and magnitude of the different types of radar events. (a) daily number of events, (b) daily summed echo power and (c) cumulative daily summed echo power.

November 2002.

Changes in the relative frequencies of sliding events, gravitational break-offs and explosive outbursts would suggest a change in the activity style. The largest activity change observed so far by the radar has been the decrease during the period from November 2001 to August 2003. For this period Figure 5.5a shows the daily number of instability events broken down into events of sliding material, gravitational break-offs and explosive outbursts. Most events are caused by sliding material, they occur about 3 times as often as gravitational break-offs and about 6-7 times more often than explosive outbursts. These ratios remain roughly constant for the whole period between November 2001 and November 2002. Even the realignment of the radar beam in March 2002 has no significant impact on the ratio between the different types of events. Following November 2002 we observe too few events to further

follow up this observation. Only between December 2001 and January 2002 the number of sliding events is found to rise compared to gravitational break-offs and explosive outbursts.

Figure 5.5b shows the daily summed echo power for the three event types. The amount of material involved in the different types of events appears to be much more similar than the actual number of events. Especially following March 2002 the summed echo powers per event do not vary significantly. Because most events are due to sliding material during this time, these events are on average smaller than gravitational and explosive events. Again, only during the period between December 2001 and January 2002 we observe an increased echo power for sliding material compared to gravitational break-offs or explosive outbursts. This is also confirmed by Figure 5.5c, where the cumulative echo power is plotted. The relative increase of sliding material with respect to the other event types corresponds well to the observation of increased relative number of sliding events in Figure 5.5a.

The different types of instability events are mainly characterized by their mean velocity. We have to note that all velocities reported in the following are radial velocities (see Section 5.2). The mean velocity is calculated from a Doppler spectrum by first multiplying each velocity with its echo power, building the sum over all these products, and then dividing this "momentum" by the total echo power (see also Voege and Hort, 2007). An instability event is a sequence of Doppler spectra, and we get a time series of mean velocities for each event. Out of this series, we pick the maximum mean velocity throughout the event, which for simplicity will be referred to as *maximum event velocity* or just *event velocity* from here on.

Figure 5.6a shows the distribution of the event velocities for all three types of events. The distributions are stacked, so that the overall distribution of all events regardless of their event type is also shown. The overall distribution of the velocities is unimodal. The maximum is at about $2m/s$ and exponentially decreases towards higher velocities. Below $2m/s$ the number of events decreases much faster, and below $1.2m/s$ there is hardly any event. The number of sliding events is much higher than for gravitational and explosive instabilities as already observed in Figure 5.5. In order to look closer at the distributions for the different event types, Figure 5.6b shows the event numbers normalized for each event type. For sliding events the velocities range from 1.5 to $3.5m/s$. Gravitational break-offs have a velocity range from 3.2 to $5.2m/s$ and explosive outbursts from 4.8 up to $7.5m/s$. These distributions are obtained from the whole data set of nearly 3 years consisting out of approximately 57000 instability events.

We also looked for temporal variations in these distributions. Therefore, Figure 5.6c shows the event velocities averaged on a weekly basis for all three types of events from November 2001 to July 2004. The error bars show the standard deviation of the

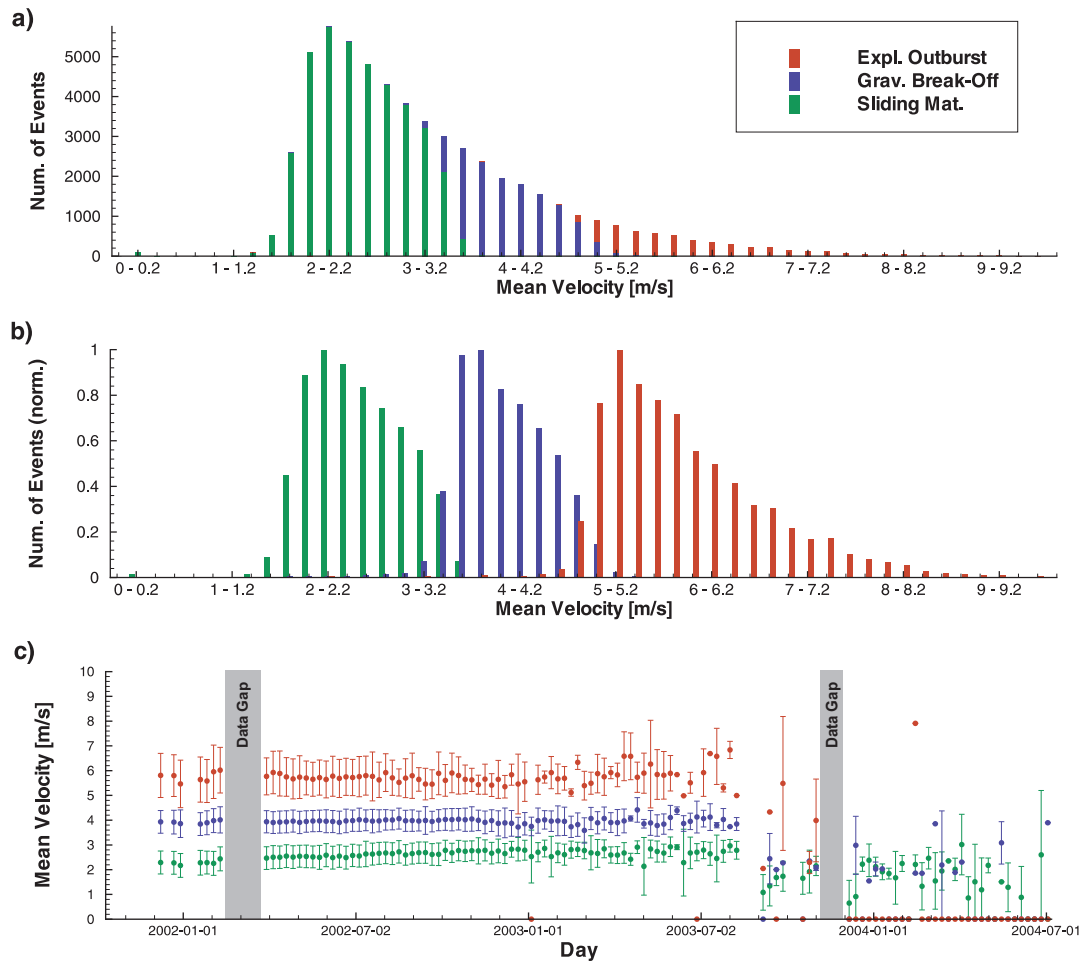


Figure 5.6: (a) Distribution of the maximum event velocities as a function of the number of events calculated from all instability events detected between November 2001 and July 2004. Each color represents one type of event: sliding material (green), gravitational break-off (blue) and explosive outburst (red). (b) The same distribution as in (a) but with event numbers normalized for each type of event. (c) Temporal evolution the maximum event velocity for each type of event. Dots are weekly averages and the error bars show the standard deviation during the corresponding week.

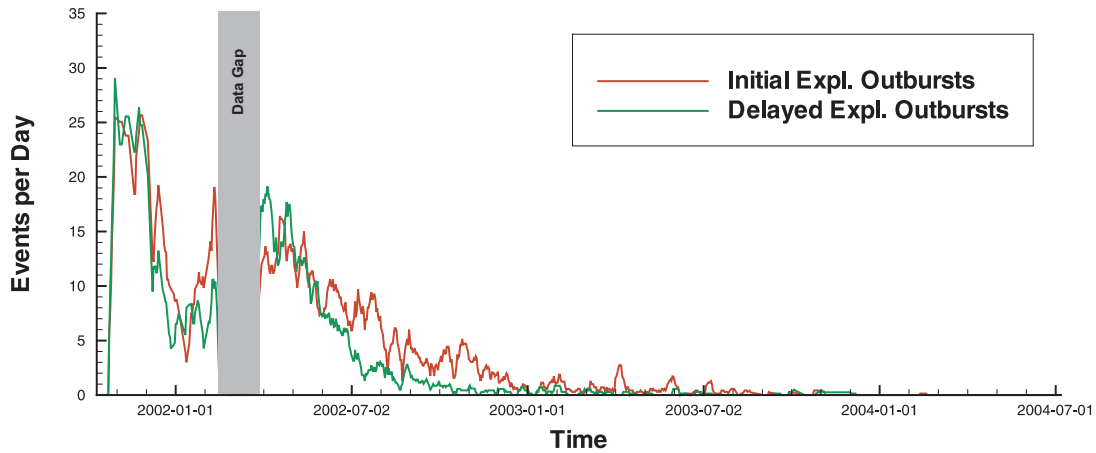


Figure 5.7: Number of events (7-day running average) with initial explosive outburst (red) and with gravitational break-off followed by an explosive outburst (green).

maximum event velocities for the corresponding week. The weekly average as well as the standard deviation of the event velocities do not change significantly between November 2001 to August 2003, although the dome activity has been continuously decreasing (compare Fig. 5.3a). The average event velocity for sliding material is about $2.5m/s$. For gravitational break-offs it is about $4m/s$ and for explosive outbursts about $6m/s$. Only in late 2003 the values scatter more because the total number of events is very small (< 20). Following August 2003 the event properties change significantly. This, however, is caused by another realignment of the radar beam, which has been carried out, after the radar had been replaced by a technically upgraded radar device.

Amongst the explosive instability events we are able to distinguish between two different types: events with initial explosive outburst and events with delayed explosive outbursts (see also Voegelé and Hort, 2006). In Figure 5.7 we compare the number explosive of events with initial outburst (red) to events with delayed outburst (green). Between November 2001 and March 2002 the numbers for both types of events are similar and follow the same trend. Only in late January 2002 the number of initial outburst events is significantly higher than for delayed events. After the radar beam has been realigned in March 2002, the number of events is again very similar for both types of events. However, following April 2002 the number of delayed events decreases faster than the number of initial outbursts until the number of events becomes very small in August 2003. Possible reasons for this observations are discussed in Section 5.4.

The radar system used at Merapi is also able to detect rainfall. The advantage of

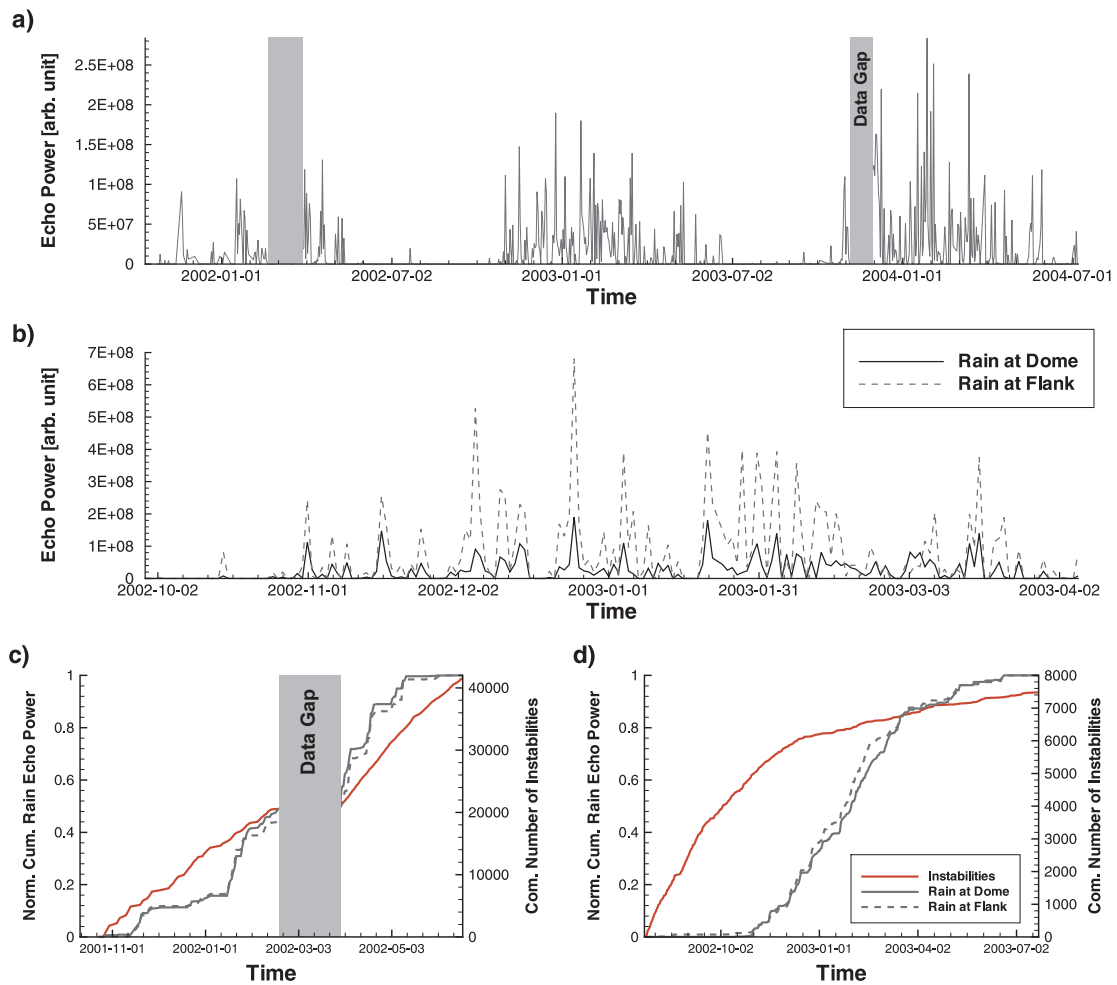


Figure 5.8: (a) Echo power of rain events summed on a daily basis from November 2001 to July 2004. Note that in August 2003 the radar device was replaced by a new instrument, which generally gives slightly higher echo powers. (b) Comparison of rainfall directly at the dome and rainfall at the lower flank for the rainy season 2002/2003. (c and d) Cumulative number of rockfalls (red) and cumulative echo power for rain events for the rainy seasons 2001/2002 and 2002/2003.

measuring rain by radar is that measurements can be made from a distant location and that measurements can be made for different range gates (see Section 5.2). Therefore, we measure rain directly at the dome and at a distance of about 2000m away from the dome in free air above the lower flank. Figure 5.8a shows rain measurements in the dome area for the period from November 2001 to July 2004 plotted as daily summed echo power. We can clearly see the rainy seasons 2001/2002, 2002/2003 and 2003/2004. In 2001/2002 the rain season seems to be weaker than in 2002/2003 and 2003/2004, but this may actually not be true as there is a significant data gap in February/March 2002. In addition, we did not observe the beginning of the season in this case. In Figure 5.8b we compare the rain measurements at the dome and at the flank of the volcano. The echo power for rain at the dome is generally less than at the flank. This is due to the geometric attenuation of the radar measurements, which is higher for larger distances. The correlation of both datasets, however, is very good, and no significant differences in the ratio between rain at dome and rain at the flank can be observed.

In order to look for a correlation between rainfall and dome activity we calculated the cumulative number of instability events and the cumulative sum of the echo power of rain events for the rainy seasons 2001/2002 (Fig. 5.8c) and 2002/2003 (Fig. 5.8d), respectively. The rainy season 2003/2004 is omitted, because the activity was too low. Because we are only interested in relative changes, all datasets have been normalized. Again, during both rainy seasons shown here, we can clearly see the similarity between rain at the dome and rain at the flank. The possibility of a correlation between dome instabilities and rainfall will be discussed in Section 5.4.

5.4 Discussion and Conclusion

Comparing rockfall monitoring by the seismic network (with manual detection/classification) of the Merapi Volcano Observatory with our radar data shows that the radar system provides useful new information about the lava dome activity. The radar is able to detect more instabilities/rockfalls than the seismic network during periods of high activity and similar numbers during times of low activity. From the radar data we can determine characteristic properties for the different types of instabilities, and we were able to observe a change in the relative numbers of events with initial explosive outburst and with a gravitational break-off followed by an explosive outburst. We have also shown that the radar is able to detect rain fall separately at the dome and at the lower flank, which can be used to investigate the impact of rainfall to dome activity. In the following we discuss the observed differences in the number of events detected by the radar system and the seismic network. We also investigate the characteristic properties of the different types of instabilities and discuss possible reasons for the observed change in the relative

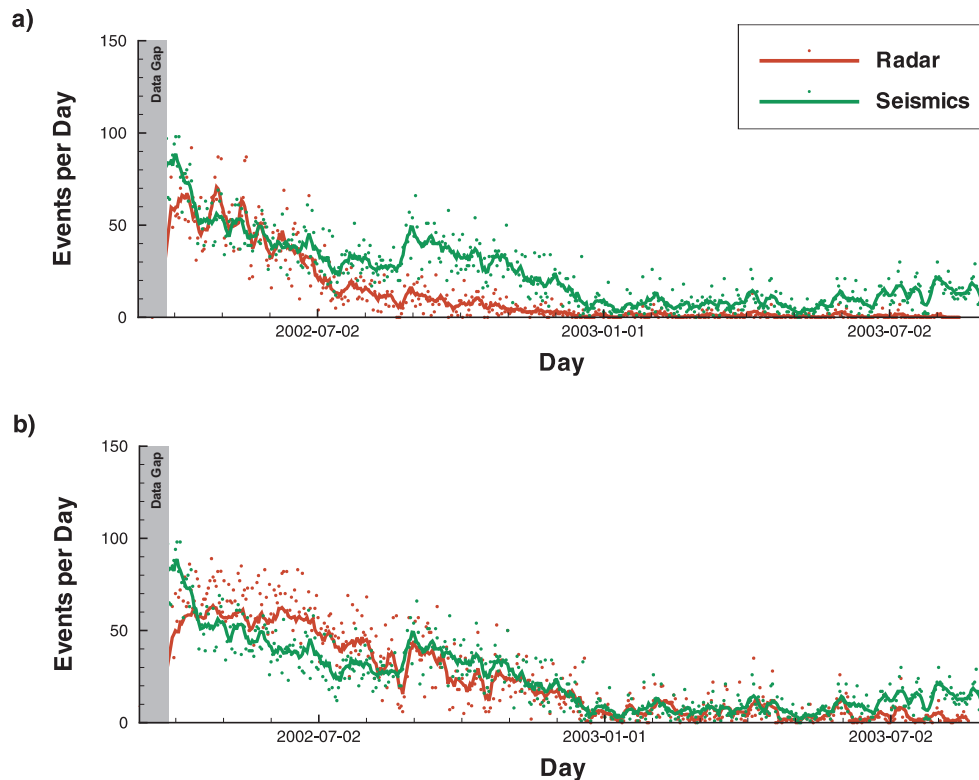


Figure 5.9: Comparison of the daily number of instability/rockfall events detected by radar and by seismic observations. The event detection for the radar data is altered in two different ways: (a) The threshold for the event detection is increased until the number of rockfalls detected by radar and seismics match right after the realignment of the beam at the end of the data gap in March 2002; (b) Successive events with a time difference of less than 6 minutes are considered as one event.

numbers of the two different types of explosive events. Finally, we analyze the rain measurements for possible correlations with dome activity.

5.4.1 Sensitivity of the radar system

During times of low activity the numbers of events are similar for both observational methods, and the good agreement between both data sets indicates that the fluctuations in the number of instabilities/rockfalls are real and not "noise" introduced by the measurement techniques (see Fig. 5.3a and c). However, we have shown that the radar system detects significantly more events than manually identified from the seismic data when the activity is high. In order to determine why, we manipulated

the radar data in order to simulate two different effects, which might cause the lower number of events identified in the seismic data: (a) higher sensitivity, i.e. the radar is able to detect smaller events, and (b) events are less likely to overlap due to the shorter duration than in the seismic data (compare Voegelé and Hort, 2007). We assume that the most active spot at the dome has been covered completely by the radar beam after the realignment in late March 2002. Therefore, the numbers of events should be similar during the period just following the realignment. In order to test the first possibility, we reduce the sensitivity of the radar artificially by increasing the threshold for our event detection algorithm, until we reach similar daily event numbers for the radar and the seismic data for late March 2002 (see Fig. 5.9a). While now the numbers match for the high activity in April and May 2002, we find significantly less events than detected by the seismic system during the low activity in December 2002. The second possibility is tested by simulating longer event durations. Therefore, we set a threshold for the minimum time-gap allowed between two successive events. Again, this threshold is increased until the number of daily events matches for both data sets just after the realignment of the beam. The best match for the numbers of events is achieved for a minimum gap of 6 minutes between two events in the radar data. Figure 5.9b shows that now the data sets match during the whole time series from March 2002 until December 2002. This indicates, that the overlap of succeeding events has the larger impact on the identification of rockfalls by the system observer/seismic network. However, we have to note that due to the manual identification of seismic events, the sensitivity of both systems' have to be compared with caution. In the presence of a huge number of events per day an observer might ignore smaller events, and thus his "threshold" could vary in time. Also, in seismic measurements small rockfalls can also appear as multiphase events (person. comm. J. Wassermann). In this case, the radar measurements could offer a valuable independent source of information and could help to discriminate seismic rockfall events from seismic events originating from the inside of the volcano.

Next, we investigate the differences between the trends of the radar data and the seismic data that we observe between October 2001 and March 2002 (Fig. 5.3b). Two considerations are important to explain the decrease of events observed by the radar, while the number of seismic events increases slightly: a) the radar system observes only a small part of the dome, while the seismic network is able to register rockfalls independently of their origin and b) following the data loss of a few weeks in February and March 2002 the radar beam was realigned to observe the most active spot at the dome. We conclude that the activity at the spot observed by the radar between October 2001 and March 2002 decreased, while the overall activity at the dome remained constant. After reorienting the radar beam to the most active spot in March 2002, the number of rockfalls is nearly at the same level as in November 2001. Therefore, the activity has been shifting to another spot at the dome, which was also confirmed visually, when the radar beam was realigned in March 2002. This example shows that combining seismic measurements with radar observations helps to monitor changes in the location of the main rockfall activity. In fact, this

is a unique opportunity to observe such changes independent of visual observations. This is most important, since the summit of Merapi is covered by clouds very often, making visual observation sometimes impossible for longer periods of time.

However, radar measurements by only one or two radar systems cannot replace seismic rockfall measurements. The slight increases in the number of rockfalls in the seismic data in September 2002 and August 2003 is not or only hardly visible in the radar data (see Fig. 5.3a). These activities must therefore have occurred at the edge or outside of the area observed by the radar beam. Because the activity was very low during both time periods an accurate realignment of the radar beam was not possible. While the measurements of the radar are independent of visibility conditions, this does not hold for the alignment of the radar beam. Because the active spot has to be identified visually, this is very difficult, when there is very low activity with only a few small rockfalls per day. When the activity is high, only a few minutes of good visibility are needed to identify the active spot and to realign the radar beam.

5.4.2 Dynamic Processes During Instability Events

A significant change in the dynamic processes during the observation period could not be observed. The relative numbers of the different types of instability events, i.e. sliding material, gravitational break-offs and explosive outbursts, did not change significantly between November 2001 and August 2003. The same holds for the echo power, i.e. the size of the events. Only between December 2001 and January 2002 the number of sliding events increased slightly compared to gravitational and explosive events. This might have several reasons. One possibility is that this is due to the most active spot moving out of the focus of the radar beam, as discussed above. According to visual observations from Babadan in March 2002 the activity moved to the upper right with respect to the center of the radar beam. Thus, the radar did not observe the onsets of some events, whereas the resulting rockfalls still passed the radar beam and therefore were classified as purely sliding events. Because we still observe explosive events, the activity cannot have completely left the radar beam, though. Another possibility is a change in the style of activity, e.g. the pressure within the dome material decreases, and thus the number of explosive events also decreases. However, only from the radar data we are not able to decide, which reason is most likely.

In September 2003 we also observe a relative increase of sliding material, which is shown in the blowup section of Figure 5.5a. This, however, is due to a reorientation of the radar beam in late August 2003. Because the activity was very low, no clear active spot could be identified. Therefore, the beam was aligned towards a canyon at

the lower edge of the dome in order to detect material, which is moving through the canyon after breaking off the dome somewhere above. In this case the canyon acts as a channel collecting material from a area of the dome larger than it could be covered by the radar alone. The increase in the number of sliding events is accompanied by a decrease in the maximum event velocity from about 2.5m/s down to $1.5 - 2\text{m/s}$ (Fig. 5.6c). The velocity of sliding material mainly depends on the tilt of the slope and the friction between material and slope. Thus, the lower velocities are likely to be due to a smaller tilt of the slope below the dome or due to a higher friction of the material with the ash that has accumulated further away from the dome.

More interesting are the observations of relative changes between the number of explosive events that start gravitationally and the number of events that start explosively. Due to magma extrusion the uppermost part of the conduit and the interior of the dome may be subject to large overpressures (e.g. Melnik and Sparks, 1999). We assume that initial explosive outbursts are triggered by a structural failure, which causes a release of pressure and leads to degassing and thus to an explosive outburst. Due to the geometry of the dome such explosive outbursts are usually small directed lateral blasts. First, this type of event has been observed at Montagne Pelée during its eruption in 1902 and therefore are called Pelean-type dome collapse (see e.g. Voight et al., 2000). Events with a delayed explosive outburst start as a gravitational instability (Merapi-type). Single blocks produced by an instability can be rather large (several meters in diameter). When such a block hits the slope after breaking off the dome it fractures, which again causes a release of pressure inside the block, and thus the block fragments explosively. At Unzen Sato et al. (1992) and Ui and Fujinawa (1999) were able to document such processes using video recordings. However, it is also possible that the gravitational break-off causes a release of pressure in the underlying dome material, and thus again an explosive outburst occurs due to degassing. First signs of a change in the relative number of these two types of explosive events in January 2002 are of relative short duration (see Fig. 5.7) and might be associated with the shift in activity discussed above. However, following April 2002 a faster decrease of explosive events starting gravitationally is observed for about one year. The reason for the faster decrease might be that with continuously decreasing activity temperature and pressure in the dome material decrease most quickly near the surface of the dome. Thus, blocks gravitationally breaking off the dome are less likely to fracture explosively. Initial events are supposed to be driven from the inside of the dome, where temperature and pressure decrease slower, and thus also the number of initial events decreases slower. However, because the difference is not very large, this needs further verification by additional measurements.

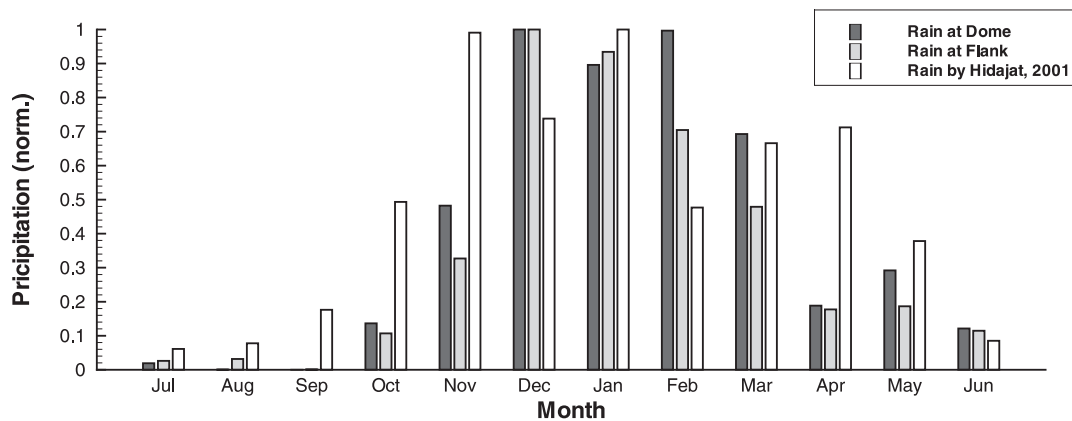


Figure 5.10: Normalized monthly precipitation at Merapi volcano. Blue: average precipitation between 1981 and 1990 taken from Hidajat (2001). Red: precipitation measured by the radar system at the dome between November 2002 and October 2003. Green: precipitation measured by the radar system at the lower flank for the same period.

5.4.3 Volcanic Activity and Rain

The influence of rainfall on the activity of lava domes has already been discussed by several authors. At Unzen Yamasato et al. (1998) repeatedly observed an increase in the number and size of pyroclastic flows due to dome instabilities after heavy rainfall. At Soufriere Hills Volcano, Montserrat, two major dome collapses were found to coincide with extremely heavy rainfall events (Matthews et al., 2002). A thermodynamical model has been introduced by Matthews and Barclay (2004), which leads to the conclusion that about 20 – 30mm rainfall suffices to trigger a significant collapse. A thermo-hydrologic mechanism for rainfall-triggered collapses has been introduced by Elsworth et al. (2004). At Merapi, Neuberg (2000) found a correlation between rainfall and dome activity. A link between fumarole temperature and rainfall has been observed by Richter et al. (2004).

The radar systems used at Merapi volcano are modified rain radars. For rain measurements these rain radars are pointed vertically upwards, so that from the terminal fall velocity and from the reflected echo power a rain rate can be calculated. In order to calculate an absolute rain rate two conditions must be met: a) the rain has to cover the complete radar beam, and b) the velocity measured by the radar has to be the true terminal fall velocity of the rain drops (Peters et al., 2002). Unfortunately, these conditions do not hold for the installations at Merapi, because the radar beam is not pointing vertically upward. Because of the small elevation angle, the radar beam has a much larger horizontal extend, and thus it is less likely than for a vertical

looking radar that a very local rain event covers the complete radar beam. Vertical looking radars measure the true fall velocity of the rain drops, even when strongly influenced by horizontal wind drift. At Merapi, the terminal fall velocity has to be calculated by projecting the measured velocity to the vertical fall direction. Here, we have to assume that the rain is actually falling vertically, which is often violated by horizontal wind drift. Therefore, a determination of an absolute rain rate from our measurements is impossible. However, rain measurements made by the radar systems can be used to monitor relative changes in the rain rate over time. Assuming that the raindrop size does not vary significantly the echo power during rain events roughly scales with the actual rain rate. Although, the rain drop size does certainly vary from one rain event to another, we assume that on average they do not vary significantly.

Central Java has a typical tropical climate with two main seasons: dry season and rainy season. The annual precipitation at Merapi Volcano is about 3200mm (Hidajat, 2001). During the dry season between May and October only very little precipitation occurs with about 50mm per month. The rainy season usually starts in mid October and lasts until mid May (see Fig. 5.10). The precipitation rises to $200 - 500\text{mm}$ per month and has its maximum in January with about 540mm . Figure 5.10 shows that although it is not possible to give absolute rain rates, the relative amount of monthly rainfall measured by the radar between November 2002 and October 2003 is consistent with the record of Hidajat (2001). This makes us confident that the relative amount of rain given by the echo power of rain events (see Fig. 5.8) can be used to investigate the radar data for possible correlations between rainfall and dome activity.

However, during the whole observation period no such correlation could be observed. Even the sharp increase in cumulative rainfall during mid January 2001 has no impact on the number of instabilities (Fig. 5.8c). Also the onset of the rainy season 2002/2003 does not seem to have any impact on the number of instabilities, which continue to decrease as during the dry season before (Fig. 5.8d). The lack of a correlation might just be due to the fact that during the whole period between November 2001 and July 2004 the activity continuously decreased with no further dome growth. It is still possible that a correlation can be observed during increasing activity, when the pressures and temperatures are higher due to fresh material. Unfortunately, the recent activity between May and July 2006 has not been observed properly by the radar system. However, since the activity has mainly occurred in the dry season, it is not very likely that an impact of rainfall on dome activity could have been observed.

Strong rain fall, however, also influences the detection of instability events by the radar system. Figure 5.11 shows the number of instabilities and the summed echo power for rain events as function of the time of day (local time) binned in 15 minutes intervals, once for the dry season 2002 (Fig. 5.11a, mid May to mid October) and

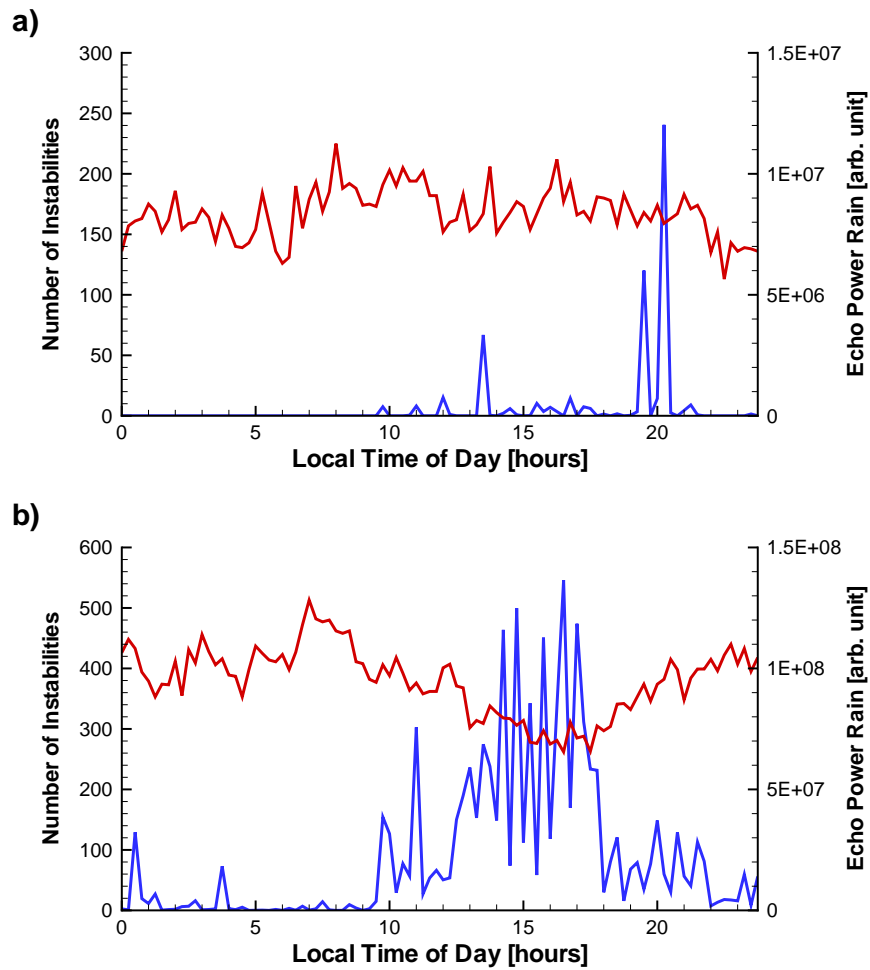


Figure 5.11: Number of instabilities (red) and the summed echo power of rain events (blue) as function of the local time of day binned in 15 minutes intervals: (a) dry season 2002 (mid May – mid October), and (b) rainy season 2001/2002 (November – mid May). Please note the differences in echo power amplitude between panel (a) and (b).

once for the rainy season 2001/2002 (Fig. 5.11b, beginning of November till mid May). The instabilities seem to be equally distributed throughout the day during the dry season. Only at 6am the number of events appears to increase slightly and decreases again during the day. During the rainy season we observe significantly less instabilities between about 12am and 8pm compared to the rest of the day. This clearly correlates with the rain rates for the same hours. However, the decrease of rockfalls during hours of high rain rates is not due to an influence of rain on the dome activity. When the radar observes strong rainfall, the echo power is usually much stronger than the echo power of instability events (see Voegelé and Hort, 2007). It is therefore impossible to detect instabilities during heavy rain, because they are superimposed by the strong rain signal. Figure 5.11b shows no delayed impact of rainfall to the number of instabilities, and thus we estimate the true numbers of instabilities (per 15 minutes bin) to be about 400 throughout the day. During about 8 hours the numbers of instabilities are therefore reduced by about 30%. Averaged over the full day we can estimate that we detect about 10% less instabilities due to strong rain events occurring during the day. Thus, the impact on instability monitoring is not very strong.

In Figure 5.11 we also observed that the number of rockfalls increases slightly at about 6am in the morning. This observation supports the possibility of an influence of sunlight warming to the stability of parts of the dome as it was discussed by Neuberg (2000). Due to the high altitude of 2980m above sea level, the temperature varies significantly between day and night. The rising sun heats the eastern side of the dome quickly up about 20°C, while the western side remains in the shade. This could lead to a temperature-induced stress field, which causes a slightly increased number of instabilities. However, the heating by sunlight only influences dome material very close to the surface and since the observed variations are very small this has to be considered with due caution.

5.4.4 Conclusion

Doppler radar measurements are relatively new in the field of volcanic monitoring and only few measurements and observations have been published so far. The data presented in this paper represents the first long-term data set of Doppler radar measurements available for lava dome activity. Although, no significant changes in the type of activity could be observed due to the continuously decreasing activity, the observations provide important information about the activity at the dome. In order to assess the full potential of the radar system, data from a complete volcanic crisis would be needed. Unfortunately, this could not be achieved for the activity in 2006, because the activity has been directed south/southeast, while the radar systems have been installed in the west of the volcano. However, especially the comparison with the seismic data shows that Doppler radar measurements can significantly improve

monitoring of dome instabilities and resulting rockfalls and block and ash flows.

Acknowledgments

We thank the staff of the MVO (especially Agus Sampurno and Anton Sulistio) for their cooperation and continuous support of this project. Thanks also to Carl Gerstenecker for providing the digital elevation model of Merapi. This work was funded by the Deutsche Forschungsgemeinschaft through grants Ho 1411 14-1,2 and 15-1.

Chapter 6

Conclusion and Outlook

The main goal of this thesis was to develop a Doppler radar monitoring system that is capable of continuous observation and detection of dome instabilities at the active lava dome of Merapi volcano. Besides the radar device itself, the most important component of the system is the logging unit. While the radar is a modified version of a commercial rain radar, the logging unit had to be developed specifically for this application. The hardware is based on standard but low power computer technique and therefore all necessary communication interfaces are provided. By far the largest effort has been undertaken in developing a reliable and easy-to-use software system that controls the whole system, stores the measured data and provides communication via radio transmission and GSM-Modem. The observatory unit takes advantage of a professional database system that stores the data and provides access from anywhere in the intranet of the Merapi Volcano Observatory. A processing and classification software package has also been developed, which can be used via a comfortable user interface.

The Doppler radar system provides the first "quasi-visual" observations of dynamic processes at lava domes independent of visibility conditions. They provide detailed information about the velocity and the amount of material moving at the dome. This information cannot be obtained by any other measurement technique, and therefore the radar systems enhance the observation and characterization of the dome activity significantly. Three different types of instability events could be identified by Doppler radar measurements: sliding material, gravitational break-offs and explosive outbursts. Sliding material and gravitation break-offs are considered to be exclusively driven by gravitational forces, gravitational break-off representing the mechanical failure of an unstable part of the dome and sliding material representing loose material sliding/tumbling down the slope. Explosive events are considered to be driven from the inside of the dome by degasing due to a release of pressure, which

can in turn result from a mechanical failure of a part of the dome.

Due to the huge amount of data (80GB of raw data and about 80.000 radar events between October 2001 and August 2004) an automatic classification system has been developed. Because the types of a radar event is mainly characterized by the shape of its Doppler spectra, first, each single Doppler spectrum is classified according to the underlying dynamic process. The event class is then determined from the resulting sequence of classified Doppler spectra. Single Doppler spectra can be classified using a variety of different feature vectors and two different classifier models: artificial neural networks and the K-nearest-neighbor method. Because both methods require supervised learning, an expert has to classify manually a set of training spectra, which is used to train the classifier. The best choice of the feature vector depends on the classification strategy. The discrimination of all five classes in one classification step achieved best result simply using a preprocessed section of the Doppler spectrum. The "two-step" classification achieves the best performance, when the relative total echo power for each half of each range gate is used to discriminate disturbances, rain, and instabilities. The mean and the standard deviation in the range gate at the dome are used to discriminate the three types of instabilities. The highest classification rate for Doppler spectra with 90.61% is achieved by the neural network classifier. However, the K-nearest-neighbor classifier achieved only about 2–3% smaller classification rates.

The classification for complete events achieves similar accuracy, with about 89%. An important fact is that the discrimination between disturbances and rain on one side and instabilities on the other side is much more accurate with about 98% correct classifications. The classification rate for the discrimination between the three types of instabilities is lower (about 86%). This is mainly due to the fact that the characteristics of these events are somewhat continuous. In some cases, also for the expert it is difficult to decide, whether there is a gravitational break-off or even an explosive outburst visible.

While the performance is very similar for both classifier models with only a slight advantage for the neural network, both models have certain advantages and disadvantages. Because neural networks are trained in advance, they are very fast when applied to new data. K-nearest-neighbor classifiers have to compare new data to the complete training set, and thus can be very slow. However, the advantage of the K-nearest-neighbor classifier is its simple implementation, and during classifier design, i.e. when searching for a suitable feature vector, it can easily and quickly be applied to test datasets.

The automatic classification system has been applied to a large data set of radar measurements. Starting in late October 2001 about 57.000 instability events have been detected until August 2004. Following 2004, the activity had decreased to a

minimum and hardly any instabilities could be observed. In 2005 and early 2006 several system damages, e.g. by lightning, caused relatively long data gaps. During the volcanic crisis between April and July 2006 one system (Gemer) has been operating, however, the activity was directed towards the south-east and thus could not properly be observed by the radar system. Comparison of the daily number of instability events detected by the radar and the number of rockfall events manually identified from the data of the MVO seismic network showed that the radar system detects more events, especially, during periods of high activity. This high level of sensitivity, however, requires a precise alignment of the radar beam to the active area at the dome. Tests showed that the higher number of events in the radar data does not result from a higher sensitivity but from a better separation of events. For a set minimum gap of 6 minutes between radar events, we achieved the best fit of radar and seismic data. In combination with seismic measurements the radar can enhance the monitoring of the location of the most active spot at the dome, even when the dome cannot be observed by the naked eye. When the number of event decreases in the radar data, a comparison with the seismic data shows if this is due to a decrease or a shift in activity.

The relative numbers of the different types of instabilities has been similar throughout the observation period, and thus a significant change in the type of activity has not been observed. Most events have been due to sliding material, followed by gravitational break-offs and explosive outbursts. Only between December 2001 and February 2002 the number of sliding events increased slightly with respect to gravitational and explosive events which is probably associated to the spatially shifting activity. After the radar beam has been aligned to the lower edge of the dome in August 2003 we observe almost exclusively sliding material events. Between March 2002 and January 2003 the radar data also shows that events with an initial explosive outburst decrease slower than explosive events with a gravitational precursor. The later events are associated with large blocks breaking off the dome, which fracture explosively when hitting the slope. The reason for the faster decrease of these events might be that with continuously decreasing activity temperature and pressure in the dome material decrease most quickly near the surface of the dome. Thus, blocks gravitationally breaking off the surface of the dome are less likely to fracture explosively. Initial events are supposed to be driven from the inside of the dome, where temperature and pressure decrease slower, and thus also the number of initial events decreases slower. The observed differences are, however, not very large, and therefore this needs further verification.

The Doppler radar systems provide the first opportunity to observe rain directly falling at the dome from a remote position. Although no absolute rain rates can be obtained, the relative rain rates are consistent with long-term rain records. A correlation between rainfall and instabilities could not be observed. Since the activity constantly decreased throughout the observation period, this might be different in case of an arising volcanic crisis. Because the signals of instabilities can be su-

perimposed by strong rain signals, we detect approximately 10% less instabilities in the rainy season than in the dry season. Because no delayed impact of rainfall to the number of instabilities has been observed, this reduced number of instabilities does not seem to be related to dome activity. However, this should be verified by comparing the radar data to a seismic event dataset with better temporal resolution (i.e., at least event per hour).

Although we were not able to properly observe a complete volcanic crisis, the results of the thesis show that Doppler radar measurements can significantly enhance monitoring of active lava domes. Even a single instrument provides useful new information about the processes at the dome and in combination with seismic measurements provide additional information about the location of the main activity. However, for a complete coverage of the dome at Merapi at least 5 radar systems would be needed.

The radar systems installed at Merapi still have a prototype character, and therefore the system's infrastructure needs further development. Especially the electromechanical mounting caused a lot of trouble. The control unit is not designed for long-term application and therefore had always to be deactivated after the radar beam had been aligned. Therefore, it was not possible to change the radar beam alignment remotely from the MVO, as considered at the beginning of the project. Besides that, it turned out that the mounting was too weak for the 120cm offset mirror and after 3 years it had to be stabilized by additional mechanical fixations. For future applications a robust mechanical mounting has to be developed, which also can be adjusted with higher precision. This, however, has not been installed at Merapi yet.

Providing the logging unit with display, keyboard and mouse also turned out to be unnecessary. Due to today's network technology, the system can easily be controlled remotely from a laptop. Therefore, the software design of the logging unit should be changed completely to a Linux system. Compared to Windows 2000[®], Linux provides easier remote access and it can be reduced to those system components that are essential for the radar software. Some of the tasks of the logging unit could also benefit from Linux mechanisms like cron-jobs, which could be used to restart the system in case the radar software hangs. Such consideration have already been taken into account during development of the processing and classification software, which has been designed platform independent and thus can be applied on Linux as well as on Windows[®] systems. Because our colleagues at the MVO are most familiar with Windows[®], the user interfaces should remain on the Windows platform. In order to achieve easier and more flexible remote access to the radar system from the MVO, the current radio modems could be exchanged by bidirectional Wireless-Lan connections, which have a higher data transmission rate and already provide basic communication protocols. Especially, when the logging unit is designed to be exclusively remotely controlled, this would significantly reduce the need to visit the

station for maintenance work.

Future applications at other dome building volcanoes are important to establish the Doppler radar measurements as state of the art monitoring technique for lava dome activity. In case only short-term measurements are planned, the system can easily be modified to the special needs, e.g. a smaller mirror can be chosen if the distance between radar and dome is shorter, the camera can be exchanged by a telescopic sight, and components like the radio transmission or the GSM-modem can be left out. Interesting volcanoes would be, e.g. Soufriere Hills on Montserrat and Unzen in Japan.

Bibliography

- Bayes, T. (1763). An essay towards solving a problem in the doctrine of chances. *Philosophical Transactions of the Royal Society (London)*, 53:370–418.
- Bishop, C., editor (1995). *Neural Networks for Pattern Recognition*. Oxford University Press.
- Chouet, B., Hamisevicz, N., and McGetchin, T. R. (1974). Photoballistics of volcanic jet activity at Stromboli, Italy. *J. Geophys. Res.*, 79:4961–4976.
- Crandell, D. R., Booth, B., Kusumadinata, K., Shimozuru, D., Walker, G. P. L., and Westercamp, D., editors (1984). *Source-book for Volcanic Hazard Zonation*. Unesco.
- Donnadiou, F., Dubosclard, G., Cordesses, R., Druitt, T., Hervier, C., Kornprobst, J., Lénat, J., Allard, P., and Coltelli, M. (2005). Remotely monitoring volcanic activity with ground-based Doppler radar. *EOS, Transactions of the American Geophysical Union*, 86(21):201–204.
- Dowla, F., Taylor, S., and Anderson, R. (1990). Seismic discrimination with artificial neural networks. *Bulletin of the Seismological Society of America*, 80(5):1346–1373.
- Dubosclard, G., Cordesses, R., Allard, P., Hervier, C., Coltelli, M., and Kornprobst, J. (1999). First testing of a volcano Doppler radar (voldorad) at Mount Etna, Italy. *Geophysical Research Letters*, 26:3389–3392.
- Dubosclard, G., Donnadiou, F., Allard, P., Cordesses, R., Hervier, C., Coltelli, M., Privitera, E., and Kornprobst, J. (2004). Doppler radar sounding of volcanic eruptions at Mount Etna. *Bull. Volcanol.*, 66(5):443–456.
- Duda, R., E.Hart, and Stork, D. (2001). *Pattern Classification*. John Wiley & Sons, Inc., 2nd edition.
- Elsworth, D., Voight, B., Thompson, G., and Young, S. (2004). Thermal-hydrologic mechanism for rainfall-triggered collapse of lava domes. *Geology*, 32(11):969–972.

- Fahlman, S. (1988). Faster-learning variations on back-propagation: An empirical study. In Touretzky, D., Hinton, G., and Sejnowski, T., editors, *Proceedings of the 1988 connectionist models summer school*, pages 38–51, San Mateo. Morgan Kaufmann.
- Falsaperla, S., Graziani, S., Nunnari, G., and Spampinato, S. (1996). Automatic classification of volcanic earthquakes by using multi-layered neural networks. *Natural Hazards*, 13:205–228.
- Fink, J. and Anderson, S. (2000). Lava domes and coulees. In Sigurdson, H., Houghton, B., McNutt, S., Rymer, H., and Stix, J., editors, *Encyclopedia of Volcanoes*, pages 307–319. Academic Press.
- Friedel, S., Byrdina, S., Jacobs, F., and Zimmer, M. (2004). Self-potential and ground temperature at Merapi volcano prior to its crisis in the rainy season of 2000–2001. *J. of Volcanol. and Geotherm. Res.*, 134:149–168.
- Gertisser, R. and Keller, J. (2003). Temporal variations in magma composition at Merapi volcano (central Java, Indonesia): magmatic cycles during the past 2000 years of explosive activity. *J. of Volcanol. and Geotherm. Res.*, 123:1–23.
- Harris, D. and Rose, W. (1983). Estimating particles sizes, concentrations, and total mass of ash in volcanic clouds using weather radar. *Geophysical Research Letters*, 88:10969–10983.
- Harris, D., Rose, W., Roe, R., and Thompson, M. (1981). Radar observations of ash clouds using weather radar. *U.S. Geol. Surv. Prof. Pap.*, 1250:322–333.
- Hidajat, R. (2001). Risikowahrnehmung und Katastrophenvorsorge am Merapi in Indonesien. Technical report, Sonderveröffentlichung des Deutschen Komitee für Katastrophenvorsorge e.V. (DKKV). (in German).
- Hidayat, D., Voight, B., Langston, C., Ratdomopurbo, A., and Ebling, C. (2000). Broadband seismic experiment at Merapi volcano, Java, Indonesia: very-long-period pulses embedded in multiphase earthquakes. *J. of Volcanol. and Geotherm. Res.*, 100:215–231.
- Hornik, K., Stinchcombe, M., and White, H. (1992). Multilayer feedforward networks are universal approximators. *Neural Networks*, 2:359–366.
- Hort, M. and Seyfried, R. (1998). Volcanic eruption velocities measured with a micro radar. *Geophysical Research Letters*, 25(1):113–116.
- Hort, M., Seyfried, R., and Voege, M. (2003). Radar Doppler velocimetry of volcanic eruptions: theoretical considerations and quantitative documentation of changes in eruptive behaviour at Stromboli volcano, Italy. *Geophys. J. Int.*, 154:515–532.
- Hort, M., Voege, M., Seyfried, R., and Ratdomopurbo, A. (2006). In situ observation of dome instabilities at Merapi volcano, Indonesia: A new tool for volcanic hazard mitigation. *J. of Volcanol. and Geotherm. Res.*, 153:301–312.

- Kienle, J. and Shaw, G. (1979). Plume dynamics, thermal energy and long-distance transport of vulcanian eruption clouds from Augustine volcano, Alaska. *J. of Volcanol. and Geotherm. Res.*, 6:139–164.
- Kollias, P. and Albrecht, B. (2000). The turbulence structure in a continental stratocumulus cloud from millimeter-wavelength radar observations. *J. Atmos. Sci.*, 57:2417–2434.
- Kollias, P., Albrecht, B. A., Lhermitte, R., and Savtchenko, A. (2001). Radar observations of updrafts, downdrafts, and turbulence in fair-weather cumuli. *J. Atmos. Sci.*, 58:1750–1766.
- Kolmogorov, A. N. (1957). On the representation of continuous functions of several variables by superposition of continuous functions of one variable and addition. *Dokl. Akad. Nauk SSSR*, 114:369–373.
- Kurková, V. (1992). Kolmogorov’s theorem and multilayer neural networks. *Neural Networks*, 5(3):501–506.
- Lacasse, C., Karlsdóttir, S., Larsen, G., Soosalu, H., Rose, W., and Ernst, G. (2004). Weather radar observations of Hekla 2000 eruption cloud, Iceland. *Bull. Volcanol.*, 66:457–473.
- Lavigne, F., Thouret, J.-C., Voight, B., Suwa, H., and Sumaryono, A. (2000a). Lahars at Merapi volcano, central Java: an overview. *J. of Volcanol. and Geotherm. Res.*, 100:423–456.
- Lavigne, F., Thouret, J.-C., Voight, B., Young, K., LaHusen, R., Marso, J., Suwa, H., Sumaryono, A., Sayudi, D., and Dejean, W. (2000b). Instrumental lahar monitoring at Merapi volcano, central Java, Indonesia. *J. of Volcanol. and Geotherm. Res.*, 100:457–478.
- Le Guern, F., Gerlach, T., and Nohl, A. (1982). Field gas chromatograph analyses of gases from a glowing dome at Merapi volcano, java, indonesia, 1977, 1978, 1979. *J. of Volcanol. and Geotherm. Res.*, 14(3–4):223–245.
- Marzano, F. and Vulpiani, G. (2006). Volcanic ash cloud retrieval by ground-based microwave weather radar. *IEEE Trans. on Geoscience and Remote Sensing*, 44(11):3235–3246.
- Marzano, F. S., Vulpiani, G., and Rose, W. (2006). Microphysical characterization of microwave radar reflectivity due to volcanic ash clouds. *IEEE Trans. on Geoscience and Remote Sensing*, 44(2):313–327.
- Matthews, A. J. and Barclay, J. (2004). A thermodynamical model for rainfall-triggered volcanic dome collapse. *Geophysical Research Letters*, 31(5):L05614.1–L05614.4.

- Matthews, A. J., Barclay, J., Carn, S., G.Thompson, Alexander, J., R.Herd, and Williams, C. (2002). Rainfall-induced volcanic activity on Montserrat. *Geophysical Research Letters*, 29(13):1644.
- Melnik, O. and Sparks, S. (1999). Nonlinear dynamics of lava dome extrusion. *Nature*, 402:37–41.
- Neuberg, J. (2000). External modulation of volcanic activity. *Geophys. J. Int.*, 142:232–240.
- Ohrnberger, M. (2001). *Continuous Automatic Classification of Seismic Signals of Volcanic Origin at Mt. Merapi, Java, Indonesia*. PhD thesis, Mathematisch-Naturwiss. Fakultt, Universitt Potsdam, Potsdam, Germany.
- Ohrnberger, M., Wassermann, J., Budi, E., and Gossler, J. (2000). Continuous automatic monitoring of mt. Merapi's seismicity. *DGG Mitteilungen*, Sonderband IV:103–108.
- Peters, G., Fischer, B., and Andersson, T. (2002). Rain observations with a vertical looking micro rain radar (mrr). *Boreal Environment Research*, 7:353–362.
- Rajopadhyaya, D., May, P., Cifelli, R., S.K. Avery, C. W., Ecklund, W., and Gage, K. (1998). The effect of vertical air motions on rain rates and median volume diameter determined from combined uhf and vhf wind profiler measurements and comparisons with rain gauge measurements. *Journal of Atmospheric and Oceanic Technology*, 15:1306–1319.
- Ratdomopurbo, A. and Poupinet, G. (2000). An overview of the seismicity of Merapi volcano (Java, Indonesia), 1983-1994. *J. of Volcanol. and Geotherm. Res.*, 100:193–214.
- Rebscher, D., Westerhaus, M., Koerner, A., Subandriyo, A., Brodscholl, A., Kuempel, H.-J., and Zschau, J. (2000). Indonesian-German multiparameter stations at Merapi volcano. *DGG Mitteilungen*, Sonderband IV:93–102.
- Richter, G., Wassermann, J., Zimmer, M., and Ohrbeeger, M. (2004). Correlation of seismic activity and fumarole temperature at the mt. Merapi volcano (Indonesia) in 2000. *J. of Volcanol. and Geotherm. Res.*, 135:331–342.
- Ripepe, M., Rossi, M., and Saccorotti, G. (1993). Image processing of explosive activity at Stromboli. *J. Volcanol. Geotherm. Res.*, 54:335–351.
- Rose, W., Gu, Y., Watson, I., Yu, T., Bluth, G., Prata, A., Krueger, A., Krotkov, N., Carn, S., Fromm, M., Hundon, D., Viggiano, A., Miller, T., Ballentin, J., Ernst, G., Reeves, J., Wilson, C., and Anderson, B. (2003). The February-March 2000 eruption of Hekla, Iceland, from a satellite perspective. In Robock, A. and Oppenheimer, C., editors, *Volcanism and the earth atmosphere*, volume 139, pages 107–132. AGU Geophys. Monogr.

- Rose, W., Kostinski, A., and Kelley, L. (1995). Real-time c-band radar observation of 1992 eruption from Crater Peak/Spurr volcano, Alaska. *U.S. Geol. Surv. Bull.*, 2139:19–26.
- Rosenblatt, F. (1958). The perceptron: A probabilistic model for information storage and organization in the brain. *Psychological Review*, 65(6):386–408.
- Rumelhart, D., Hinton, G., and Williams, R. (1986). Learning representations by back-propagating errors. *Nature*, 323(9):533–536.
- Sato, H., Fujii, T., and Nakada, S. (1992). Crumbling of dacite dome lava and generation of pyroclastic flows at Unzen volcano. *Nature*, 360:664–666.
- Schmincke, H. (2004). *Volcanism*. Springer.
- Schneider, D., Rose, W., and Kelley, L. (1995). Tracking of 1992 eruption clouds from crater peak vent of mount spurr volcano, Alaska, using avhrr. *U.S. Geol. Surv. Bull.*, 2139:27–36.
- Schneider, S. (1983). Volcanic dust and climate: How clear is the connection? *Climate Change*, 5(2):111–113.
- Schwarzkopf, L. (2001). *The 1994 and 1998 block-and-ash flow deposits at Merapi volcano, Central Java, Indonesia: implications for emplacement mechanisms and hazard mitigation*. PhD thesis, Geomar Forschungszentrum, Universität Kiel, Kiel, Germany.
- Schwarzkopf, L. and Schmincke, H. (2000). Die vulkanwelt indonesiens. *Geograph. Rund.*, 4:4–11.
- Schwarzkopf, L., Schmincke, H., and Cronin, S. (2005). A conceptual model for block-and-ash flow basal avalanche transport and deposition, based on deposit architecture of 1998 and 1994 Merapi flows. *J. of Volcanol. and Geotherm. Res.*, 139:117–134.
- Seyfried, R. and Hort, M. (1999). Continuous monitoring of volcanic eruption dynamics: A review of various techniques and new results from a frequency-modulated radar Doppler system. *Bull. of Volcanol.*, 60(8):627–639.
- Simkin, T. and Siebert, L., editors (1994). *Volcanoes of the World*. Geoscience Press Inc., Tuscon.
- Simkin, T. and Siebert, L. (2000). Earth’s volcanoes and eruptions: An overview. In Sigurdson, H., Houghton, B., McNutt, S., Rymer, H., and Stix, J., editors, *Encyclopedia of Volcanoes*, pages 249–261. Academic Press.
- Strauch, R. (1976). *Theory and Application of the FM-CW Doppler Radar*. PhD thesis, Faculty of the Graduate School, University of Colorado, Boulder, Colorado, USA.

- Tanguy, J., Ribière, C., Scarth, A., and Tjetjep, W. (1998). Victims from volcanic eruptions: a revised database. *Bulletin of Volcanol.*, 60:137–144.
- Ui, T. and Fujinawa, N. M. M. S. A. (1999). Generation of block and ash flows during the 1990-1995 eruption of Unzen volcano, Japan. *J. of Volcanol. and Geotherm. Res.*, 89:123–137.
- Voege, M. and Hort, M. (2006). Automatic classification of Doppler radar events at Merapi volcano, Indonesia: Part I. Submitted to *Geophysical Journal International*.
- Voege, M. and Hort, M. (2007). Installation of a Doppler radar monitoring system at Merapi volcano, Indonesia. Submitted to *IEEE Transactions on Geoscience and Remote Sensing*.
- Voege, M., Hort, M., and Seyfried, R. (2005). Monitoring volcano eruptions and lava domes with Doppler radar. *EOS, Transactions of the American Geophysical Union*, 86(51):537–548.
- Voege, M., Hort, M., Seyfried, R., and Ratdomopurbo, A. (2006). Automatic classification of Doppler radar events at Merapi volcano, Indonesia: Part II. Submitted to *Geophysical Journal International*.
- Voight, B., Constantine, E., Siswamidjyo, S., and Torley, R. (2000). Historical eruptions of Merapi volcano, central Java, Indonesia, 1768-1998. *J. of Volcanol. and Geotherm. Res.*, 100:69–138.
- Voight, B. and Davis, M. (2000). Emplacement temperatures of the november 22, 1994 nuée ardente deposits, Merapi volcano, Java. *J. of Volcanol. and Geotherm. Res.*, 100:371–377.
- Wadge, G., Macfarlane, D., Robertson, D., Hale, A., Pinkerton, H., Burrell, R., G.E.Norton, and James, M. (2005). Avtis: A novel millimeter-wave ground based instrument for volcanic remote sensing. *J. of Volcanol. and Geotherm. Res.*, 146:307–318.
- Wassermann, W. and Ohrnberger, M. (2001). Automatic hypocenter determination of volcano induced seismic transients based on wavefield coherence - an application to the 1998 eruption of mt. Merapi, Indonesia. *J. of Volcanol. and Geotherm. Res.*, 110:57–77.
- Wilson, L. (1976). Explosive volcanic eruptions - iii. plinian eruption columns. *Geophys. J. R. Astron. Soc.*, 45:543–556.
- Yamasato, H., Kitagawa, S., and Komiya, M. (1998). Effect of rainfall on dacite lava dome collapse at Unzen volcano, Japan. *Paper in Meteorology and Geophysics*, 48(3):73–78.

- Zimmer, M. and Erzinger, J. (2003). Continuous H₂O, CO₂, ²²²Rn and temperature measurements on Merapi Volcano, Indonesia. *J. of Volcanol. and Geotherm. Res.*, 125:25–38.
- Zimmer, M., Erzinger, J., and Sulistiyo, Y. (2000). Continuous chromatographic gas measurements on Merapi volcano, Indonesia. *DGG Mitteilungen*, Sonderband IV:87–92.
- Zlotnicki, J., Bof, M., Perdereau, L., Yvetot, P., Tjetjep, W., Sukhyar, R., Purbawinata, M., and Suharno (2000). Magnetic monitoring at Merapi volcano, Indonesia. *J. of Volcanol. and Geotherm. Res.*, 100:321–336.

Chapter A

Software Development

There are three kinds of information that have to be handled by the monitoring system: a) Doppler spectra, b) video images and c) status information. Doppler spectra have the highest priority in the system. They have to be stored to disk and they are sent via radio modem to the MVO, so that the MVO staff can analyze them in real-time. Video images also have to be stored to disk. Because sending a video image via radio takes much longer than sending a Doppler spectrum, they are sent only upon MVO request. Aside from this the system has to provide several services. During the measurements the system time has to be synchronized to GPS time and status information has to be sent via SMS. During maintenance and reconfiguration of the system the electromechanical mounting has to be controlled, and live video images as well as live data from the radar have to be displayed. The radar needs initialization after start-up so that important measurement parameters are set to the correct values.

Many of these tasks have to run simultaneously, requiring a multi-tasking operating system. We chose Microsoft Windows 2000[®], because a) it supports all hardware components used in the system, b) it has an "easy-to-use" user interface and c) our Indonesian colleagues are most familiar with this type of system. All software applications necessary for the measurements are installed as system processes, i.e. they are automatically started during system startup. This is especially important when the system comes back to live after a power failure.

To keep the complexity of the software development to a minimum, the tasks mentioned above have been divided into several modules/applications. Figure A.1 shows all modules involved in the measurements. Some modules interact and exchange information. For the communication between modules a special inter-pro-

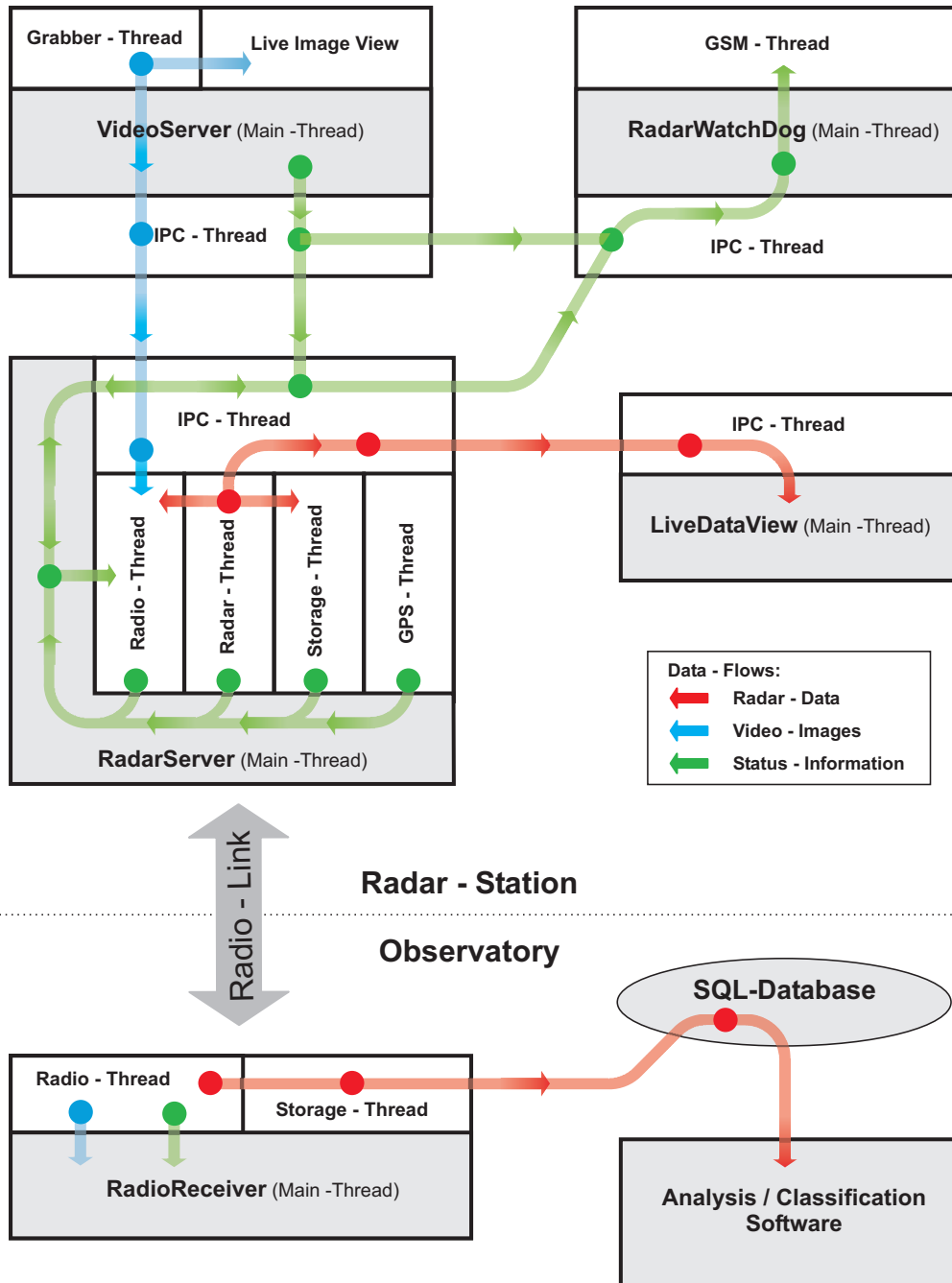


Figure A.1: Software - Tasks/Threads and their data flows.

cess-communication (IPC) has been developed.

In the following we will first describe those modules, which control the logging unit and all its peripherals during the measurements, i.e. *RadarServer*, *VideoServer*, *RadarWatchDog* and *RadarLiveView*. Then, we will describe the modules at the observatory unit, i.e. *TNCReceiver* and *RadarDbView*, which receive the data, store them into the database and provide user-interfaces to the radar data, video images and status information.

RadarServer: This module is responsible for most of the tasks during measurements: a) configure the radar device and receive radar data, b) write measured data to disk, c) synchronize the system to GPS time, and d) send data to the MVO via radio. These tasks have to run simultaneously, therefore each is organized as an independent thread as shown in Figure A.1. The main thread of the Radarserver is only responsible for starting and observing all other threads of this module. It gathers status information from all threads and compiles it to a status message. This status message is sent to the observatory by the radio-thread and is passed via IPC to the RadarWatchDog (see below).

Videoserver: The Videoserver mainly controls the framegrabber and retrieves images from the CCD camera. Executed as system process, the Videoserver is running throughout the measurements and images can be stored to disk at set intervals to observe visual changes at the dome. For radar beam alignment the Videoserver provides a live-image view. To document the radar beam orientation, images can be stored to disk manually from the live view. Via IPC, the Videoserver provides status information, i.e. the number of stored images, to the Radarserver and the RadarWatchDog (see below).

RadarWatchDog: The RadarWatchDog is responsible for keeping all processes running that are important for the measurements. It analyzes the status information received via IPC from the Radarserver and Videoserver and restarts them if necessary. The status information of both processes is compiled to a compact status message that can be sent by SMS via the GSM-modem. A SMS is sent out automatically once a week addressed to an email server, which forwards the message to email-accounts of the people, who are in charge of the system. In addition the RadarWatchDog is able to receive simple commands via SMS, i.e. to restart the whole system or to instantly send a status message.

RadarLiveView: All Doppler spectra are sent from the RadarServer to the RadarLiveView via IPC. The RadarLiveView displays the current Doppler spectrum and shows the echo power for the previous hour. In case the system is not measuring, i.e. the RadarServer has been stopped, the RadarLiveView can be used to change the radar's configuration and to get Doppler spectra directly from the radar and

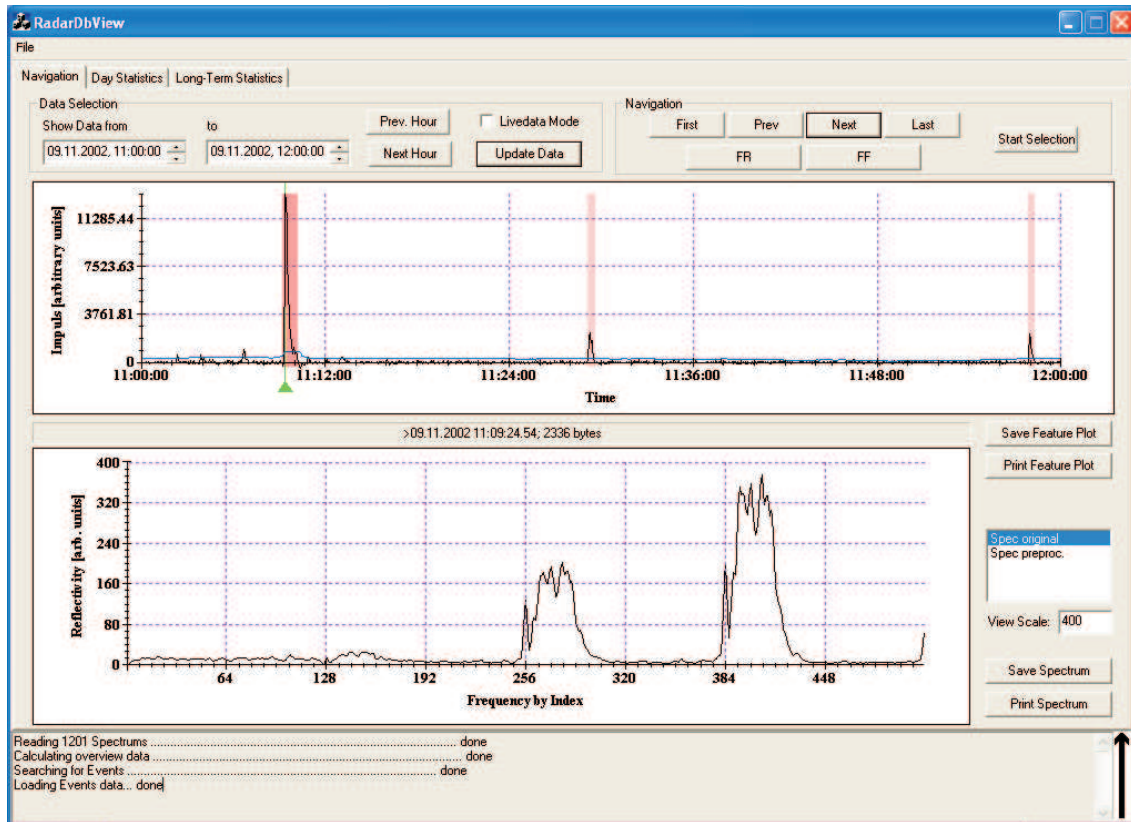


Figure A.2: Screenshot of the processing and analysis software *RadarDbView*. Here the navigation screen is shown, with Doppler spectrum features for one hour of data (black: the total reflected radar energy; blue: its long-term-average). You can see three radar events marked in red, all caused by dome instabilities. Below you see a complete Doppler spectrum of the first event, which is selected by the green marker in the feature plot.

display them in real-time.

TNCReceiver: The system process TNCReceiver receives the radar data, video images and status information at the observatory unit from both stations. The data streams of the different radar stations are sent via two logical channels of the same modem. The modem is able to receive data simultaneously for up to 10 channels. For each channel the received data is stored in an input buffer. To prevent an input buffer overflow, the TNCReceiver repeatedly reads the data from all input buffers at set intervals. When a complete dataset has been received an acknowledgment is sent back to the station via the same channel. In addition, the TNCReceiver is able to send commands to the station, i.e. to restart the system, to request status information, or to send a video image. Status information is also automatically sent by the radar stations every 5 minutes and displayed in a status view window.

Because of their size, video images are only sent once a day automatically. When requested by command they are displayed on screen immediately.

RadarDbView: The *RadarDbView* application is the most important tool to analyze the radar data. It consists of three processing screens: a) navigation screen, b) day statistics screen, and c) long-term statistics screen. The navigation screen allows the user to browse through the radar data. A time interval (up to one day) can be chosen for which the radar data is retrieved from the SQL-database. For each spectrum some key values, e.g. the total echo power of the whole Doppler spectrum, are calculated and displayed (see Fig. A.2). This feature (upper) plot gives the user an overview of the events that occurred during the chosen time interval. An event detection and classification algorithm marks events of different types by different colors. The feature plot can be used to browse the Doppler spectra. The Doppler spectrum marked by the user in the feature plot is displayed in the lower plot. The Doppler spectra can be displayed using different preprocessing procedures. The day statistics screen is used to automatically detect and classify all events that occurred during a selected day (see Voegelé and Hort, 2006). The resulting statistics shows the number of events of each type for each hour of the day. The long-term statistics screen does the same for several consecutive days. Here, the statistics shows the number of events for each event class for each day. Because the database is connected via TCP/IP, the RadarDbView is not bound to be executed on the observatory unit and can be used on every computer inside the MVO's intranet. Thus, multiple users have access to the radar data and especially during time consuming analyzes of large amounts of radar data the observatory unit is not blocked for other users.

Chapter B

Radar Beam Calibration

In order to align the CCD-camera with the radar beam we use rotating corner reflectors. The corner reflectors are attached to the ends of a 20cm long bar, which is rotating around a vertical axis at a constant rate (see Fig. B.1b). The rotation of the corner reflectors results in a well defined peak in the Doppler spectra. The corner reflector is setup at a position several hundred meters from the radar system. To make sure the measurements are not influenced by vegetation, it is mounted on top of a high mast.

In order to aim the radar beam exactly at the corner reflectors, we change the orientation of the radar, until we find the orientation with the strongest echo. Knowing the exact position the beam is pointing at, we can align the CCD-camera attached to the side of the radar mirror. During this alignment it is important to take into account that the camera is mounted approx. 80cm from the center of the mirror. To achieve an exactly parallel alignment of radar beam and camera, the camera has to aim at a position near the reflectors that corresponds to the camera's position in respect to the beam center.

Once beam and camera are aligned we can determine the intensity distribution of the beam. In order to do so, we do consecutive measurements on an equally spaced 2-dimensional grid (see Fig. B.1a), which gives a 2-dimensional contour plot in angle coordinates. Figure B.2 shows such a plot from a calibration measurement made in 2004 at station Babadan.

The calibration of radar and camera has to be done on a regular basis, e.g. every 6 month, to make sure that external influences like heavy weather and temperature changes have not changed the orientation of camera or radar beam. The calibration

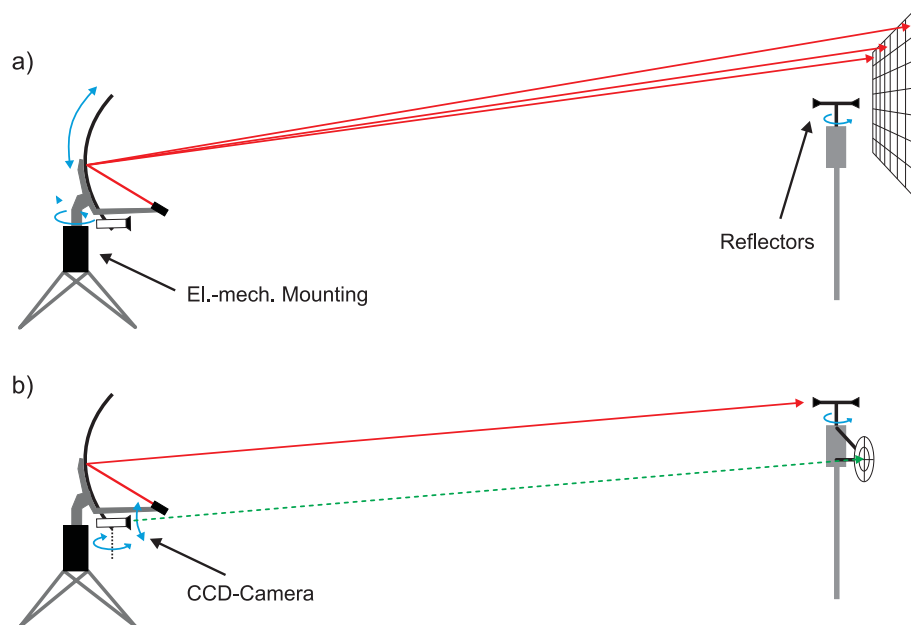


Figure B.1: Calibration of the radar beam: a) Aiming the radar beam at the target by searching for the maximum of the radar echo of the corner reflectors in the Doppler spectra. b) Aligning the camera parallel to the radar beam. To be parallel, the camera has to be aimed at point beside the target, which corresponds to the camera's position relative to the beam center.

can also be lost due to interference by animals or humans. Since finding the center of the radar beam and especially the grid measurements can be very time consuming, these tasks have been automated. Once the opening angle of the camera is known, the beam intensity distribution can be overlain onto the camera image. Now, while aiming the radar beam at the dome, one can clearly see which part of the dome is illuminated with which radar beam intensity (Fig. B.2).

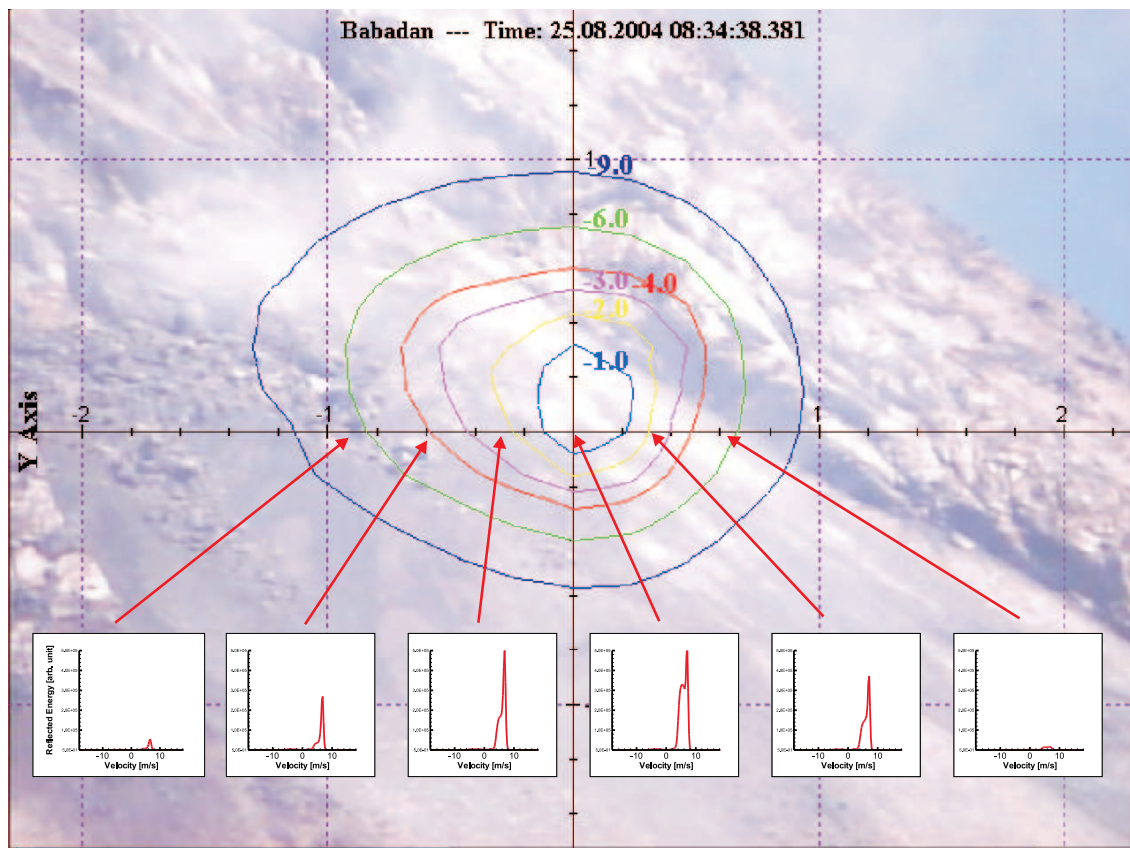


Figure B.2: Intensity distribution plot of the beam intensity obtained by a calibration measurement in 2004 in Babadan. Contour lines represent the attenuation in dB. The plots in the lower part show the Doppler spectra that have been used to calculate the intensity of the radar beam at the corresponding grid points. The image underlying the intensity distribution plot shows the area at the dome the radar beam has been aligned to after the calibration.

Acknowledgments

An dieser Stelle möchte ich mich bei allen bedanken, die mir bei der Erstellung dieser Doktorarbeit geholfen haben.

In allererster Linie gehört mein Dank Herrn Prof. Matthias Hort für seine hervorragende Betreuung und Unterstützung. Erst durch ihn bin ich in die Geophysik gelangt, und mit seinem fördernden Interesse und wertvollen Anregungen hat er im wesentlichen zum Gelingen dieser Arbeit beigetragen.

Ebenfalls danke ich Joachim Wassermann, dass er sich als Zweitgutachter zur Verfügung gestellt hat. Außerdem möchte ich ihm für die Unterstützung bei der Arbeit in Indonesien danken, bei der ich von viele Ratschlägen und Tipps seinerseits profitieren konnte.

Für die Hilfe bei der Arbeit in Indonesien möchte ich ebenfalls Antonious Ratdompurbo (Leiter des Merapi Volcano Observatory) danken, der uns immer nach Kräften bei unserer Arbeit unterstützt hat. Genauso möchte ich den Mitarbeiter des MVO danken, die uns immer sehr zuvorkommend begegnet sind. Ganz besonder gilt mein Dank an dieser Stelle Agus Sampurno, der uns mit Leib und Seele zur Seite stand. Ebenfalls danke ich Alexander Gerst, Malin Klawonn und Lea Scharff, die wesentlich zum erfolgreichen Aufbau der Radarstationen beigetragen haben.

Beim gesamten Institut für Geophysik bedanke ich mich für eine gute und entspannte Arbeitsatmosphäre. Besonders die Diskussionen in der Mittagspause mit Gesa, Daniela, Herrn Dümong und Frau Meier haben immer wieder auch die nötige Ablenkung gebracht. Ein ganz besonderer Dank geht an Christel Mynarik, der Guten Seele des Instituts, die mir bei so manchem Problem eine große Hilfe war. Hierbei sei besonders der zuweilen beschwerliche Fax-Verkehr mit Indonesien erwähnt.

Meinen Eltern und meiner Schwester, danke ich für ihre ausdauernde Unterstützung, die mich schon durch mein Studium gebracht hat.

Mein ganz besonderer Dank gilt meiner lieben Tina, die es nicht immer leicht mit mir hatte, aber trotzdem immer sehr viel Geduld mit mir bewiesen hat.

Das Merapi-Radar Projekt wurden von der Deutschen Forschungsgemeinschaft unter HO 1411 13-1, 14-1,2 und 15-1 gefördert.

Schließen möchte ich an dieser Stelle mit den Worten meines geschätzten Freundes Agus Sampurno: **Peaceful to be more, Danke!**